Selective and Dynamic Control of Thermal Conduction in Graphene Heterostructures

A Dissertation Presented for the

Doctor of Philosophy

Degree

The University of Tennessee, Knoxville

Ali Yousefzadi Nobakht

December 2018

© by Ali Yousefzadi Nobakht, 2018
All Rights Reserved.

This dissertation is dedicated to my loving wife, Fatemeh

Abstract

Thermal transport is critical in engineering system design, as it directly affects the stability, durability, and efficiency of systems. To overcome new challenges in engineering design for high-power, flexible, and miniaturized devices, more effective, delicate, and specific control of thermal transport is required. As two-dimensional (2D) materials have attracted attentions due to their promises for innovative devices, demands for advanced control of their thermal transport have also arisen. Among 2D materials, graphene has been intensively studied for various applications due to its exceptional properties, and especially, its high thermal conductivity allows for effective investigation of various control effects. Therefore, graphene is selected for this study on thermal transport control. Selective and dynamic control of in-plane and cross-plane thermal transport are investigated for graphene and graphene heterostructures with Si and SiO_2. For enhanced understanding of various control mechanisms, atomic vibrations and their fundamental properties are examined via molecular dynamics simulations.

Structural design (substrate, defect, doping, etc.) and system conditions (temperature and pressure), which can affect scattering kinetics and interfacial transmission, are examined to achieve selective and dynamic thermal transport control. This study suggests the following findings: 1) Adding a substrate to freestanding graphene significantly reduces thermal conductivity by suppressing out-of-plane phonons, while the effect of another substrate is minimal. 2) Applying a mechanical pressure is very effective for anisotropic control, showing that change of cross-plane thermal transport is more than ten times larger than in-plane transport. 3) Reduction of nanosize structural defects (holes) on graphene is two-orders-of-magnitude larger than macroscale porous structure with the same porosity. Moreover, the hole arrangement in nanoscale systems can change the transport reduction and induce

asymmetric thermal transport. 4) Si doping is another promising method of controlling in-plane conductivity by increased phonon scatterings, induced by both mass and interaction mismatch. 5) Both structural and point defects, created by holes and doping, enhance interfacial thermal transport due to the increase of cross-plane atomic interaction by in-plane structure weakening. Enhanced controllability of thermal transport from this research will allow for the development of innovative thermal engineering systems and improvement to energy conversion, storage, and heating/cooling systems.

Table of Contents

1 Significance of Advanced Thermal Transport Control **1**

1.1 Introduction 2

1.2 Materials and Methodology 3

1.3 Research Overview: Control Approaches 5

2 Anisotropic Control of Thermal Transport in Graphene/Si Heterostructures **8**

2.1 Abstract 9

2.2 Introduction 10

2.3 Methodology 11

2.4 Results and Discussions 15

2.5 Conclusions 26

3 Heat Flow Diversion in Supported Graphene Nanomesh **27**

3.1 Abstract 28

3.2 Introduction 29

3.3 Simulation Methods 30

3.4 Results and Discussion 35

3.4.1 Suspended GNM 35

3.4.2 Supported GNM 39

3.5 Conclusions 44

4 Thermal Rectification via Asymmetric Structural Defects in Graphene **45**

4.1 Abstract 46
4.2 Introduction 47
4.3 Material and Methods 48
4.4 Results and Discussion 52
4.5 Conclusions 58

5 Control of In-plane and Cross-plane Thermal Transport of Graphene by Silicon Doping 60

5.1 Abstract 61
5.2 Introduction 62
5.3 Materials and Methods 63
5.4 Results and Discussion 66
5.4.1 Suspended graphene 67
5.4.2 SiO_2 supported graphene 68
5.5 Conclusions 70

6 Conclusions 72

6.1 Summary and Contributions 73
6.2 Recommendation for Further Studies 76
6.3 Outlook 77
6.4 Publications 79
6.4.1 Journal publications 79
6.4.2 Conference presentations 80

Bibliography 81

Vita 104

List of Figures

2.1 Simulation models for the calculation of thermal transport properties. (a) Suspended graphene thermal conductivity. The hot and cold thermostats are placed to create temperature gradient (dT/dx) and heat flux ($\boldsymbol{q}$) along the sample for the in-plane thermal conductivity. (b) Supported graphene thermal conductivity. The hot and cold thermostats are placed on graphene and Si, separately. (c) Interfacial thermal resistance for supported graphene. The hot thermostat is placed on the graphene, and the temperature and energy evolution during thermal relaxation are recorded to calculate the interfacial thermal resistance. (d) Interfacial thermal resistance for sandwiched graphene. In addition to the thermal relaxation, the z-direction force is applied to the upper Si block for the pressure dependence of the thermal transport. 13

2.2 (a) Thermal conductivity of suspended graphene (k_{sus}) with respect to the distance between hot and cold reservoirs ($d_{H\text{-}C}$). The bulk conductivity of suspended graphene ($k_{0,\mathrm{sus}}$) and the ballistic conductance ($G_{B,\mathrm{sus}}$) are estimated from the length dependence. (b) In-plane thermal conductivities of the supported (k_{sup}) and sandwiched (k_{sw}) single-layer graphene with respect to $d_{H\text{-}C}$. (c) Relative thermal conductivities in supported and sandwiched graphene compared with suspended graphene ($k_{\mathrm{sup}}/k_{\mathrm{sus}}$ and $k_{\mathrm{sw}}/k_{\mathrm{sus}}$). Thermal conductivity is reduced by the interaction with Si, and the reduction increases with $d_{H\text{-}C}$. 17

2.3 (a) Comparison between the suspended and supported phonon density of states (DOS, D_p) for in-plane and out-of-plane phonon modes. Differing from in-plane phonons, D_p in out-of-plane phonon modes (ZA and ZO) is significantly changed. (b) Total phonon DOS of suspended, supported, and sandwiched graphene. D_p of bulk Si and Si near the interface with graphene are also added. The supported and sandwiched D_p's are slightly different, and the cross-plane interaction shifts D_p's in both cases to Si D_p. (c) Relative contributions of in-plane and out-of-plane phonons to the in-plane thermal conductivity. The out-of-plane phonon contribution reduces by the interaction with the substrate. (d) Phonon specific heat capacities (normalized by nk_B) calculated for the suspended and supported SLGs using D_p's in Figs. 3(a) and (b). 19

2.4 (a) Temperature evolution of SLG and Si during thermal relaxation. (b) The decays in temperature difference ($\triangle T_{\text{SLG- Si}}$) and the energy in graphene (E_{SLG}) (inset). The equilibrium temperature in the sandwiched structure is lower than the supported due to its doubled Si mass or doubled heat capacity, and the relaxation is also faster in the sandwiched structure due to the larger contact area. 21

2.5 Variations of (a) in-plane thermal conductivity of SLG (k_{sw}) and (b) cross-plane interfacial thermal resistance ($R_{\text{SLG/Si}}$) in the sandwiched structure (Si-SLG-Si) with respect to the applying pressure (p). $R_{\text{SLG/Si}}$ decreases as p increases while k_{sw} does not vary significantly. 22

2.6 (a) Atomic density distribution of Si with respect to the distance with C atoms. The increase in p decreases the average distance between C and Si, which induces the stronger interaction. (b) D_p's of phonon modes polarized in the in-plane directions (xy) in the sandwiched SLG and interfacial-region Si under two different p's (0 and 2.6 GPa). (c) Out-of-plane D_p's in the sandwiched SLG under the pressures of 0, 1.0 and 2.6 GPa. (d) D_p's of phonon mode polarized in the cross-plane direction (z) in the interfacial-region Si with respect to p (the out-of-plane D_p in the sandwiched SLG under the maximum pressure is added as a reference). While the in-plane phonons do not change with p, out-of-plane phonons in both interfacial Si and SLG have additional low-energy peaks in D_p, which increases with p. (e) D_p's of silicon at different distances from the interface (p=2.6 GPa). The peak near zero energy disappears after few layers of atoms far from the interface. . . 24

2.7 (a) Out-of-plane phonon D_p's in the sandwiched SLG using different interaction strength (ε). (b) In-plane thermal conductivity (k_{SLG}) and interfacial thermal resistance ($R_{\mathrm{SLG/Si}}$) in Si/graphene (SLG)/Si structure with respect to interaction strength. 25

3.1 Simulation models for the calculation of thermal transport properties. (a) Square hole arrangement and (b) zigzag hole arrangement of GNM. (c) GNM with Si substrate (side view). Separate hot and cold thermostats are placed on Si and GNM. 32

3.2 (a) Mesh structure for the local heat flux distribution in GNM. (b) The difference between calculated cell temperature and temperature of simulation sample ($T_{\mathrm{cell}} - T_{\mathrm{total}}$) with respect to number of meshes in each side of the dashed quare (n). 34

3.3 Size dependence of GNM thermal conductivity for three different sample length and two different porosity cases. 35

3.4 (a) Thermal conductivity of GNM with classical Eucken model, square (SA), and zigzag (ZA) hole arrangements with respect to porosity (ζ). (b) Relative GNM thermal conductivity of the zigzag hole arrangement as compared to that of the square hole arrangement ($k_{\mathrm{ZA}}/k_{\mathrm{SA}}$) with respect to porosity (ζ). Comparison of thermal conductivity in-plane (k_{xy}) and out-of-plane (k_z) phonon modes, and relative thermal conductivity of out-of-plane phonon modes (k_z/k_{GNM}) for (c) square hole arrangement (SA) and (d) zigzag hole arrangement (ZA). 37

3.5 Temperature dependency of GNM in-plane thermal conductivity with square (filled shapes) and zigzag (outlined shapes) hole arrangements at various porosities (dashed lines are linear fit in logarithmic scale, which is exponential fit in linear scale). (b) Exponent of exponential fit (slope of the linear fit in logarithmic scale) of thermal conductivity changes with temperature for different porosities. 38

3.6 In-plane local heat flux distribution. (a) Heat flux distribution in the square hole arrangement GNM with hole radius of 25 Å. (b) Magnitude/angle distribution of the in-plane heat flux vectors within the square hole arrangement. (c) Heat flux distribution in the zigzag arrangement GNM with hole radius of 25 Å. (d) Magnitude/angle distribution of the in-plane heat flux vectors within the zigzag hole arrangement. 40

3.7 (a) Relative thermal conductivities of supported SA and ZA GNM to the suspended GNM ($k_{\mathrm{sup}}/k_{\mathrm{sus}}$). (b) Relative thermal conductivity of GNM to non-porous graphene ($k_{\mathrm{GNM}}/k_{\mathrm{GNM,np}}$) in suspended and supported SA and ZA GNMs with respect to porosity (ζ). 41

3.8 (a) Temperature profiles for Si (dashed lines) and GNM (solid lines) during the temperature relaxation period. As porosity increases, the system reaches thermal equilibrium more quickly and at a lower equilibrium temperature. (b) Interfacial thermal resistance, R (outlined shapes and dashed line), and areal interfacial thermal resistance, $R''(\zeta) = A(\zeta)R(\zeta)$ (filled shapes and solid line). To evaluate the effect of decreasing A on decreasing R, $R''(\zeta) = A(\zeta)R(0)$ is also plotted (dashed dot line). (c) Upper panel: Alterations in potential energy (φ) and atomic force (F) of Si and C atoms, based on the used vdW LJ potential model, with respect to atom distance. Lower panel: Atomic density distribution of Si with respect to the distance of C atoms. Porosity increases lead to decreases in the average distance between Si and C, and potential energy and force increases. (d) Upper panel: D_p of Si near the interface with graphene (< 5 Å from the interface). Lower panel: D_p of supported GNM at various porosities. 42

3.9 Ratio of heat addition/subtraction to/from the thermostated regions (q_T) to the ensemble average of the heat flux x component ($q_{f,x}$) within supported GNM. 43

4.1 Schematics of simulation cells for (a) triangular hole arrangement (TRA), and (b) rectangular hole arrangement (REA). In both cases, the heat flow direction from low to high porosity region is defined as the forward direction, and the opposite direction is reverse direction. In this figure, the white circles represent the holes distributed in DEG. (c) The relation between the porosity (ζ) and the degree of asymmetry (α_A). Here, d_s=0 for the rectangular case. 50

4.2 Heat flux ratio of DEG with triangular hole arrangement to non-defect graphene with respect to porosity (ζ) and asymmetricity (α_A). (b) Thermal rectification of DEG with triangular hole arrangement with respect to porosity (ζ) and asymmetricity (α_A). 53

4.3 Local heat flux distribution in DEG with a triangular hole arrangement. For the forward direction of heat flow, (a) local heat flux contour, (b) local heat flux vectors, and (c) angular distributions of local heat flux vectors. For the reverse direction of heat flow, (d) local heat flux contour, (e) local heat flux vectors, and (f) angular distributions of local heat flux vectors. 53

4.4 (a) Phonon density of states (D_p) of TRA-DEG at Regions A and B in the forward and reverse heat flow directions. (b) Effect of porosity on D_p overlap factor (S) of TRA-DEG, for the forward and reverse heat flow directions. 55

4.5 Local heat flux distribution in DEG with a rectangular hole arrangement. For the forward direction of heat flow, (a) local heat flux contour, (b) local heat flux vectors, and (c) angular distributions of local heat flux vectors. For the reverse direction of heat flow, (d) local heat flux contour, (e) local heat flux vectors, and (f) angular distributions of local heat flux vectors. 56

4.6 Thermal rectification of REA-DEG (a) with respect to porosity with different non-defected areas (d_s = 0 and 5 nm). (b) With two different porosities, rectification variations with respect to non-defected area size (d_s). (c) Comparison of thermal rectifications for TRA and REA with two different non-defected area sizes 58

5.1 Schematics of simulation cells for (a) suspended Si-doped graphene (b) SiO_2 supported Si-doped graphene. 64

5.2 (a) Effect of mass, potential, and mass+potential on the in-plane thermal transport of suspended Si-doped graphene as a function of dopant concentration. (b) Relative contribution of mass and potential on thermal transport reduction. 67

5.3 (a) Effect of mass, potential, and mass+potential on the in-plane thermal transport of supported Si doped graphene as a function of dopant concentration. (b) Relative contribution of mass and potential on thermal transport reduction. 68

5.4 Cross-plane interfacial thermal resistance in the supported Si doped graphene with respect to dopant concentration. 69

5.5 (a)D_p's of pure graphene, as well as mass, potential, and mass+potential effect. (b) D_p's of phonon mode polarized in the cross-plane direction (z) for pure graphene, as well as mass, potential, and mass+potential effect. The near zero phonon peak appears for the doped graphene and similar to previous results, the potential has a larger effect in comparison with mass effect. 70

6.1 (a) Applying asymmetric doping to generate thermal rectification in graphene layer. (b) Asymmetric interfacial thermal transport induced by non-uniform pressure applied to the interface. (c) Assembling nano thermal rectifiers to create micro and macro thermal rectifiers. 78

Chapter 1

Significance of Advanced Thermal Transport Control

1.1 Introduction

Performance and stability of many engineering applications are affected by their thermal properties. Since high temperatures (i.e., large phonon population) lead to frequent electron scattering, hindering electron transport [1, 2] and deteriorating the performance of electronic devices (e.g., transistors) as well as photovoltaic cells or batteries, thermal transport is as critical as electrical transport in various applications (e.g., the power of a solar panel decreases by 0.485% per the temperature increase of 1°C from 25°C [3]). High thermal conductance/conductivity enhances heat dissipation and reduces temperature distribution with a given heat flow. On the other hand, low conductance/conductivity is required to preserve thermal energy and isolate thermal systems from external effects such as refrigerator or cooling/heating chamber. The desirable thermal transport behaviors are achieved by selecting proper materials and/or system design.

Above the enhancement of heat insulation or dissipation, more delicate, specific control of thermal transport, which includes i) anisotropic, ii) asymmetric, and iii) carrier property- and species- dependent controls, will contribute to the breakthrough of application performance and shed light on the development of thermal devices.

Depending on the application, a system needs both dissipating and insulating characteristics; in those applications, directional control or anisotropic thermal transport is desirable (i.e., thermal transport should be high in one direction but not in other direction). Examples include manufacturing process (maintaining a constant bed temperature with lateral-direction insulation) and electronic packaging (working as thermal cable transferring heat to heat sink) [4], in addition to energy storage systems [5] and space fission propulsion/power systems [6].

Thermal energy storage and building heating will be more efficient when packaging or wall layers allow for large heat transfer from heat source while limiting heat loss from the system to heat sink. For cooling devices or thermal management, however, the reverse directional dependency will be desirable. This asymmetric thermal transport along a specific axis which depends upon the sign of the temperature gradient or heat current is termed as rectification [7]. In addition to energy efficiency and thermal management, effective rectification will be

base of innovative thermal (phononic) devices (switch, diode, transistor, etc.) [8] as analogies of electronics.

Electron and lattice vibration (phonon when quantized) are main thermal energy carriers in solid systems. Selective transport control depending on these energy carrier species is important; for example, in well-known thermoelectric energy conversion, lowering thermal conductivity while maintaining electrical conductivity enhances thermoelectric efficiency [1]. In addition, more detailed modal and spectral control can be considered; since electron scattering in semiconductors is dominated by interaction with optical phonons [2], reducing the population of high-energy optical modes will be effective to enhance electron scattering; i.e., selective filtering of specific mode or frequency will improve performance of electronic devices in an innovative way.

In addition to the aforementioned selective controls, dynamic control of thermal transport via operational conditions, such as temperature and pressure, can further enhance thermal system design as it allows for real-time response to change of external conditions.

Considering those mentioned above, investigating new methods of controlling the rate and direction of the heat flow in solid systems is vital to improve our physical understanding of the thermal transport phenomenon and enhance the design of electronic, energy conversion, and phononic devices.

1.2 Materials and Methodology

To enhance and innovate the design and performance, future electronic devices are expected to be smaller, faster, and more flexible. Due to their distinctive electrical, thermal, mechanical, and chemical properties, 2D materials have been studied as a key to achieving high-performance flexible electronics [9, 10, 11, 12]. Not only for electronics, but 2D materials are also expected to improve the performance of energy conversion and storage systems such as solar photovoltaic cells, batteries, and thermoelectric systems [13, 14]. Among the 2D materials, graphene with hexagonally arranged carbon atoms, receiving the most attention today.

In graphene, the charge carriers can be described as massless Dirac fermions resulting in extremely large electrical mobility (up to $\sim$15000 cm^2/V-s at room temperature) [15, 16, 17]. Additionally, it possesses exceptional high thermal conductivity (range of 3080$-$5150 W/m-K and phonon mean free path of $\sim$775 nm near room temperature) [18, 19], high mechanical strength (Young's modulus of 1 TPa and intrinsic strength of 130 GPa [20, 21]), as well as optical transparency [22]. Most thermal properties of graphene are derived from the strong in-plane covalent sp^2 bonds between neighboring carbon atoms which, are among the strongest in nature (stronger than the sp^3 bonds in diamond), with bonding energy of approximately 5.9 eV [23]. The utilization of these superior properties can already be seen with the integration of graphene in solar photovoltaic cells, where a significant performance enhancement was reported [24, 25, 26]. However, depending on the application, graphene properties are not always desirable; the high thermal conductivity and low Seebeck coefficient of pristine graphene are not appropriate for thermoelectric systems, and graphene requires a nonzero band gap in order to be a charge collector in solar cells [27] or have high on/off switching ratios (approximately 100 [9]).

Wide range of graphene applications (e.g., field effect transistors [28], thermoelectric (TE) energy conversion [29, 30, 31, 32], gas detection [33], solar cells [34] etc.) and its unique properties made this material enough promising to be chosen as the goal material for this research. Above all, high thermal conductivity of graphene holds promise for manipulation of thermal transport characteristics, and its low phonon-phonon (p-p) scattering rate allows for geometric confinement or defects to have a significant influence on thermal transport control [35, 36], exotic physics of two-dimensional (2D) phonon transport [37] which makes it very promising to be used in different engineering designs. Since graphene is a 2D material, it is used mostly in supported or sandwiched form in engineering applications. In this research Si and SiO_2 (most used semiconductor and insulator materials in the electronics industry) as the supporting materials. Moreover, in the 2D materials, all of the atoms are affected by the substrate effect and study of the graphene in supported and sandwiched mode provides more insights to the ongoing physics of the thermal transport.

Atomic vibrations (or phonons when quantized in the lattice) are the main energy carriers for thermal transport in graphene, semiconductors, and insulators, and we can

neglect electron transport for heat transfer calculations in these materials. Considering computational cost and feasibility to simulate larger systems, thermal transport physics can be predicted with an acceptable accuracy using molecular dynamics (MD) simulations. Thus, MD simulation is selected as the main tool in this study, which can provide enough information to understand the heat conduction in graphene systems while giving us the ability to simulate large enough systems with affordable simulation cost.

1.3 Research Overview: Control Approaches

This research will investigate the effective control of thermal transport properties in two-dimensional (2D) materials system using atomistic computer simulations. We seek for selective control of transport, which includes transport control of selective energy carrier and anisotropic transport control. The former can enhance the performance of thermoelectric conversion [1], for which thermal transport should be reduced while maintaining electrical conductivity, and the latter, can improve the design of thermal management system in electronic devices [38] and energy storage systems [39].

Despite versatility and effectiveness, controlling thermal transport is challenging because main thermal carriers, i.e., phonons, are governed by only diffusion (high to low phonon population or temperature) differing from charged particles driven by the electric potential in addition to diffusion [1]. Intensive efforts to control thermal transport [40, 41, 42, 43] have been made to overcome this challenge; however, the effectiveness of various transport control approaches needs to be quantified for an enhanced design of transport control system, and understanding of the control mechanisms should be improved. For quantification of control effectiveness, computational simulations will be effective tools because various structural and operating conditions can be systematically controlled. In particular, atomistic simulations allow for not only calculation of thermal transport properties for effectiveness evaluation, but also direct analysis of carrier properties, which facilitates to the identification of fundamental control mechanisms and dominant controlling factors.

According to kinetic transport theory [44], thermal conductivity of 2D materials can be defined as $k = (1/2)C\nu\Lambda$, where C is the specific heat, ν is phonon group velocity,

and Λ is phonon mean free path (MFP) [45]. By exposing graphene to a substrate, creating geometrical or structural defects, and point defects (i.e., doping), we can alter and control the Λ and in-plane thermal transport kinetics as the result. The cross-plane thermal transport can be controlled by manipulating and designing the system in a way to affect the interfacial phonon transmissivity τ_r value. The interfacial transmission can be controlled by interfacial interactions and phonon status. Applying mechanical force to interface can reduce the average inter-plane distance and increase the interaction rate, or geometrical defects can weaken the structure of graphene and make it more easily influenced by interactions with the substrate. Therefore, by applying mechanical forces, geometrical defects, asymmetric defects arrangements, and Si doping, we can achieve selective and dynamic control of the in-plane and cross-plane thermal transport in graphene heterostructures.

Chapter 2 will discuss the effect of applying mechanical forces, as a dynamic and selective method of manipulating thermal direction and magnitude, to the graphene/silicon interface on the in-plane thermal conductivity of the graphene, as well as interfacial thermal transport. Also, the effect of substrate on the in-plane thermal conductivity of graphene, as heterostructure effect is investigated. The results of this chapter have been published in the *Journal of Applied Physics* [46].

Chapter 3 will demonstrate the results of our study on the effect of structural defects on the in-plane and cross-plane thermal transport in graphene/Si heterostructures. Here, the effects of the size and arrangement of defects on controlling the direction and magnitude of thermal transport have been investigated. The results of this chapter have been published in the *Carbon* journal [47].

In chapter 4, the effect of asymmetrically arranged defects on the in-plane thermal conductivity of graphene will be discussed, demonstrating asymmetrically arranged defect can create directional dependance thermal conductivity will be investigated. We will see that asymmetric geometry can result in different thermal conductivity in the different direction, which is called thermal rectification. The results of this chapter have been published in the *Carbon* journal [48].

Chapter 5 will discuss impurity (i.e., doping) effect on the in-plane thermal conductivity of single-layer graphene. Doping graphene with heavier atoms like Si can reduce the thermal

conductivity of graphene and can be an effective method of selective controlling thermal transport in graphene. The results of this study are under review in the *Computational Materials Science* Journal.

Chapter 2

Anisotropic Control of Thermal Transport in Graphene/Si Heterostructures

A version of this chapter was originally published by Ali Yousefzadi Nobakht and Seungha Shin:

Yousefzadi Nobakht, Ali, and Seungha Shin. "Anisotropic control of thermal transport in graphene/Si heterostructures." *Journal of Applied Physics* 120.22 (2016): 225111.

2.1 Abstract

The cross-plane interaction across interface changes phonon kinetics and spectrum near the interface, and the interaction effects on both in-plane and cross-plane thermal transport are investigated in graphene/Si heterostructure. The interaction with substrates dramatically reduces the in-plane thermal conductivity of graphene by changing the behaviors of the out-of-plane phonons as well as adding phonon-substrate scatterings. Applying pressure up to 2.6 GPa to the sandwiched graphene reduces the cross-plane interfacial thermal resistance by 50% without altering the in-plane thermal conductivity in a significant way. The pressure increases the inter-layer coupling and creates a low-energy phonon transport channel between graphene and Si with minor effects on phonons propagating along the graphene. This study suggests anisotropic control of thermal transport, and the physics and calculation results can be used to improve the thermal design and analysis in two-dimensional nano-electronic devices.

2.2 Introduction

As the electronic industry miniaturizes devices and electronic parts shrink to nanometers, the thermal management of these devices are becoming a challenge [49]; effective heat dissipation is required for the device performance and stability [50]. The reported high electrical [51] and thermal conductivities [18, 19, 52] of single-layer graphene (SLG) have made this material a very promising candidate for electronic applications such as field effect transistors [28]. However, when graphene is supported by a substrate, the superior thermal conductivity is dramatically reduced due to the influence of contacting materials [32]. Since graphene in micro- and nano-electronics is mostly supported or sandwiched rather than suspended [53, 54], both in-plane and cross-plane thermal transports, which are characterized by in-plane conductivity and interfacial conductance (inverse of resistance), should be studied with the consideration of the cross-plane interactions of contacting materials for the thermal design of graphene applications [55, 56, 57, 58, 59, 32]. In particular, the interfacial thermal transport between graphene and substrates plays a critical role in the saturation of graphene electronic devices [60, 61, 62]. There are many recent studies on different methods of controlling interfacial thermal transport [63, 57, 64]; however, for further enhancement of electronic device design and heat dissipation, we still need to find an effective, cheap and feasible way of controlling directional thermal transport, and improve physical understanding on interfacial interactions.

In this research, we study the thermal transport in various configurations and conditions of graphene heterostructures for understanding the cross-plane interaction physics, finding methods to control thermal transport, and enhancing the thermal design and analysis. Since quantized atomic vibrations, i.e., phonons, are main thermal energy carriers in the graphene systems [53, 54], we focus on thermal transport by phonons. Molecular dynamics (MD) is employed to study the phonon transport including the in-plane conductivity of SLG as well as cross-plane interfacial conductance between SLG and substrate. Si is selected as substrate because it is a representative of semiconductors and the most common material used in the electronic devices.

To identify the influence of cross-plane interaction on phonon behavior, which is expected to cause the change in thermal transport properties, we calculate the phonon density of state (DOS) of SLG under different conditions. Supported and embedded (sandwiched) forms of SLG are investigated, and the phonon transport properties and spectra in the heterostructures are compared with the suspended (free-standing) SLG. In the sandwiched SLG, we apply the compressing pressure, as a potential tool to control the strength of the interactions between SLG and Si substrates, and study the effects on the interfacial thermal resistance as well as in-plane thermal conductivity.

2.3 Methodology

Periodic boundary conditions are applied in x and y directions while a free boundary condition is used in z direction to avoid interactions between periodic cells. Here, x is the in-plane heat flow direction and z is the flow direction for interfacial thermal transport [Figs. 2.1(a)-(d)]. Our simulations showed that the width dependency of thermal conductivity is negligible for sample wider than 11 nm, so we choose 11.6 nm for the simulation sample width (w in y direction) to reduce the computational cost and minimize lattice mismatch in Si/SLG heterostructures. Various lengths (l) are simulated for the length dependence of thermal conductivity (k) and the calculation of bulk thermal conductivity (k_0). l ranges from 40 to 2400 nm in simulations for the suspended SLG, however l's in the supported and sandwiched SLG structures are less than 300 nm due to the computational cost. For the cross-plane transport, a fixed, mid-size sample length ($\sim$ 200 nm) is selected. The width and length of the Si block are the same as the graphene, and the size of Si in z direction is 3.8 nm. Based on our simulations on different Si block sizes, this thickness of Si block is large enough to avoid size dependence of simulation results. All the simulations were performed in Large-scale Atomic/Molecular Massively Parallel Simulator (LAMMPS) [65], all results in this work are average of five independent simulations, and the time step for all our simulations is chosen to be 0.5 fs. Adaptive intermolecular reactive empirical bond order (AIREBO) [66] is used to model C-C bonded interactions, and three-body Stillinger-Weber [67] potentials for Si-Si interactions. Primarily short-range, van der Waals (vdW)

interaction [68, 69] between C and Si atoms is modeled by the 12−6 Lennard-Jones (LJ) potential, $\varphi_{LJ} = 4\varepsilon[(\frac{\sigma}{r})^{12} - (\frac{\sigma}{r})^{6}]$, where ε is the energy at equilibrium position, σ is the distance at which the intermolecular potential between the two particles is zero, and r is the distance of separation between particles. The potential parameters used in our simulations are based on the vdW interactions in the universal force field (UFF) model by Rappe, et al. [70].

Thermal conductivity is calculated by using non-equilibrium molecular dynamics (NEMD) [71, 72, 73, 74, 75, 76, 77]. After the equilibration in NVT ensemble (constant number of particles, volume, and temperature) at a measured T for 0.5 ns employing velocity rescaling, the hot and cold Langevin thermostats are added at $x = l/4$ and $3l/4$ with a width of $l/20$ (i.e., distance between two thermostats, $d_{H\text{-}C} = l/2$) [Fig. 2.1(a)] [72, 73, 76]. Temperature is averaged for long enough period of time (1 ns) to minimize the noises in temperature distribution. Thermal conductivity k (W/m-K) is calculated by using Fourier's law, $\boldsymbol{q} = -k\nabla T$ with a heat flux from the hot to the cold region, $\boldsymbol{q}$ (W/m^2) and a temperature gradient, $\nabla T (= dT/dx$ in 1D transport). $\boldsymbol{q}$ is the average heat addition and removal over 2 ns on thermostats per unit cross-sectional area. The interlayer spacing of graphite, (0.335 nm [78]), is selected as the thickness of a single-layer graphene for the cross-sectional area. For ∇T, T-distribution is calculated from the local kinetic energy average, and to avoid the thermostat effects and T-dependence, the linear part of T-profile near a measured T is used. In order to calculate the thermal conductivity of graphene with a Si substrate, hot and cold thermostats are placed in graphene and Si for direct calculation of graphene heat flux as in Fig. 2.1(b) separately. The hot and cold thermostats in graphene and Si are set as the same temperatures, and after equilibration of MD simulations, Si and graphene temperature distributions are parallel and almost identical; thus, heat leakage to or addition from Si substrate is negligible. In addition to heat flux at thermostats ($l/4$ and $3l/4$) calculated using thermostat heat addition and removal, x component of local heat flux (q_x) is measured at three different locations ($3l/8$, $l/2$, and $5l/8$) as given by[79]

$$q_x = \frac{1}{V}[\sum_i \frac{1}{2} m_i(\boldsymbol{u}_i \cdot \boldsymbol{u}_i)u_{i,x} + \sum_i \varphi_i u_{i,x} + \frac{1}{2}\sum_i \sum_j x_{i,j}(\boldsymbol{u}_i \cdot \boldsymbol{F}_{ij})], \tag{2.1}$$

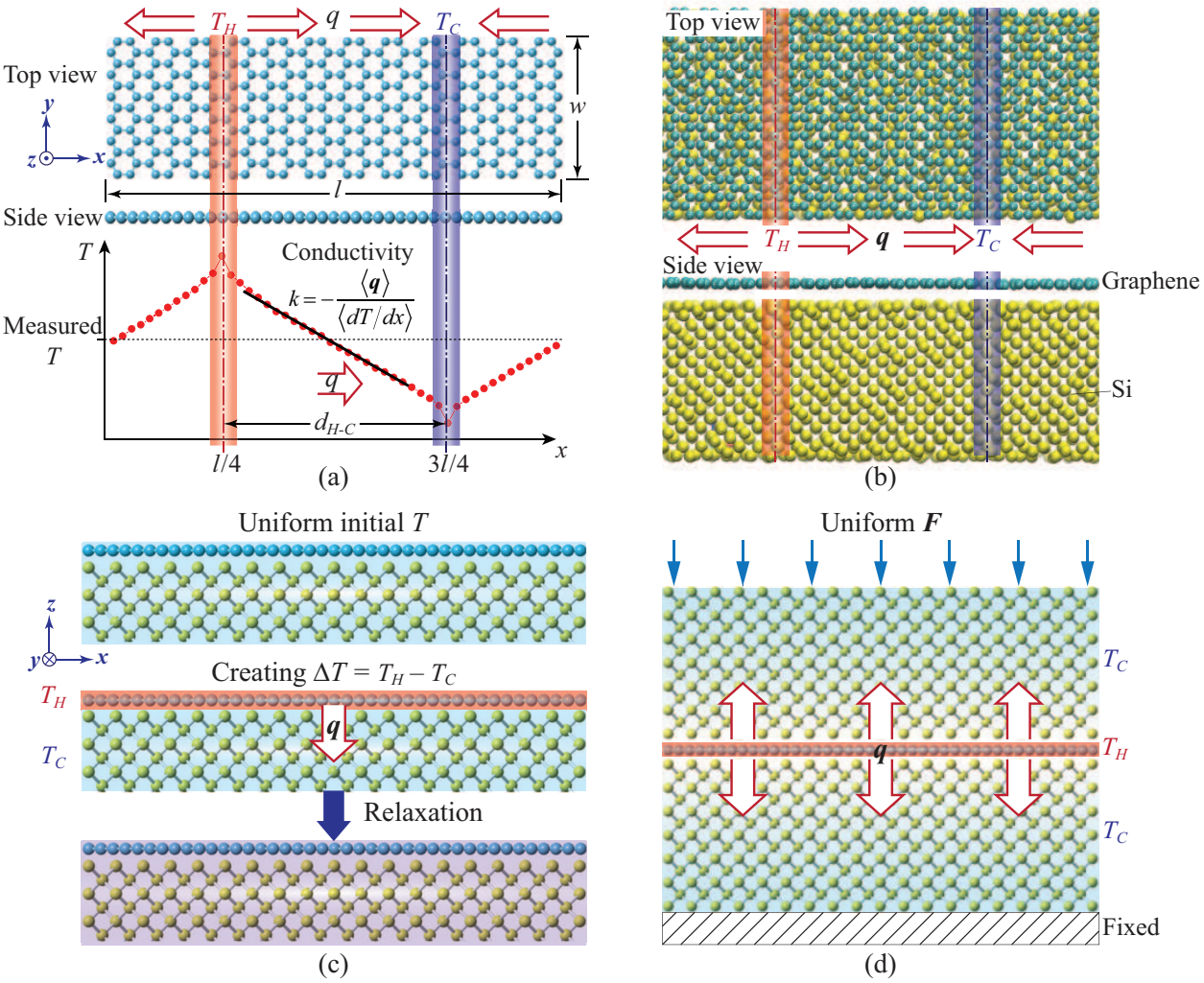


Figure 2.1: Simulation models for the calculation of thermal transport properties. (a) Suspended graphene thermal conductivity. The hot and cold thermostats are placed to create temperature gradient (dT/dx) and heat flux ($\boldsymbol{q}$) along the sample for the in-plane thermal conductivity. (b) Supported graphene thermal conductivity. The hot and cold thermostats are placed on graphene and Si, separately. (c) Interfacial thermal resistance for supported graphene. The hot thermostat is placed on the graphene, and the temperature and energy evolution during thermal relaxation are recorded to calculate the interfacial thermal resistance. (d) Interfacial thermal resistance for sandwiched graphene. In addition to the thermal relaxation, the z-direction force is applied to the upper Si block for the pressure dependence of the thermal transport.

where V is the volume, m_i is the mass of particle i, $\boldsymbol{u}_i$ is the velocity vector, $u_{i,x}$ is the x component of $\boldsymbol{u}_i$, φ_i is the potential energy, x_{ij} is the x component of the interatomic separation ($\boldsymbol{r}$), and $\boldsymbol{F}_{ij}$ is the interaction force between i and j particles. In all cases, heat fluxes calculated at thermostats agree well with local heat flux calculation and the local heat flux is almost constant ($< 5\%$ difference), which confirms negligible heat leakage i.e., 1D thermal transport under this thermostat setup. In this research, a local heat flux at the center ($l/2$) will be employed in conductivity calculation. To estimate contributions of out-of-plane and in-plane phonon modes to thermal transport separately, either z-direction polarization only or xy-direction polarization only is included in the heat flux calculation. For the sandwiched graphene simulation, the graphene layer is placed between two Si blocks [Fig. 2.1(d)] and the same methodology as in the supported case is employed for the calculation of q_x and k.

The interfacial thermal resistance is calculated by analyzing the temperature relaxation [80, 81]. The system is equilibrated first at 300 K, and then hot and cold thermostats are placed on graphene and Si, respectively. Once reaching a stable temperature on graphene and Si, the thermostats are removed to relax the system thermally. During the relaxation period, the temperatures and total energies of the graphene and Si are recorded and used for the calculation of (areal) interfacial thermal resistance, R ($\mathrm{m^2}$-K/W) given as [80, 82, 83, 84]

$$\frac{\partial E_t}{\partial t} = A\frac{T_{\mathrm{SLG}} - T_{\mathrm{Si}}}{R}, \tag{2.2}$$

where E_t is the total energy of the supported graphene, A is the thermal transport interface area, and T_{SLG} and T_{Si} are the graphene and Si temperatures. In our simulations and previous studies [64, 85, 83, 84], R is almost constant for the temperature range of simulation (200-500 K), so approximating R as constant, Eq. (2) is integrated as

$$E_t = E_0 + (\frac{R}{A})\int_0^t (T_{\mathrm{SLG}} - T_{\mathrm{Si}})dt, \tag{2.3}$$

where E_0 is the initial total energy of graphene. In the sandwiched graphene case, A is doubled since heat flows in both up- and downward direction.

The sandwiched structure is selected to investigate the effect of the pressure (p) on the interfacial thermal resistance and in-plane thermal conductivity. We apply a uniform force to the upper Si block in negative z direction while constraining the z direction movement of bottom-layer atoms of lower Si block to keep it in its place [Fig 2.1(d)]. Phonon density of states (D_p) is calculated through the Fourier transform of the velocity autocorrelation function [86]. For this calculation, we use velocities of sampled atoms exported every time step from NVE ensemble simulations.

2.4 Results and Discussions

Since the distance between hot and cold reservoirs ($d_{H\text{-}C}$) is comparable to or smaller than the SLG phonon mean free path (λ_p∼750 nm [19]), thermal conductivity (k) is dependent on $d_{H\text{-}C}$ due to the ballistic effect; i.e., shorter $d_{H\text{-}C}$, lower k in NEMD simulations [87] as in Fig. 2.2(a). If $d_{H\text{-}C} \ll \lambda_p$, transport between two reservoirs will be almost scattering-free, and k will be proportional to product of ballistic conductance (G_B) and sample length (i.e., $k = G_B d_{H\text{-}C}$). However, the size-dependence of k is negligible in diffusive regime ($d_{H\text{-}C} \gg \lambda_p$) and the diffusive k is approximated as $G_B \pi \lambda_p/2$ [88]. Combining both ballistic and diffusive behaviors, k for intermediate $d_{H\text{-}C}(\sim \lambda_p)$ is suggested as follows in the previous studies [88, 54]

$$k \sim G_B \left(\frac{1}{d_{H\text{-}C}} + \frac{2}{\pi \lambda_p}\right)^{-1}. \tag{2.4}$$

However, k's from the NEMD simulations is not fitted well to Eq. (4), and especially a larger deviation from the fitting equation is observed with a longer length ($d_{H\text{-}C}$) than λ_p. This anomalistic length-dependence of k has been studied, and is attributed to the additional participation of low-frequency, long-wavelength phonons in transport, which is restricted by the system size [89, 90]. In Fig. 2.2(a), we used three aforementioned equations (for three length ranges) to fit the thermal conductivity results from our simulations. The first region (red, dashed-dot line) is for the ballistic thermal transport regime and the linear relation between k and G_B, the second region (purple, dot line) represents the range of intermediate

sample length, and the third region (black, long-dashed line) is for a long sample length, which incorporates more long-wavelength phonon contributions.

Using the fitting method [76], $G_{B,\mathrm{sus}}$, bulk conductivity ($k_{0,\mathrm{sus}}$), and $\lambda_{p,\mathrm{sus}}$ in suspended SLG are obtained as 4.286 GW/m^2-K, 2235 W/m-K, and 332 nm, respectively, as in Fig. 2.2(a). The discrepancies from other experimental and theoretical studies (reported $k_{0,\mathrm{sus}}$ = 3000-5000 W/m-K [18, 19, 52], $G_{B,\mathrm{sus}} = 4.167$ GW/m^2-K [88], and $\lambda_{p,\mathrm{sus}} = 750$ nm [54]) are attributed to the limited size and approximations in MD simulations and AIREBO model [91, 87, 92]; however, overall phonon properties and transport behaviors are reproduced well with our current approaches [93].

The in-plane thermal conductivities of SLG in the supported and sandwiched structures (k_{sup} and k_{sw}) are calculated, and their length dependence for relatively short-size range (< 150 nm, due to the computational cost) is also studied. As in Fig. 2.2(b), thermal conductivity is dramatically reduced by the contact with a Si substrate in the supported structure; however, the interaction with additional contact surface in the sandwiched structure does not have a significant effect on k. k_{sw} is slightly smaller than k_{sup}, and their length dependences are also similar to each other, showing that both relative thermal conductivities compared with the suspended SLG (i.e., $k_{\mathrm{sup}}/k_{\mathrm{sus}}$ and $k_{\mathrm{sw}}/k_{\mathrm{sus}}$) decreases with $d_{H\text{-}C}$ [Fig. 2.2(c)].

The high thermal conductivity of suspended SLG is attributed to a larger density of states (D_p) of out-of-plane modes [54] (ZA and ZO) at low energies, which results in higher c_p, and low phonon scattering rates of those phonon modes (Z: z-direction polarization, A: acoustic,and O: optical). The low scattering rates originate from the fact that approximately 60% of the normal (N) and Umklapp (U) scattering of the out-of-plane phonons are prohibited by the selection rules; thus, long mean free path of ZA and ZO phonons in comparison with the in-plane phonons [58] leads to dominant contribution to in-plane thermal conductivity of suspended graphene (more than 77% [54]). However, these ZA and ZO phonons are significantly affected by the contact, whereas in-plane phonons with LA, TA, LO, and TO polarizations (L: longitudinal, and T: transverse) show only a slight change as D_p's for in-plane and out-of-plane modes in suspended and supported graphene shows in Fig. 2.4(a). In particular, the ZA mode in supported or sandwiched graphene does not have

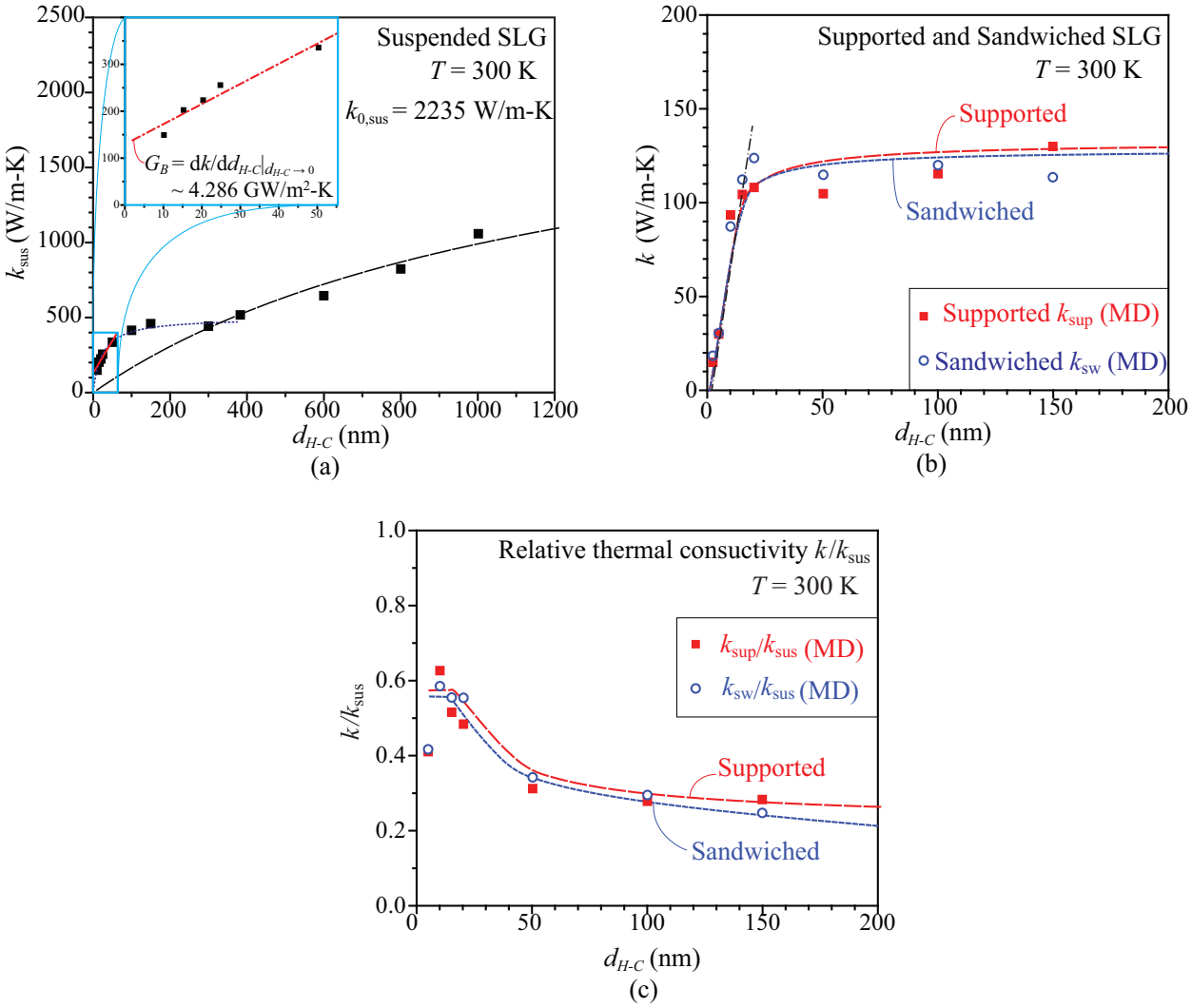


Figure 2.2: (a) Thermal conductivity of suspended graphene (k_{sus}) with respect to the distance between hot and cold reservoirs ($d_{H\text{-}C}$). The bulk conductivity of suspended graphene ($k_{0,\mathrm{sus}}$) and the ballistic conductance ($G_{B,\mathrm{sus}}$) are estimated from the length dependence. (b) In-plane thermal conductivities of the supported (k_{sup}) and sandwiched (k_{sw}) single-layer graphene with respect to $d_{H\text{-}C}$. (c) Relative thermal conductivities in supported and sandwiched graphene compared with suspended graphene ($k_{\mathrm{sup}}/k_{\mathrm{sus}}$ and $k_{\mathrm{sw}}/k_{\mathrm{sus}}$). Thermal conductivity is reduced by the interaction with Si, and the reduction increases with $d_{H\text{-}C}$.

nonzero D_p at phonon energy of zero any more, while the suspended graphene does due to the quadratic dispersion by flexural bending rigidity [94]. Since low-energy (long-wavelength) ZA phonons have less scattering rates or longer relaxation time [95], the smaller population of near zero energy phonons will cause a shorter average effective mean free path (λ_p), reducing thermal conductivity. Additionally, the ZO mode is shifted to the energy of substrate Si optical mode peaks by the cross-layer interaction, which also enhances scattering with substrate phonons. Compared to the clear difference between suspended and supported D_p's in out-of-plane polarization, additional contact in the sandwiched structure has a minor effect on phonon spectrum as in Fig. 2.4(b). The relative contribution of each phonon polarization (in-plane or out-of-plane) to thermal conductivity [Fig. 2.4(c)] shows that out-of-plane phonon contribution is dominant in in-plane thermal transport of suspended graphene, while in-plane phonons carry most of thermal energy in supported and sandwiched cases. This confirms that the dramatic reduction of thermal conductivity stems from increased scattering of out-of-plane phonons. Very close participation percentage of xy and z phonons in supported and sandwiched graphene and analogous D_p's for these cases, can explain the small difference between supported and sandwiched graphene in-plane thermal conductivity.

Using D_p in Figs. 2.4(a) and 2.4(b) with the equilibrium phonon (Bose-Einstein) distribution function $\{f^o_{\mathrm{BE}}=[\exp(\hbar\omega/k_{\mathrm{B}}T)-1]^{-1}\}$, the phonon specific heat capacities (c_p) of suspended and supported SLGs are calculated as

$$c_p = \int_0^\infty E_p \frac{\partial f^o_{BE}}{\partial T} D_p(\omega) d\omega = \int_0^\infty \frac{\hbar^2\omega^2}{k_{\mathrm{B}}T^2} \frac{\exp(\hbar\omega/k_{\mathrm{B}}T) D_p(\omega)}{[\exp(\hbar\omega/k_{\mathrm{B}}T)-1]^2} d\omega, \tag{2.5}$$

where k_{B} is the Boltzmann constant. The c_p of SLG does not vary dramatically with different structures; moreover, the out-of-plane modes in the supported case have slightly higher c_p than the suspended at temperatures around 300 K in spite of its lower k_{sup} as in Fig. 2.4(d).

Since the phonon conductivity k is proportional to c_p, u_p (average velocity) and λ_p according to the kinetic theory [96], we can conclude that the large reduction in k is mainly due to the increasing phonon scattering (shorter λ_p). The phonon mean free path (λ_p) increases with the time constant of phonon scattering (τ_p), which decreases with more scatterings. In the simulation of supported graphene, SLG phonons are scattered by other

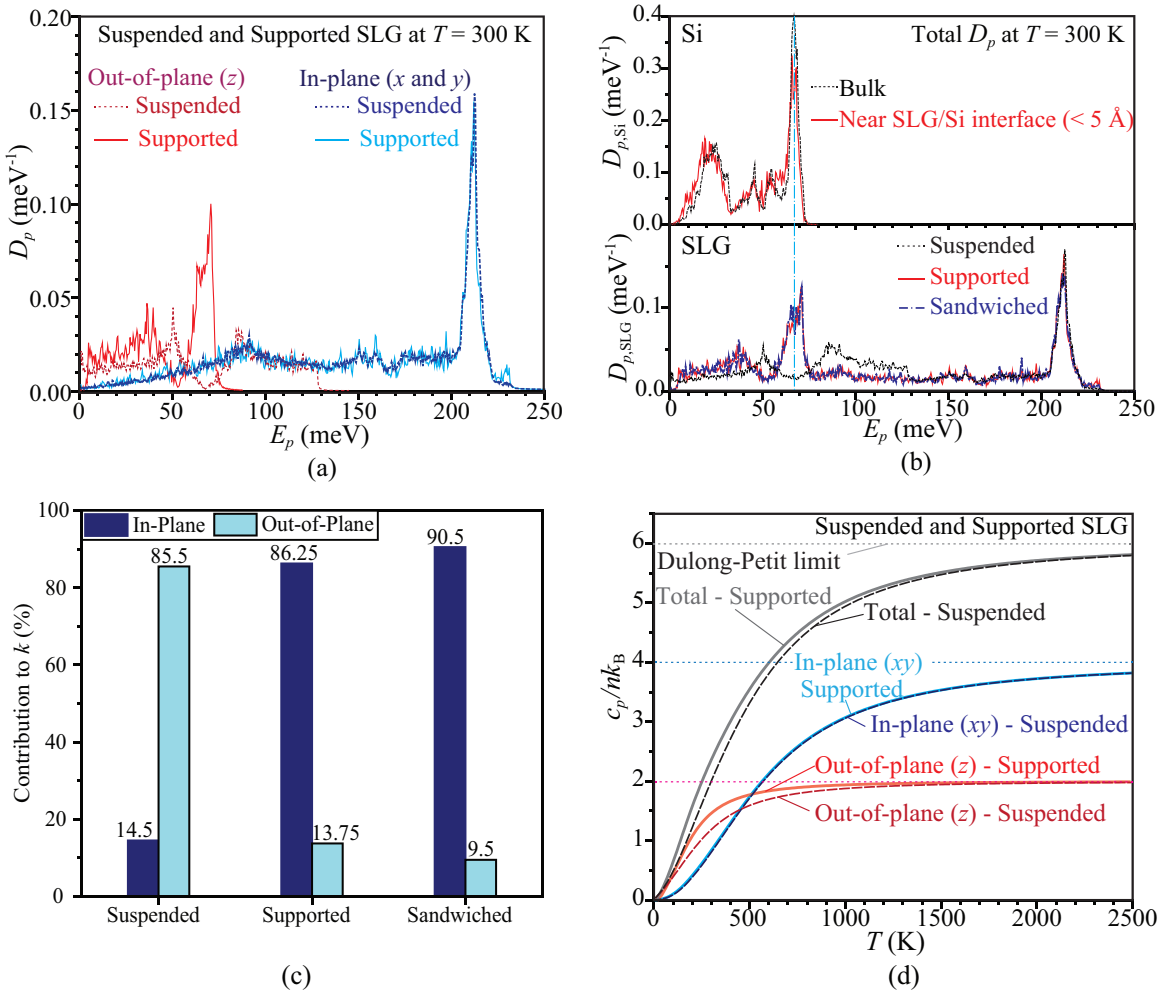


Figure 2.3: (a) Comparison between the suspended and supported phonon density of states (DOS, D_p) for in-plane and out-of-plane phonon modes. Differing from in-plane phonons, D_p in out-of-plane phonon modes (ZA and ZO) is significantly changed. (b) Total phonon DOS of suspended, supported, and sandwiched graphene. D_p of bulk Si and Si near the interface with graphene are also added. The supported and sandwiched D_p's are slightly different, and the cross-plane interaction shifts D_p's in both cases to Si D_p. (c) Relative contributions of in-plane and out-of-plane phonons to the in-plane thermal conductivity. The out-of-plane phonon contribution reduces by the interaction with the substrate. (d) Phonon specific heat capacities (normalized by nk_B) calculated for the suspended and supported SLGs using D_p's in Figs. 3(a) and (b).

SLG phonons (p-p), substrate interaction (p-sub), and thermostats (p-d, due to the limited transport distance, $d_{H\text{-}C}$), and these scattering mechanisms are characterized by three time constants; $\tau_{p\text{-}p}$, $\tau_{p\text{-}sub}$, and $\tau_{p\text{-}d}$, respectively. Using the Matthiessen rule [1], the overall time constant of phonon scattering (τ_p) is given as

$$\frac{1}{\tau_p} = \sum_j \frac{1}{\tau_{p,j}} = \frac{1}{\tau_{p\text{-}p}} + \frac{1}{\tau_{p\text{-}sub}} + \frac{1}{\tau_{p\text{-}d}}. \tag{2.6}$$

Here, $\tau_{p\text{-}d}$ increases with sample size ($d_{H\text{-}C}$), while other main mechanisms are not size-dependent; thus, with a longer $d_{H\text{-}C}$ (or $\tau_{p\text{-}d}$), the relative contribution of $\tau_{p\text{-}sub}$ and $\tau_{p\text{-}p}$ to overall τ_p is more significant. Since the shorter λ_p (or larger scattering rate) for lower k in the supported or sandwiched structures originates from the increased p-p or p-sub scattering when considering a common $d_{H\text{-}C}$, the change in conductivity by substrate $[(k_{\text{sus}} - k_{\text{sup}})/k_{\text{sus}}]$ increases with $d_{H\text{-}C}$ (i.e., $k_{\text{sup}}/k_{\text{sus}}$ decreases). This negative length-dependence of relative conductivity is observed both in the supported and sandwiched structures as in Fig. 2.2(c).

The phonons in the supported and sandwiched SLGs have almost identical DOS [Fig. 2.4(b)] (thus, very similar c_p) and ballistic conductance from the similar linear dependence for a very short length of system [Fig. 2.2(b)]. Thus, a minor difference between k_{sup} and k_{sw} despite additional substrate demonstrates a small difference between the supported and sandwiched SLG scattering rates. This small difference implies that the substrate scattering ($\tau_{p\text{-}sub}$) is not significant although it can further reduce k, and the additional contact in the sandwiched structure increases only the minor substrate scattering. Therefore, we deduce that through the contact with a single substrate, the SLG loses its 2D characteristics (including the flexural bending motion and the mentioned prohobitions in selection rules), which results in low p-p scattering rate (especially in out-of-plane modes) for higher k's. The extensive change in the out-of-plane phonon modes, which have dominant contributions to the in-plane thermal transport in suspended SLG, and the minor difference between the supported and sandwiched phonon properties explain the k reduction (large reduction from the suspended one but the minor difference by additional substrate) in Figs. 2.2(b) and 2.2(c).

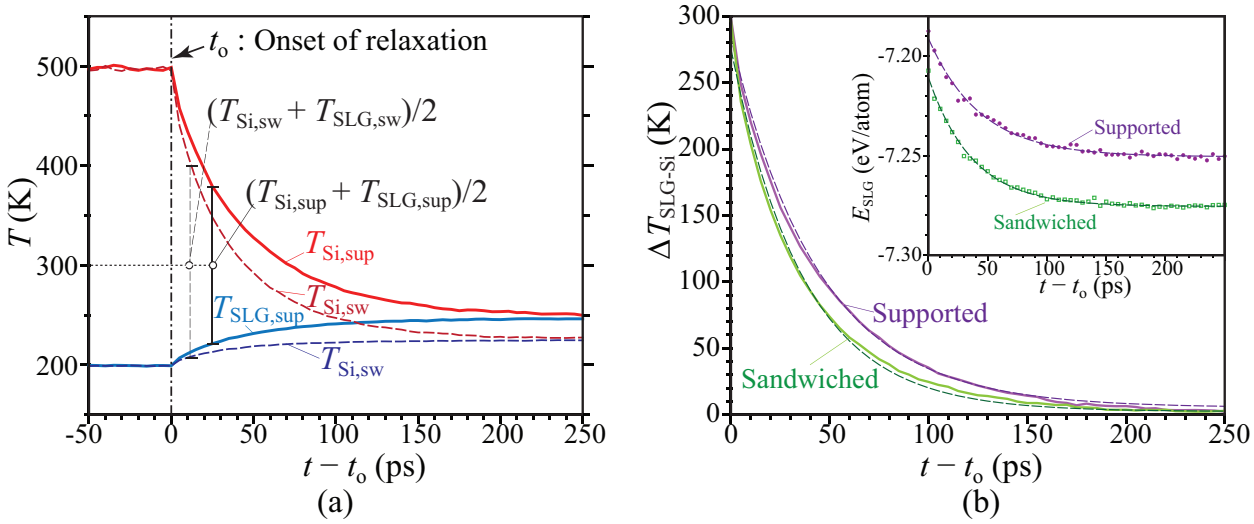


Figure 2.4: (a) Temperature evolution of SLG and Si during thermal relaxation. (b) The decays in temperature difference ($\triangle T_{SLG\text{-}Si}$) and the energy in graphene (E_{SLG}) (inset). The equilibrium temperature in the sandwiched structure is lower than the supported due to its doubled Si mass or doubled heat capacity, and the relaxation is also faster in the sandwiched structure due to the larger contact area.

Thermal relaxation between hot SLG and cold Si is analyzed for the cross-plane thermal transport. The resulting equilibrium temperature in the sandwiched structure is lower than the supported due to its doubled Si mass or doubled heat capacity as shown in Fig. 2.4(a). The decays in temperature difference ($\triangle T_{SLG\text{-}Si}$) and the energy in graphene (E_{SLG}) are fitted to exponential function eliminating the noise from MD results. Using this fitted equation with Eq. (3), thermal boundary resistance ($R_{SLG/Si}$) is calculated using Eqs. (2) and (3) and the fitting parameters are adjusted in a way not to affect the simulation results [Fig 2.4(b)].

The interfacial thermal resistance near the room temperature is almost constant in this range of temperatures as in Refs. [64, 85, 83, 84], and our calculations also show that the $R_{SLG/Si}$ is almost consistent during the relaxation despite a variation of average interfacial temperature $[(T_{Si} + T_{SLG})/2]$. The minor temperature dependence of interfacial transport in spite of a larger population of participating phonons at higher temperatures demonstrates the dominance (high interfacial transmission) of low-frequency phonons, excited already at low temperatures. The high transmission of low-frequency phonons is observed also in other graphene heterostructures [97, 98].

For the accuracy in the calculation of $R_{\mathrm{SLG/Si}}$ at 300 K, we select data points around $[(T_{\mathrm{Si}} + T_{\mathrm{SLG}})/2]$ of 300 K. The calculated $R_{\mathrm{SLG/Si}}$ in the supported case is 3.502×10^{-8} m^2-K/W, which is in a good agreement with previous reports (3.57×10^{-8} m^2-K/W through Raman method [99] and 3.52×10^{-8} m^2-K/W in other MD simulations [100]). As Fig. 2.4(b) shows, thermal relaxation in the sandwiched structure requires less time than the supported case; however, the calculated $R_{\mathrm{SLG/Si}}$ (4.98×10^{-8} m^2-K/W) is larger than the supported one, and the faster decay in $\triangle T_{\mathrm{SLG\text{-}Si}}$ and E_{SLG} is attributed to the doubled interfacial area. Although the additional contact in the sandwiched structure does not make a significant change in the phonon spectrum and in-plane conductivity of SLG compared to the supported, more scatterings at the interface are induced by stronger interaction with Si from both sides, leading to a larger $R_{\mathrm{SLG/Si}}$ in the sandwiched structure.

The different effect of the interaction by additional contact on in-plane thermal conductivity and cross-plane resistance implies the possibility of the anisotropic control of thermal transport in SLG/Si heterostructure through the control of the cross-plane (i.e., out-of-plane direction) interaction. In this study, pressure normal to the interface (p), ranging from 0 to 2.6 GPa, is applied for the transport control in the sandwiched structure (Si/SLG/Si).

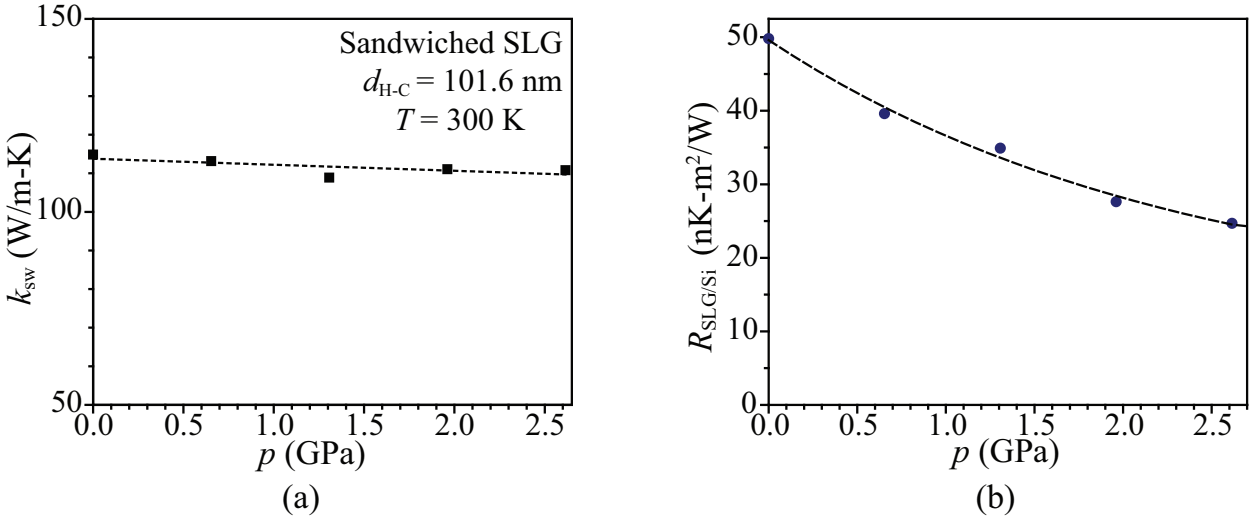


Figure 2.5: Variations of (a) in-plane thermal conductivity of SLG (k_{sw}) and (b) cross-plane interfacial thermal resistance ($R_{\mathrm{SLG/Si}}$) in the sandwiched structure (Si-SLG-Si) with respect to the applying pressure (p). $R_{\mathrm{SLG/Si}}$ decreases as p increases while k_{sw} does not vary significantly.

The in-plane thermal conductivity of the sandwiched SLG slightly decreases with increasing p, demonstrating minor effects of p on k_{sw} as in Fig. 2.5(a). k_{sw} from the MD simulation under 2.6 GPa to the interface is 3.5% lower than without pressure, and the reduction using k_{sw} from the linear fitting is 2.1%. In contrast, $R_{\mathrm{SLG/Si}}$ significantly decreases with increasing p (2.6 GPa reduces by around 50%) [Fig. 2.5(b)] as expected and observed also in multi-layer graphene [63]. This suggests the anisotropic thermal transport control (selective enhancement of cross-plane thermal transport) by applying p.

The p-increase reduces the distance between C in SLG and Si atoms in general; thus, a larger number of Si atoms are located within shorter distances with C atoms as shown in Fig. 2.6(a). The shorter distance induces a stronger interaction between C and Si, which is represented by the LJ potential. The average distance between the sandwiched SLG and the Si block is reduced by 7% in the presence of the pressure of 2.6 GPa, compared to one with no pressure ($p = 0$ GPa). D_p of phonons with in-plane polarization, which is perpendicular to the pressure- (or force-) applied direction, does not vary with pressure as expected and shown in Fig. 2.6(b). In contrast, the phonon spectrum in the p-applied (out-of-plane or z) direction shows an additional low-energy peak in both the sandwiched SLG and interfacial Si as in Figs. 2.6(c) and (d). As p increases, this peak increases and D_p's of SLG and Si are more synchronized. The stronger interaction and applied pressure constrain the motions of constituent atoms neighboring the interfaces, analogous to linkage to very heave mass, which we attribute the appearance and increase of low-energy phonon peak to.

The peak is sharp and narrow, and its size in Si diminishes as the distance from the interface increases [Fig. 2.6(e)]; thus, we deduce that the phonon is localized (or not propagated) in the out-of-plane direction. Additionally, the out-of-plane mode, which the peak belongs to, has a minor contribution to in-plane thermal transport as in Fig. 2.4(c), and the in-plane thermal conductivity is decreasing despite an increased phonon population by larger density of state at the peak. Therefore, the low-energy phonons in the peak do not contribute to in-plane thermal transport, being localized. On the contrary, this low-energy vibration excitation in both Si and graphene can provide additional transport channels, enhancing local cross-plane interfacial transport.

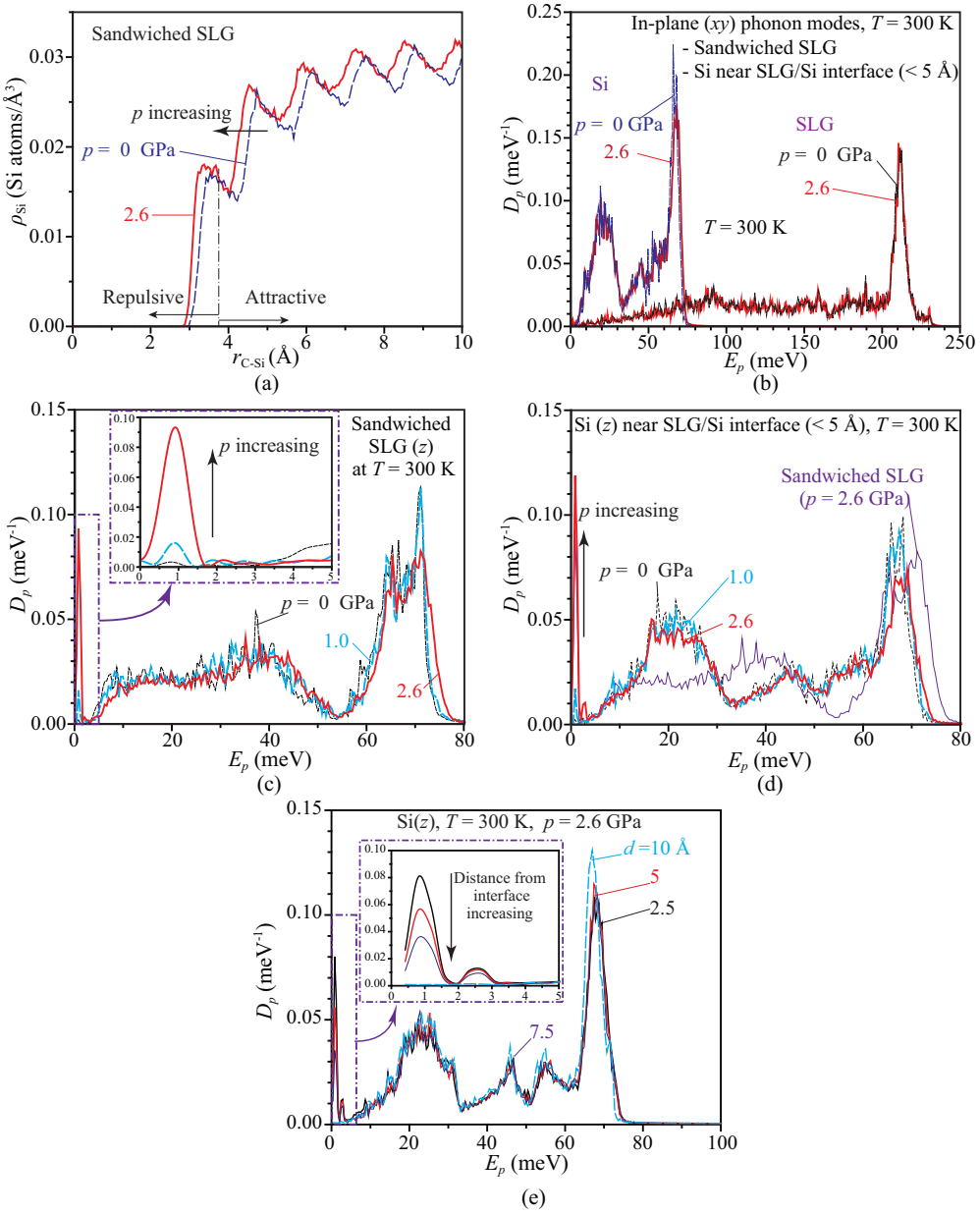


Figure 2.6: (a) Atomic density distribution of Si with respect to the distance with C atoms. The increase in p decreases the average distance between C and Si, which induces the stronger interaction. (b) D_p's of phonon modes polarized in the in-plane directions (xy) in the sandwiched SLG and interfacial-region Si under two different p's (0 and 2.6 GPa). (c) Out-of-plane D_p's in the sandwiched SLG under the pressures of 0, 1.0 and 2.6 GPa. (d) D_p's of phonon mode polarized in the cross-plane direction (z) in the interfacial-region Si with respect to p (the out-of-plane D_p in the sandwiched SLG under the maximum pressure is added as a reference). While the in-plane phonons do not change with p, out-of-plane phonons in both interfacial Si and SLG have additional low-energy peaks in D_p, which increases with p. (e) D_p's of silicon at different distances from the interface (p=2.6 GPa). The peak near zero energy disappears after few layers of atoms far from the interface.

As discussed above, phonons with long wavelength (low frequency) dominantly contribute to thermal transport due to their high transmission across interfaces and this additional channel enhances the cross-plane thermal transport vividly; thus, the larger peak by higher pressure at the interface can lead to the lower interfacial resistance. Our additional simulations show that increasing ε (characterizing the Si-SLG interaction strength) in the LJ potential induces similar effects of increasing p; a low-energy peak appears and increases with ε, in-plane D_p is almost invariant, and in-plane thermal conductivity (k_{sw}) slowly decreases while the decrease in interfacial thermal resistance ($R_{\mathrm{SLG/Si}}$) is significant as shown in Figs. 2.7(a) and (b). However, large ε is required to have similar extent of change in phonon D_p and transport (e.g., five times larger ε leads to similar results of 1.0 GPa, ε_0 is the LJ potential parameter from UFF model by Rappe, et al. [70]), and very large ε ($> 10\varepsilon_0$) causes a large deformation of Si crystal structure near the interface. Therefore, pressure control is more feasible in engineering, and more effective without undesirable effects (such as unstable interfacial structures) than control of interaction strength.

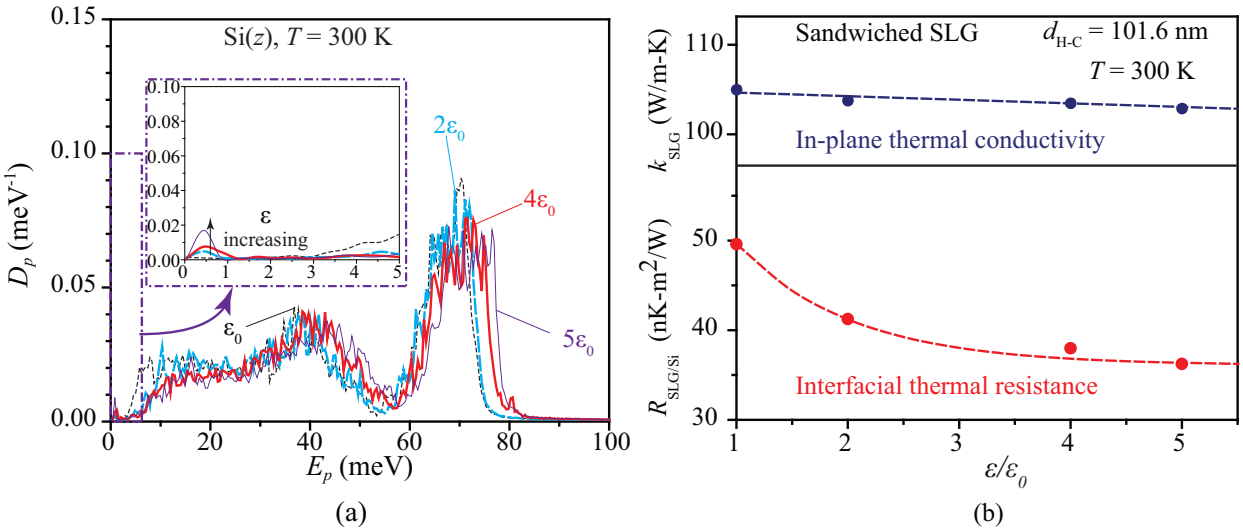


Figure 2.7: (a) Out-of-plane phonon D_p's in the sandwiched SLG using different interaction strength (ε). (b) In-plane thermal conductivity (k_{SLG}) and interfacial thermal resistance ($R_{\mathrm{SLG/Si}}$) in Si/graphene (SLG)/Si structure with respect to interaction strength.

2.5 Conclusions

Phonons polarized in out-of-plane direction are significantly influenced by the cross-plane interaction with a contacting substrate, while in-plane phonons are almost intact. The substrate effect is expected to activate the phonon scattering modes especially involving out-of-plane modes, which are prohibited in suspended 2D graphene, reducing the mean free path and thermal conductivity as a result. The additional contact surface in the sandwiched structure increases the substrate interaction in the out-of-plane direction, and applying a pressure induces the change in out-of-plane phonon modes; however, the change in conductivity (k) is not significant, indicating the minor effect of the cross-plane interaction control on the in-plane thermal transport of heterostructured graphene since the thermal energy is transported dominantly by in-plane phonons, which are almost invariant with pressure application. In contrast, the graphene/Si interfacial transport can be effectively controlled by the cross-plane interaction, thus the variation in out-of-plane phonon mode. Applying the pressure for the interaction control creates the additional low-frequency transport channel in the out-of-plane mode, which effectively reduces interfacial thermal resistance (by 50% with 2.6 GPa, while in-plane conductivity reduces by 3.5%).

This study offers insights on thermal transport properties in graphene heterostructures, which can be employed for the thermal system design and analysis of graphene devices. Effective, anisotropic thermal transport control proposed in this research is beneficial in many engineering applications, such as space fission propulsion/power systems [6], electronic circuits [38], and energy storage systems [5]. In a future study, thermal transport with different temperature and substrate, which leads to a different phonon mismatch and cross-plane interaction, and the phonon kinetics in those systems can be further studied for the enhanced understanding.

Chapter 3

Heat Flow Diversion in Supported Graphene Nanomesh

A version of this chapter was originally published by Ali Yousefzadi Nobakht, Seungha Shin, Kenneth D Kihm, Drew C Marable, and Woomin Lee:

Yousefzadi Nobakht, Ali, et al. "Heat flow diversion in supported graphene nanomesh." Carbon 123 (2017): 45-53.

3.1 Abstract

Redirection of energy carrier propagation by geometric confinement is studied through the analysis of in-plane and cross-plane thermal transport within various graphene nanomesh (GNM) configurations using molecular dynamics (MD) simulations. As the transport channel width decreases with an increase in porosity, the effect of redirection increases; thus, the in-plane thermal conductivity of large-porosity GNM is more dependent on hole arrangement. Since higher porosities weaken the GNM structure due to a larger population of broken bonds, carbon atoms within the graphene structures are more easily influenced by interactions with the substrate silicon (Si) block. Subsequently, increase in porosity leads to the decrease of interfacial thermal resistance. At higher porosities, lower interfacial resistance and in-plane thermal conductivity cause diversions (and redirections) in heat flow from the GNM to the underlying Si substrate. Our study suggests that this method of heat flow redirection can be applied as an effective means to control and manage heat transfer within numerous applications; extension to the improved conductivity calculation accuracy can also be achieved through the inclusion of this diversion analysis.

3.2 Introduction

Since graphene's first successful isolation [15], and the identification of its high electrical [51] and thermal [18, 19] conductivity properties, these characteristics have made this novel material very promising for advancement and innovation within electronic applications [101, 102, 103, 104]. Many research efforts have explored extensions of graphene's highly desirable attributes to more diverse and broader applications by manipulating its properties (e.g., boosting desirable and suppressing undesirable properties). Controlling thermal transport (i.e., direction and magnitude) is of great interest for energy conversion and electronic system design, with thermoelectric (TE) energy conversion being one such example of manipulation [29, 30, 31, 32]. For optimal performance within TE devices, the reduction of thermal conductivity (k), while maintaining or enhancing the TE power factor ($\sigma_e S^2$, σ_e: electrical conductivity and S: Seebeck coefficient), is critical. Moreover, the direction of heat transfer can be controlled by altering thermal transport properties; utilization of such methods can be employed to enhance heat dissipation [105].

Previous efforts to manipulate the thermal conductivity of graphene have emphasized the use of chemical approaches to introduce defects and/or functional groups as an avenue to control resultant thermal properties [106, 107, 108, 109, 77]. Defects increase phonon scattering to thereby suppress thermal transport; however, defects are difficult to control and their effect on thermal transport is reported to be minor when defect concentration is large [110, 111]. Moreover, defects parasitically degrade other desirable properties (e.g., electrical conductivity in TE applications) [106]. Edge passivation [112], isotope engineering [45], strain [113], and grain boundary [109, 114] have also been considered for thermal transport control; among the various methods, the technique of geometrically modifying or constricting a graphene sheet is suggested as one of the most feasible and affordable methods [42] to effectively control thermal transport [115]. The use of graphene nanomesh (GNM), which contains nano-sized periodic holes on a graphene sheet, is one such example representative of the application of geometric constraints towards effective thermal transport control [116, 43]. Due to their tunable bandgap through adjustment of pore size and periodicity, GNM presents

itself as an excellent candidate for thermoelectric energy conversion [117] and field-effect transistors [116, 102, 103, 118], energy storage [119], as well as gas detection [120, 121].

Recent studies utilizing molecular dynamics (MD) have primarily investigated free-standing GNM, whereas experimental studies and applications mainly employ GNM within supported/sandwiched form [116, 122, 120, 121]. As the presence of a substrate is known to greatly influence thermal behaviors of single-layer graphene (SLG) and graphene nanoribbon in a dramatic way [123, 124, 45, 125, 32, 126] studying GNM in a supported form provides more accurate insight to thermal transport behaviors within applications. In the study of supported GNM, Si is selected as a substrate material to achieve maximized heat diversion effect (due to its high thermal conductivity), and because of our continuing interest in Si-supported graphene [46] and wide engineering applications (e.g., detectors in aqueous environments [127], Schottky junction solar cells [128], and photonics [129]). Hole arrangement and porosity are controlled in suspended and Si-supported GNM; their effects on thermal transport, and the underlying physics of said effects, are examined.

3.3 Simulation Methods

Periodic boundary conditions are applied in the y-axis direction, while fixed and free boundary conditions are used for the x- and z-axis directions (to avoid interactions between periodic cells), respectively. Here, x and y are in-plane directions, and heat flows in the x direction (Figs. 3.1a-3.1c). A sample length (l in x direction) of 47.2 nm and a width (w in y direction) of 23.4 nm are selected to minimize lattice mismatch in Si/SLG heterostructures. The Si block length and width are of the same dimensions as the graphene sheet; the height of the Si block is 38.0 nm in the z-axis direction. Adaptive intermolecular reactive empirical bond order (AIREBO) [66] potential is used to model C-C bonded interactions, and the three-body Stillinger-Weber [67] potential is employed for modeling Si-Si interactions. Short-range van der Waals (vdW) interactions [68, 69] between C and Si atoms are modeled by the 12−6 Lennard-Jones (LJ) potential, $\varphi_{LJ} = 4\varepsilon[(\sigma/r)^{12} - (\sigma/r)^{6}]$, where ε is the minimum energy, σ is the distance at which the intermolecular potential between the two particles is zero, and r is the distance of separation between particles. The potential parameters used in

our simulations are based on the vdW interactions in the universal force field (UFF) model by Rappe et al. [70]. All simulations were performed using Large-scale Atomic/Molecular Massively Parallel Simulator (LAMMPS) [65]; the total simulation time and time step size for all simulations are chosen to be 2.5 ns and 0.5 fs, respectively. In this work, reported results are the average of five independent simulations.

Two different arrangements of holes [square (SA) and zigzag (ZA)] are employed within this research (Figs. 3.1a and 3.1b). In each simulation, hole sizes are uniform and the radius ranges from 0 to 28.5 Å, while the hole center positions are fixed; thus, the porosity (of the simulation cell central region) is controlled up to 75%. With the maximum possible porosity being 78.5%, to avoid potential tearing and distortion of the graphene sheet structure, we select a porosity of 75% as the maximum investigated porosity size. With various hole arrangements and porosities, we investigate in-plane thermal transport in both stand-alone and Si-supported GNMs, as well as cross-plane transport in Si/GNM systems.

Thermal transport, characterized by conductivity and conductance (or resistance), is evaluated by determining resultant heat flow and temperature distributions under non-equilibrium temperature settings [75, 76, 77]. Initial equilibration is performed for 0.5 ns in the NVT ensemble (constant number of particles, volume, and temperature) to rescale velocities to a prescribed temperature. After equilibration is complete, four layers of atoms are fixed at both ends of the structure (x- and y-axis directions); hot and cold Langevin thermostats are then applied next to these fixed regions so to generate a heat flux in the direction marked by arrows in Figs. 3.1a-3.1c [42, 112, 76]. Thermal conductivity, k (W/m-K), is calculated by using Fourier's law, $\boldsymbol{q} = -k\nabla T$, the heat flux from the hot to the cold region, q (W/m^2), and the resulting temperature gradient, ∇T ($= dT/dx$ in 1D transport). q is the average heat addition/removal by the thermostats per unit cross-sectional area over a time span of 2.0 ns. For the cross-sectional area, the thickness of single-layer graphene is selected as the inter-layer spacing of graphite (0.335 nm [79]). In the determination of ∇T, local temperature is calculated from the ensemble average of local atomic energy over a sufficient period of time (1.0 ns) so to minimize noise within temperature distributions. Considering thermostating effects and temperature dependences on thermal transport, the

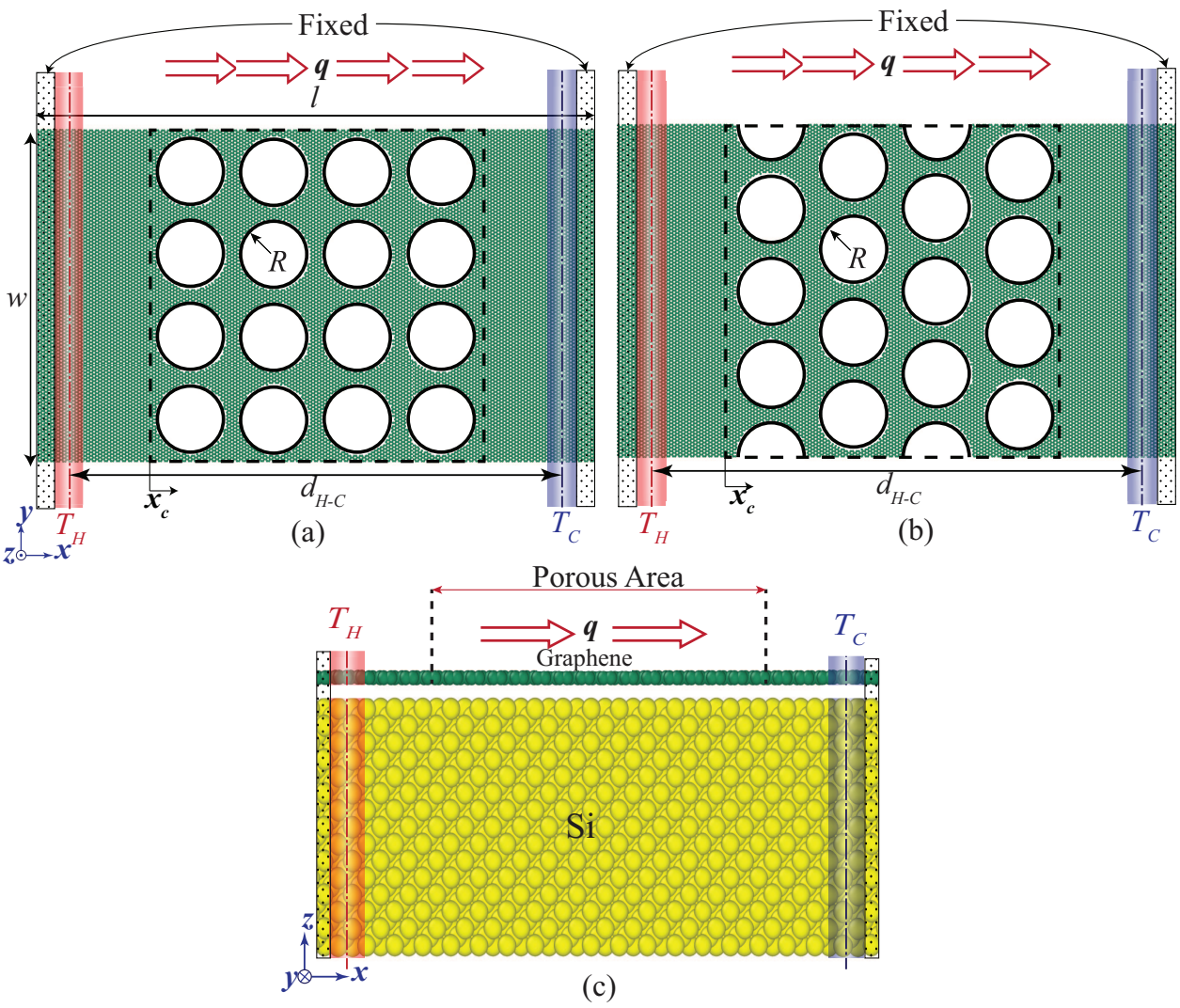


Figure 3.1: Simulation models for the calculation of thermal transport properties. (a) Square hole arrangement and (b) zigzag hole arrangement of GNM. (c) GNM with Si substrate (side view). Separate hot and cold thermostats are placed on Si and GNM.

linear portion near the prescribed T-value of the temperature profile is selected for our analyses.

In order to calculate the thermal conductivity of graphene with a Si substrate, hot and cold thermostats are separately placed on both graphene and Si as in Fig. 3.1c. In addition to using thermostat heat flow (q_T), heat flux along the graphene sheet and Si block is obtained from the ensemble average of the x component of heat flux ($q_{f,x}$), which is given by [79]

$$q_{f,x} = \frac{1}{V}[\sum_i \frac{1}{2} m_i(\boldsymbol{u}_i \cdot \boldsymbol{u}_i)u_{i,x} + \sum_i \varphi_i u_{i,x} + \frac{1}{2}\sum_i \sum_j x_{i,j}(\boldsymbol{u}_i \cdot \boldsymbol{F}_{ij})], \tag{3.1}$$

where V is the volume, m_i is the mass of particle i, $\boldsymbol{u}_i$ is the velocity vector, $u_{i,x}$ is the x component of $\boldsymbol{u}_i$, φ_i is the potential energy, x_{ij} is the x component of the interatomic separation ($\boldsymbol{r}$), and $\boldsymbol{F}_{ij}$ is the interaction force between i and j particles. To estimate the separate contributions of phonon modes to thermal transport, either the x and y components of vectors (for the in-plane contribution) or only the z components (for the out-of-plane contribution) are included in heat flux calculations (Eq. 1). To illustrate local heat flow direction and magnitude (Figs. 3.6a-3.6d), we divide the simulated GNM into small groups of atoms creating a 50×50 mesh grid (Fig. 3.2a) to capture all geometrical and heat flow details, as well as to ensure sufficient number of atoms for the statistically meaningful heat flux calculations. To find an appropriate mesh size, we tested different grid dimensions and calculated temperatures of hole edge cells with the smallest number of atoms (T_{cell}), which has potential for the largest deviations from a prescribed, overall temperature (T_{o}). The difference between selected cell and overall equilibrium temperature of a sample ($T_{\text{cell}} - T_{\text{o}}$) decreases as the mesh size and number of atoms in the cell increases; ultimately, this difference reaches almost zero when the cells contain a sufficient number of atoms for thermal analysis (Fig. 3.2b). The local heat flux vector is determined by applying Eq. (1) every time step and is averaged for 2.5 ns.

Cross-plane thermal transport across the GNM/Si interface is investigated by means of the temperature relaxation method [64, 81]. The GNM/Si system is first equilibrated at 300 K; hot and cold thermostats at 350 K and 250 K are then respectively placed on the GNM

and Si block in the NVE ensemble. After reaching steady-state, the thermostats are then removed to allow for thermal relaxation of the simulated structure.

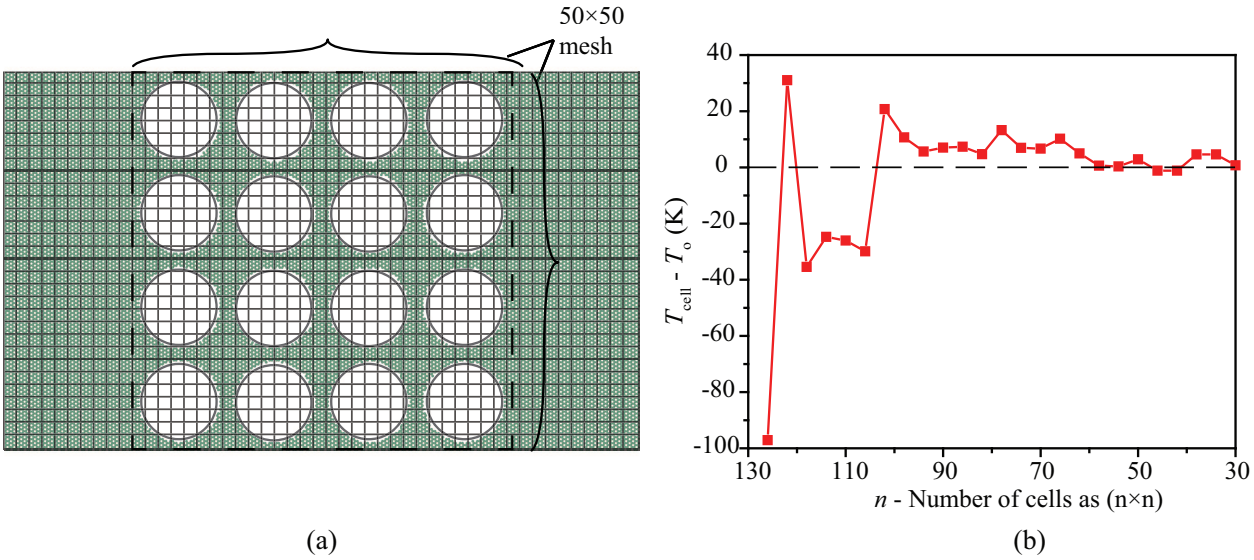


Figure 3.2: (a) Mesh structure for the local heat flux distribution in GNM. (b) The difference between calculated cell temperature and temperature of simulation sample ($T_{\text{cell}} - T_{\text{total}}$) with respect to number of meshes in each side of the dashed quare (n).

During this thermal relaxation period, temperature and energy changes of GNM and Si block are recorded; the interfacial thermal resistance, R (K/W) can be obtained by [64, 83, 84]

$$R = \frac{\int_0^t (T_{\text{GNM}} - T_{\text{Si}})dt}{E_t - E_0}, \tag{3.2}$$

where E_t is the total energy of the supported graphene, E_0 is the initial energy of GNM at the beginning of relaxation period, A is the thermal transport interface area, and T_{GNM} and T_{Si} are the GNM and Si temperatures.

In order to identify phonon behaviors within thermal transport of the GNM/Si system, phonon density of states (D_p) is calculated through the Fourier transform of the velocity autocorrelation function [86]. In addition, atomic density distribution (ρ) is determined as a representative parameter for the average distance between GNM and Si layers; this is performed by averaging the number of particles per unit volume during the temperature relaxation stage of simulations.

3.4 Results and Discussion

3.4.1 Suspended GNM

In MD, with a non-equilibrium temperature setting for in-plane thermal conductivity, the heat transfer path is comparable to the mean free path (MFP, 240–750 nm in graphene [19, 90]) of thermal energy carriers, i.e., phonons. Thus, the resulting thermal conductivity depends on the size of the simulation domain [130]; the thermal conductivity size dependence of pristine graphene has been extensively studied in our previous research [46]. The size dependence of GNM is also examined by comparing thermal conductivities from MD with two different porosities (ζ = 20% and 56%), and three different dimensions of simulation domain ($l/2, l$, and $2l$). As Fig. 3.3 demonstrates, although MD thermal conductivity of GNM increases with simulation domain size, it is much less sensitive to sample length (i.e., the length dependency is reduced) as porosity increases, which is attributed to an increasing dominance of boundary/edge scattering.

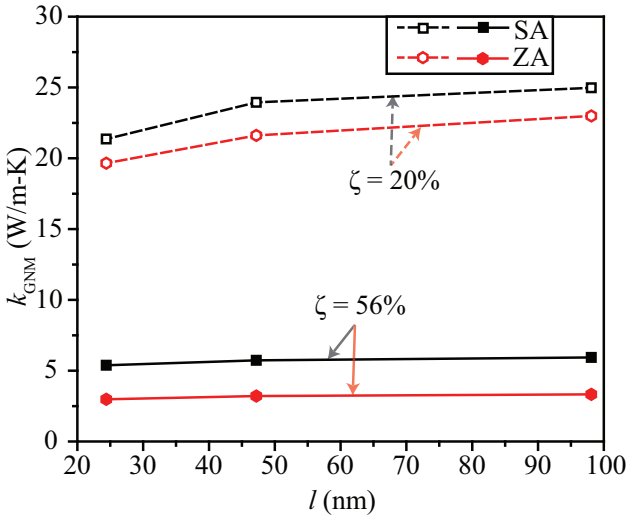


Figure 3.3: Size dependence of GNM thermal conductivity for three different sample length and two different porosity cases.

The in-plane thermal conductivity (k_{GNM}) significantly decreases with increasing porosity in both hole arrangements, as shown in Fig. 3.4a. This reduction of thermal conductivity, by increasing porosity, is more significant for larger samples due to a smaller size dependence at higher porosities (Fig. 3.3). This resulting porosity dependency is much greater than

predictions made by the classical (Eucken) model, where the ratio of thermal conductivity of a material with porosity (ζ), k_{GNM}, to its non-porous counterpart (same size GNM without pore, $k_{\mathrm{GNM,np}}$), is given by $k_{\mathrm{GNM}}/k_{\mathrm{GNM,np}} = (1-\zeta)/(1+\zeta/2)$ [131]. This classical model is developed based on the premise that a subject system is within the continuum (diffusive) regime, where system dimensions are much larger than the MFP, to allow for the Fourier's law-based assumption of constant thermal conductivity within a system. However, as transport channels (or neck sizes) in GNM are smaller than that of graphene MFP, ballistic size-dependent thermal transport (i.e., conductivity decreases as size decreases) induces excessive reduction of overall thermal conductivity [88]. Thermal conductivities of both hole arrangements are very similar to each other when their porosities are small ($<$ 20%); however, their difference is seen to increase with increasing porosity as in Fig. 3.4b. With a porosity of 75%, the thermal conductivity of the zigzag arrangement is found to be roughly half of that determined within the square arrangement. In consistency with another study [43], this implies that phonons within a narrowed channel due to a higher porosity are more influenced by hole arrangements. As hole edges appear on the path of phonon propagation, whose direction is limited by channel width, scattering is more frequent within the zigzag arrangement.

According to previous research [54], the high thermal conductivity of suspended SLG is attributed to a larger density of states at lower energies and lower phonon scattering rates of out-of-plane phonon modes, which produces the dominant contribution (more than 77%) made to the in-plain thermal conductivity of suspended graphene. Our relative thermal conductivity calculations of in-plane and out-of-plane phonon modes (Figs. 3.4c and 3.4d) also confirms the importance of out-of-plane phonon contributions to the in-plane thermal transport of defect-free SLG. However, the relative influence of out-of-plane phonons (k_z/k_{GNM}) is found to decrease as porosity increases; due to a longer phonon-phonon scattering MFP [132], pore induced phonon scattering more significantly obstructs the out-of-plane modes, and thus, reduces the total thermal conductivity.

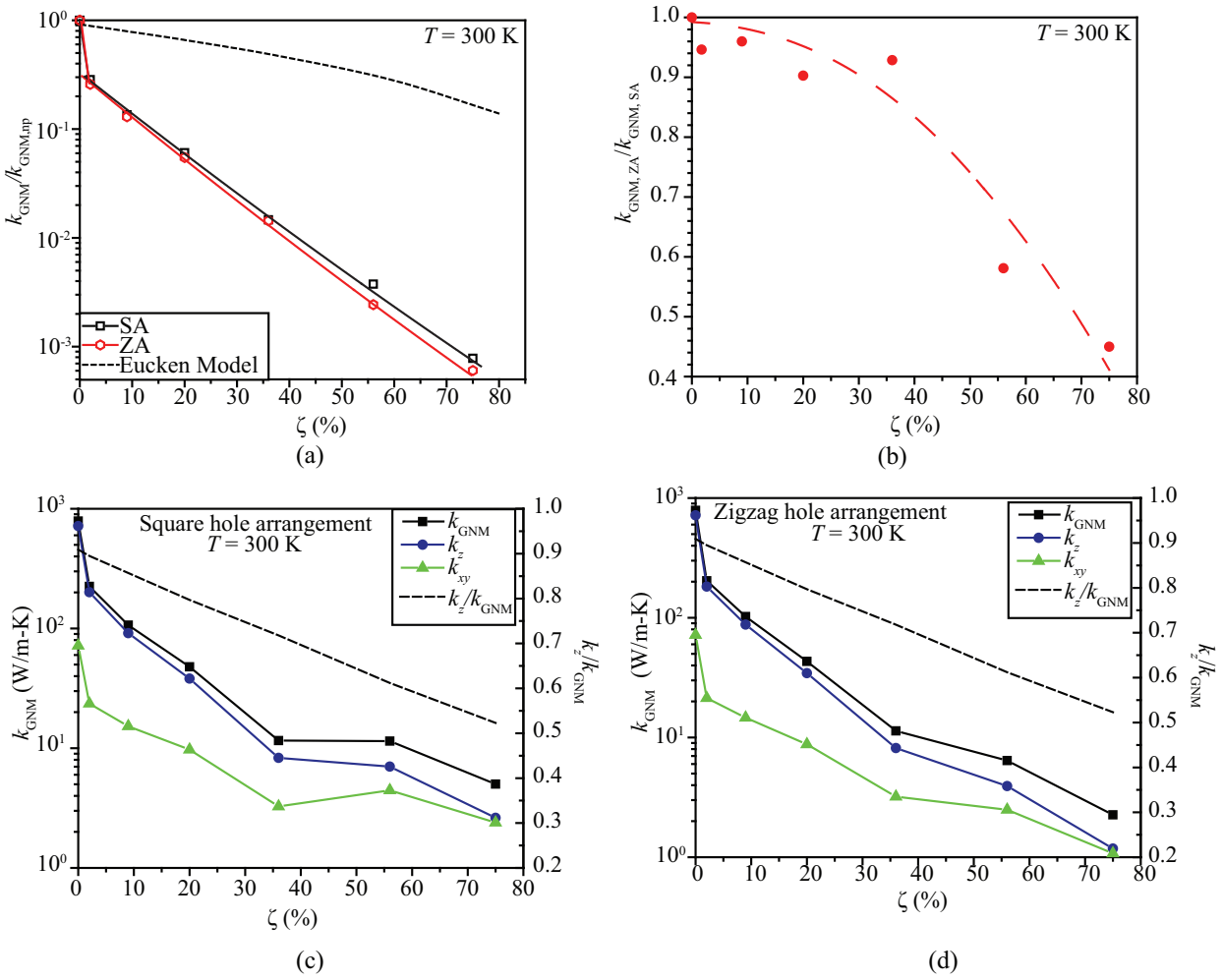


Figure 3.4: (a) Thermal conductivity of GNM with classical Eucken model, square (SA), and zigzag (ZA) hole arrangements with respect to porosity (ζ). (b) Relative GNM thermal conductivity of the zigzag hole arrangement as compared to that of the square hole arrangement ($k_{\mathrm{ZA}}/k_{\mathrm{SA}}$) with respect to porosity (ζ). Comparison of thermal conductivity in-plane (k_{xy}) and out-of-plane (k_z) phonon modes, and relative thermal conductivity of out-of-plane phonon modes (k_z/k_{GNM}) for (c) square hole arrangement (SA) and (d) zigzag hole arrangement (ZA).

For both hole arrangements, as relative contribution of temperature dependent phonon-phonon interactions to overall phonon scattering decreases with porosity, the temperature dependence of thermal conductivity is less significant at larger porosities. Without pores (defect-free, upper line in Fig. 3.5a), k decreases with temperature. However, this negative temperature dependence is alleviated as porosity increases; eventually, positive temperature dependence begins to emerge at a porosity of 50% (Fig. 3.5b) as the thermal conductivity peak (Umklapp peak) moves towards higher temperatures at larger porosities.

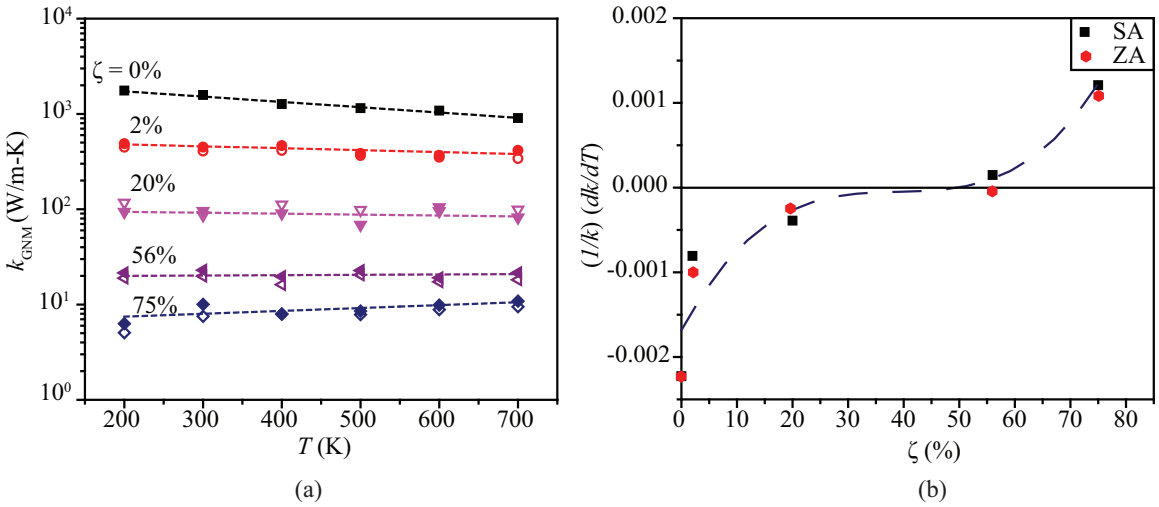


Figure 3.5: Temperature dependency of GNM in-plane thermal conductivity with square (filled shapes) and zigzag (outlined shapes) hole arrangements at various porosities (dashed lines are linear fit in logarithmic scale, which is exponential fit in linear scale). (b) Exponent of exponential fit (slope of the linear fit in logarithmic scale) of thermal conductivity changes with temperature for different porosities.

Figures 3.6a and 3.6c demonstrate the in-plane projection of local heat flux vectors in the two different hole arrangements under identical simulation conditions (hole radius of 25 Å and porosity of 56%). Although both cases share similar temperature distributions due to identical temperature settings, the square arrangement (Fig. 3.6a) shows a larger number of high-magnitude heat flux vectors than the zigzag arrangement (Fig. 3.6c); the average heat flux of the zigzag arrangement is roughly 76% of that determined for the square arrangement. Analysis of local heat flux vectors in polar coordinates illustrates that higher magnitude heat flux vectors are primarily concentrated within an approximately 30° difference from the heat flow direction (0°) in the square arrangement (Fig. 3.6b). Contrarily, GNM with zigzag hole arrangement (Fig. 3.6d) has a wider angular distribution of heat flux vectors and a lower

centralized density of higher magnitude vectors; this confirms the lower net heat flux in the x-axis direction than of that found in the square arrangement. Geometric constraints in the zigzag hole arrangement impose more frequent scatterings to phonons possessing wave vectors that align with the heat transfer direction ($-30^\circ \sim 30^\circ$); thus, contributions from these phonons will be suppressed, reducing the net heat flux as well as thermal conductivity.

3.4.2 Supported GNM

Due to additional scattering and loss of reflection symmetry (which significantly restricts the phase space for phonon-phonon scattering of z-axis direction phonons [58]) caused by the presence of a substrate, thermal conductivity of the supported graphene sheet is reduced to approximately 10% of that determined for suspended graphene (k_{sus}). This conductivity reduction caused by the presence of a substrate decreases as porosity increases. In other words, the ratio of supported GNM conductivity to suspended at the same porosity, $k_{\text{sup}}/k_{\text{sus}}$ linearly increases for GNM of both hole arrangements as shown in Fig. 3.7a ($k_{\text{sup}}/k_{\text{sus}} \sim 0.6$ at $\zeta = 76\%$). This indicates that the effect of substrate-induced scattering becomes less dominant in supported GNM with a higher porosity due to larger scattering rates caused by geometric constraints. In addition, Fig. 3.7b, where porous GNM thermal conductivity is compared with non-porous graphene under the same conditions (substrate and porosity), conveys that the porosity dependence of thermal conductivity (i.e., decreasing k with increasing ζ) is less significant in supported GNM systems than in suspended cases. As the influence is shared by both geometric constraints (holes) and substrate effects, each of these influences become weakened. We note that as in suspended systems, SA is still found to possess a higher conductivity than ZA in supported configurations. Porosity also influences thermal transport across the interface of Si/GNM systems. As porosity increases, the GNM/Si system reaches thermal equilibrium at a lower equilibrium temperature and at a quicker rate than systems with lower porosities (Fig. 3.8a). Despite area (A) reduction by increased porosity, interfacial thermal transport (R, K/W), calculated from the temperature relaxation method with Eq. (2), is shown to decrease (Fig. 3.8b); i.e., areal resistance (R'', m^2-K/W) decreases more quickly than the decrease in area. Here, hole arrangement does not affect cross-plane thermal transport.

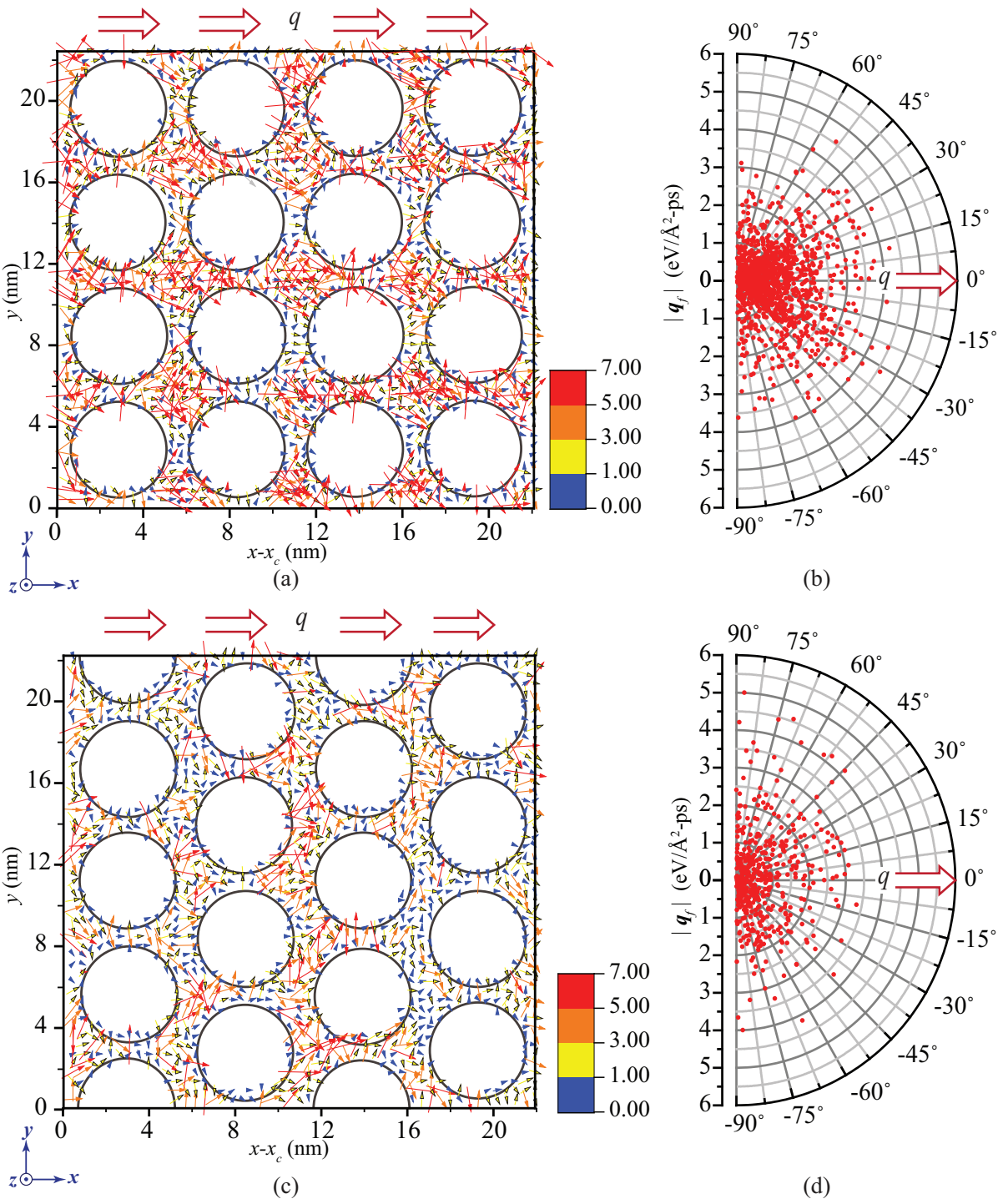


Figure 3.6: In-plane local heat flux distribution. (a) Heat flux distribution in the square hole arrangement GNM with hole radius of 25 Å. (b) Magnitude/angle distribution of the in-plane heat flux vectors within the square hole arrangement. (c) Heat flux distribution in the zigzag arrangement GNM with hole radius of 25 Å. (d) Magnitude/angle distribution of the in-plane heat flux vectors within the zigzag hole arrangement.

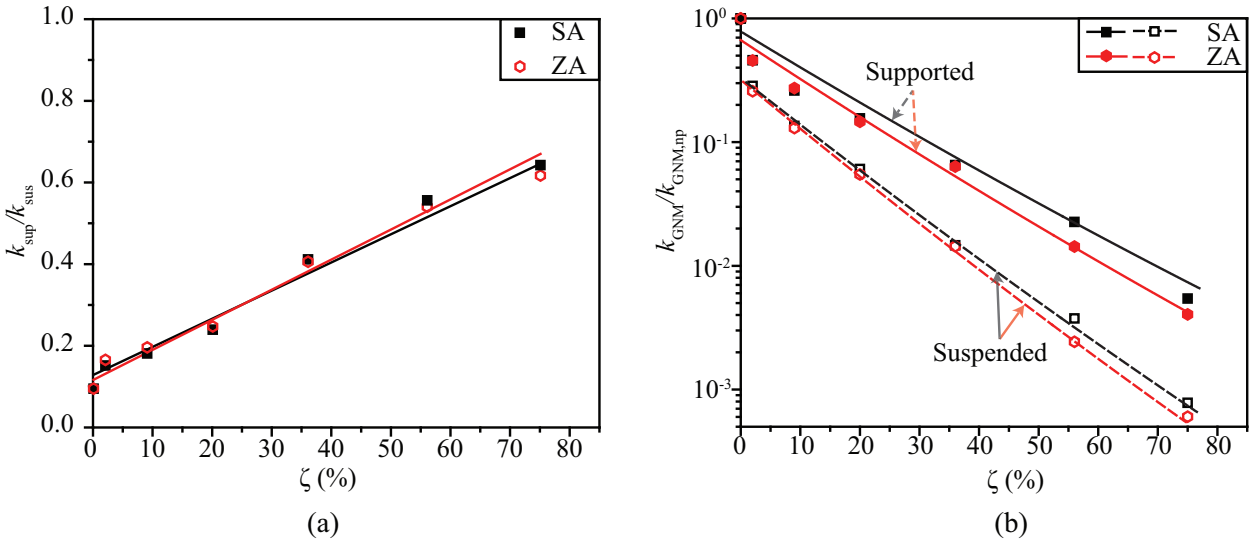


Figure 3.7: (a) Relative thermal conductivities of supported SA and ZA GNM to the suspended GNM ($k_{\text{sup}}/k_{\text{sus}}$). (b) Relative thermal conductivity of GNM to non-porous graphene ($k_{\text{GNM}}/k_{\text{GNM,np}}$) in suspended and supported SA and ZA GNMs with respect to porosity (ζ).

This enhancement to cross-plane transport within high-porosity GNMs is attributed to an increased strength of interactions between the Si and carbon atoms, stemming from a reduction in interfacial distance between Si and GNM. Carbon atoms in non-porous graphene are constrained by three C-C (sp^2) bonds, while edge atoms are connected with one or two neighboring atoms. As porosity increases, a larger fraction of these atoms are located at hole edges with dangling bonds; in turn, this causes GNM structures to become less rigid and more susceptible to deformation by van der Waals forces. Thus, the average distance between Si and GNM decreases with increasing porosity, and is described by the atomic density distribution in Fig. 3.8c. Since vdW interactions become stronger at shorter distances, this reduction in interfacial distance leads to the expectation of stronger interactions across the interface and thus, lower interfacial resistances [133, 134, 135]. In addition, the increasing size of the near-zero peaks in D_p (Fig. 3.8d), which have a longer wavelength and higher transmission across interface [97, 98], enables for lower interfacial thermal resistance, and evidences the emergence of stronger interactions between Si and GNMs [46].

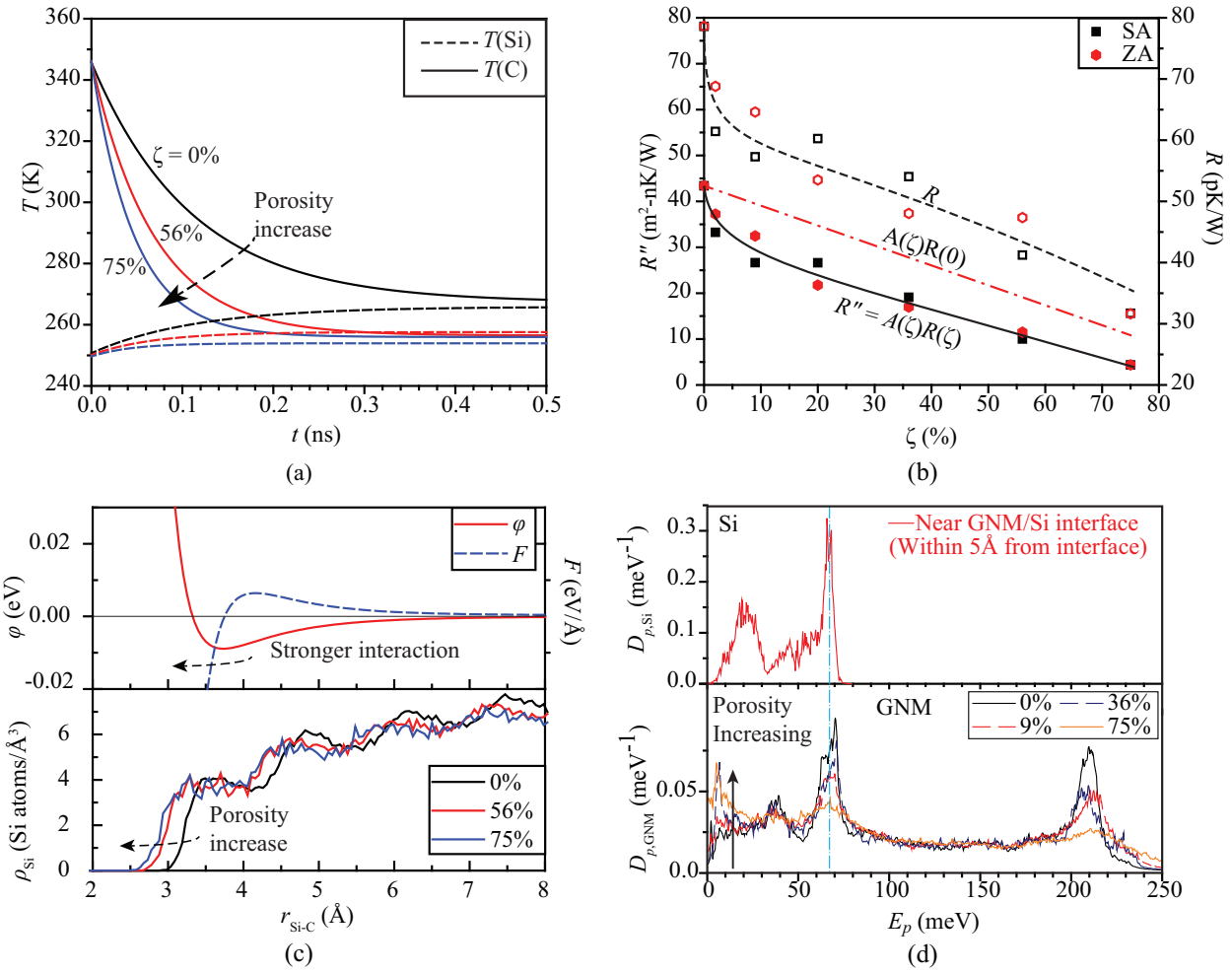


Figure 3.8: (a) Temperature profiles for Si (dashed lines) and GNM (solid lines) during the temperature relaxation period. As porosity increases, the system reaches thermal equilibrium more quickly and at a lower equilibrium temperature. (b) Interfacial thermal resistance, R (outlined shapes and dashed line), and areal interfacial thermal resistance, $R''(\zeta) = A(\zeta)R(\zeta)$ (filled shapes and solid line). To evaluate the effect of decreasing A on decreasing R, $R''(\zeta) = A(\zeta)R(0)$ is also plotted (dashed dot line). (c) Upper panel: Alterations in potential energy (φ) and atomic force (F) of Si and C atoms, based on the used vdW LJ potential model, with respect to atom distance. Lower panel: Atomic density distribution of Si with respect to the distance of C atoms. Porosity increases lead to decreases in the average distance between Si and C, and potential energy and force increases. (d) Upper panel: D_p of Si near the interface with graphene (< 5 Å from the interface). Lower panel: D_p of supported GNM at various porosities.

Since the nanomesh (porous) structure is locally included within our simulated systems, thermal conductivity is spatially distributed and the variation of thermal resistance ($\propto 1/k$) produces a diversion in heat flux to the substrate. Reduction of interfacial thermal resistance, via increase in porosity, enhances this process. Due to heat redirection to the substrate, the heat flux at both thermostated ends (q_T, obtained from recorded thermostat heat exchange data) is larger than that of the central porous region [$q_{f,x}$, calculated from averaged heat flux in the x-axis direction using Eq. (1)]. This heat redirection is shown schematically in Fig. 3.9, demonstrating two possible paths for heat to flow; the first path is without heat leakage to Si and along the GNM, and the second path is heat leakage and reaching the cold thermostat through the Si block. The resistance of the first path is synonymous with thermal resistance of the GNM and can be calculated from its thermal conductivity ($R = l/kA$). When heat flow leaks to the substrate, as in the second path, interfacial thermal resistance (Fig. 3.8b) and thermal resistance of the Si block are included in total resistance of the path. The thermal resistance of the first path displays an increase as porosity increases, while the resistance of the second path is shown to decrease with increasing porosity; thus, a higher porosity leads to a larger mismatch between q_T and $q_{f,x}$ (i.e., larger heat leakage) as Fig. 9 shows.

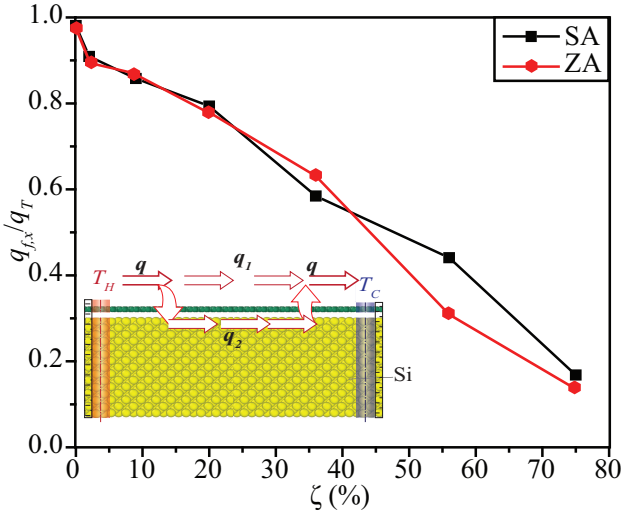


Figure 3.9: Ratio of heat addition/subtraction to/from the thermostated regions (q_T) to the ensemble average of the heat flux x component ($q_{f,x}$) within supported GNM.

3.5 Conclusions

Propagation of thermal energy carriers is redirected by geometrical confinements on graphene (hole arrangement and size); this redirection of heat flow is shown to effectively control thermal transport. The transport channel scale (width) in GNMs is critical to resultant variations of in-plane thermal transport as: 1) nanoscale channel size and hole pitch less than the phonon mean free path induce ballistic transport between holes and promote porosity dependence of conductivity, and 2) smaller channel widths, as found within larger porosities, more significantly confine the direction of thermal carrier propagation (more aligned with channel direction), thus magnifying the effect of hole arrangement (different conductivities of GNMs with ZA and SA). Although additional scatterings caused by the GNM supporting substrate do not change the tendencies of conductivity variation by porosity and arrangement, their influences on in-plane transport are weakened by diversified scattering mechanisms. Contrarily, GNM porosity is shown to greatly affect cross-plane transport as interfacial thermal resistance decreases with increasing porosity. This is in spite of a decreasing area available for thermal transport to take place; as the average atomic distance between the substrate and GNM is reduced due to structure weakening from broken bonds near holes, the strength of vdW interactions increase between the two layers. With increasing porosity of supported GNM, we observe heat leakage to the substrate stemming from decreases of in-plane conductivity and cross-plane thermal resistance; considerations should be given to this diversion of heat flow within conductivity measurements and simulations for improved accuracy. This study presents an effective means to control heat flow direction and magnitude, in addition to accurate prediction of thermal transport results; these findings have possible extension to enhanced thermal system design and evaluation of electronics.

Chapter 4

Thermal Rectification via Asymmetric Structural Defects in Graphene

A version of this chapter was originally published by Ali Yousefzadi Nobakht, Yasser Ashraf Gandomi, Jiaqi Wang, Matthew H Bowman, Drew C Marable, Benton E Garrison, Daekun Kim, and Seungha Shin:

Nobakht Yousefzadi, Ali, et al. "Thermal rectification via asymmetric structural defects in graphene." Carbon 132 (2018): 565-572.

4.1 Abstract

Thermal rectification in defect-engineered graphene with asymmetric hole arrangements is assessed via molecular dynamics simulations. Asymmetry in two different configurations (triangular and rectangular hole arrangements) is controlled by manipulating geometrical parameters, such as hole size; effects of geometry on the resultant rectification are investigated. Filtering of phonon propagation directions by geometrical confinement, and asymmetric relaxation distance induce a difference in heat transfer depending on transport direction, or thermal rectification. Increase in porosity, which results in additional confinement and larger difference in relaxation, produces more significant thermal rectification. While a rectangular arrangement of holes results in 70% of the maximum thermal rectification, up to 78% of rectification was achieved using a triangular arrangement within 47.5 nm of graphene, which can be attributed to more effective phonon-hole boundary scattering with a triangular arrangement. This study suggests a feasible approach to create thermal rectification and enables its fine control, contributing to the development of phononic devices and enhancement of thermal system design for electronics.

4.2 Introduction

Thermal transport control has been a key topic of study for thermal engineering in electronic and energy conversion devices so to achieve desirable thermal conditions for both operation and efficiency [136]. Recent focus has been on advanced control of thermal transport for a more complicated requirement of achieving high thermal transport in one direction while insulating in the other along that same path of transport [137, 138, 139, 140]. Control of the thermal transport directionality enables for greater thermal management of systems, as protection from external heat can be provided in addition to the management of systematic heat generation. This, termed 'rectification,' is allowed by the asymmetric thermal properties, as asymmetric configurations create different thermal resistances [141, 142, 143]. These systems, deemed thermal rectifiers, are expected to serve as a critical building block for advanced phononic devices [144, 145, 146, 147].

Asymmetric configurations for rectification in solids can be achieved in single- and multi-component systems. In heterostructures, discrepancies in thermophysical properties (thermal strain, thermal potential barriers, etc.) of two materials can effectively create different interfacial thermal transport depending on the directionality of heat flow [7]; however, additional structural complexity and influence on other properties have led to the study of thermal rectification using homogeneous structures [142]. Geometrical confinement [138, 141, 142, 144, 145, 146, 147] and/or nonlinear interactions within the system [148, 149, 150, 151, 152, 139, 143] have been suggested as primary mechanisms for inducing thermal rectification phenomenon within these single-material designs. Low-dimensional carbon materials, such as graphene and carbon nanotube (CNT), have been employed for thermal rectification studies [138, 141, 145, 47] due to their facile geometric confinement and extremely high thermal conductivity (2000 - 5000 W/m-K near room temperature) [18, 37, 130, 153], holding promise for manipulation of thermal transport characteristics. Low phonon-phonon (p-p) scattering rate in graphene allows for geometric confinement or defects to have a significant influence on thermal transport control [35, 36]. Recent studies have debated over the use of either carbon nanotubes [154, 7, 140] or graphene nanoribbons (GNR) [138, 155, 145] as optimal thermal rectifiers. Transport studies within

asymmetric GNR's revealed that the heat flux flows greater in the direction of decreasing width than the opposite direction [142]. As the length of the GNR is reduced, the resultant thermal rectification was found to increase [152]. Through several studies, it has been found that defects [106, 156, 157, 158, 159], functional groups [108, 160, 161, 45], and vacancies [47, 162, 111] produce different effects on the outward display of graphene properties in terms of thermal and electronic transport. A majority of previous research studies pertaining to graphene and CNT thermal rectification are experimentally expensive or challenging to implement [163, 146, 164], impractical [140, 165], or requiring significant changes in device shape and design [138, 144]. In contrast, since the size and position of holes within the material can effectively be controlled by the focused ion beam (FIB) method in experiments [116, 122, 136], precise control of thermal rectification can now be achieved.

As a new feasible method for thermal rectification control, the thermal transport behaviors in defect-engineered graphene (DEG) with asymmetric hole arrangements is evaluated for thermal rectification. In this research, heat transfer and phonon behaviors with two different directions of heat flow are calculated and compared via analysis of molecular dynamics (MD) simulation results. Hole size (or porosity) and hole arrangement (triangular and rectangular) are controlled, and the effects of asymmetric geometries and porosity on the transport of thermal energy carriers are discussed.

4.3 Material and Methods

Periodic boundary conditions are applied in the y-axis direction, while fixed and free boundary conditions are employed for the x- and z-axis directions, respectively. Here, x and y are the in-plane directions, and heat flows in the x direction (Figs. 4.1a and 4.1b). A single-layer graphene sheet is simulated, and for all tested simulations, the dimensions of the sample graphene are held constant (i.e., length in x direction, $l = 47.5$ nm; width in y direction, $w = 23.5$ nm). The adaptive intermolecular reactive empirical bond order (AIREBO) [66] potential is used to model inter-carbon (C-C) interactions. All simulations were performed using Large-scale Atomic/Molecular Massively Parallel Simulator (LAMMPS) [65]; the total simulation time and time step size for all simulations are 2.5 ns and 0.5 fs, respectively. The

results presented in this work have been obtained via averaging five independent simulations and all common verification of MD resultant data (e.g., validation of potential and kinetic energy convergence, and structural stability) were performed for all of the simulations to ensure that presented results are physically sound and scientifically meaningful.

Asymmetric structures, employed for the analysis of thermal rectification (or asymmetric thermal transport) are created by introducing holes to a single-layer graphene sheet. The holes are oriented in two different arrangements of holes [triangular arrangement (TRA) and rectangular arrangement (REA)] (Figs. 4.1a and 4.1b). In each simulation, hole sizes are uniform and the porosity (ζ) ranges from 0 to 75% for the hole-filled area, while the center positions of holes are fixed. In the TRA simulations, the hole size is altered to reach the desired porosity. In the REA, the distance between hole-filled area (d_s) is considered in addition to hole size. With two different values of d_s (= 0 and 5 nm), porosity is controlled by adjusting hole size with fixed hole positions. In an additional series of simulations, the effect of d_s on thermal rectification is investigated by varying d_s from 0 to 10 nm for two selected porosity values (30% and 60%). Degree of asymmetry (or asymmetricity, α_A), as a parameter related to both porosity and hole distribution (Fig. 4.1c), is evaluated by using the first moment of area [$\int(x - x_c)dA$, where x is the x coordinate (parallel or opposite to the heat flow direction), dA is the integration element, and x_c is the x coordinate of the centerline in a pristine graphene], given as:

$$\alpha_A = \frac{|\int(x - x_c)dA|}{\int|(x - x_c)dA|.} \tag{4.1}$$

Here, α_A can range from 0 to 1; for samples without hole or with symmetric hole arrangement, $\alpha_A = 0$, while perfect asymmetry results in $\alpha_A = 1$.

Temperature distribution and thermal transport are induced under non-equilibrium temperature settings [75, 76] by prescribing hot and cold thermostatting regions at the two opposite ends of the simulation sample. To examine thermal transport at T, temperatures of hot and cold thermostats are set as $T + 25$ K and $T - 25$ K, respectively. Initial equilibration is performed for 0.5 ns in the NVT ensemble (constant number of particles, volume, and temperature) by rescaling velocities to a prescribed temperature.

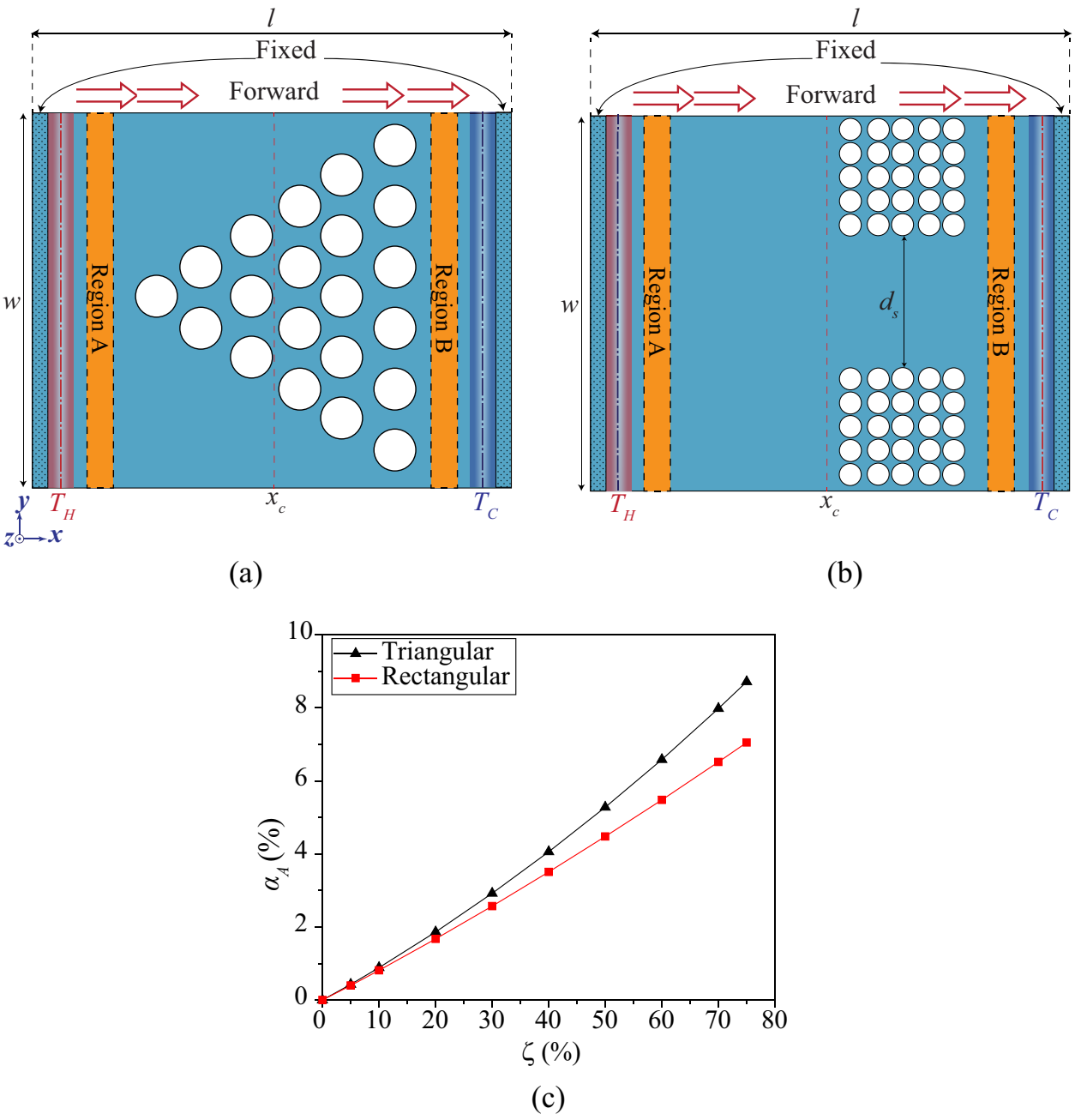


Figure 4.1: Schematics of simulation cells for (a) triangular hole arrangement (TRA), and (b) rectangular hole arrangement (REA). In both cases, the heat flow direction from low to high porosity region is defined as the forward direction, and the opposite direction is reverse direction. In this figure, the white circles represent the holes distributed in DEG. (c) The relation between the porosity (ζ) and the degree of asymmetry (α_A). Here, d_s=0 for the rectangular case.

After equilibration is completed, five layers of carbon atoms (≈ 4.6Å) are fixed at both ends of the structure (x- and y-axis directions) to prevent heat leakage to the periodic mirror of sample at the ends; hot and cold Langevin thermostats are then applied next to these fixed regions to generate a heat flux within the simulation sample [42, 112, 76]. The chosen forward and reverse directions are shown in Fig. 4.1, and the thermal rectification (η) is calculated as:

$$\eta(\%) = \frac{|q_{\text{forward}} - q_{\text{reverse}}|}{q_{\text{forward}}} \times 100, \tag{4.2}$$

where q_{forward} and q_{reverse} (W/m^2) are heat fluxes between two thermostats when heat flows in the forward and reverse directions. Heat flux is calculated using the average heat added to/removed from the thermostats per unit cross-sectional area over a time span of 2.0 ns; for the cross-sectional area, the thickness of single-layer graphene is selected as the inter-layer spacing of graphite (0.335 nm [79]).

To examine local heat flow direction and magnitude, we divide the simulated DEG into smaller cells via a mesh grid. For selection of appropriate mesh size, we tested different grid dimensions and calculated the temperatures of hole edge cells with the smallest number of atoms (T_{cell}), which have the potential to display the largest deviations from a prescribed, overall temperature (T_{o}). The difference between selected cell and overall equilibrium temperature of a sample ($T_{\text{cell}} - T_{\text{o}}$) decreases as the mesh size and number of atoms in the cell increases; ultimately, this difference reaches almost zero when the cells contain a sufficient number of atoms for thermal analysis. Here, 50×50 mesh grid is selected as it allows for the statistically meaningful heat flux calculations to capture all geometrical and heat flow details. The local heat flux vector is calculated by [166, 167]:

$$\boldsymbol{q} = \frac{1}{V}[\sum_i \frac{1}{2} m_i(\boldsymbol{u}_i \cdot \boldsymbol{u}_i)\boldsymbol{u}_i + \sum_i \varphi_i \boldsymbol{u}_{i,x} + \frac{1}{2}\sum_i \sum_j \boldsymbol{x}_{ij}(\boldsymbol{u}_i \cdot \boldsymbol{F}_{ij})], \tag{4.3}$$

where V is the volume of the simulation domain, m_i is the mass, $\boldsymbol{u}_i$ is the velocity vector, φ_i is the potential energy of particle i, and $\boldsymbol{x}_{ij}$ and $\boldsymbol{F}_{ij}$ are the relative position vector and interaction force between i and j particles. Here "i" and "j" are indices of particles in the domain.

To identify phonon behaviors within thermal transport, phonon density of states (D_p) is calculated through the Fourier transform of the velocity autocorrelation function [86, 46] in two different regions, before and after the hole-filled area (Regions A and B in Fig. 4.1). Due to an asymmetric geometry, the D_p will be different for these regions [145, 146]. The overlap factor (S), which can provide a quantitative indirect measure of phonon transmission spectra [168] and characterize the rectification properties [150, 151, 152, 139], is defined as:

$$S = \frac{\int_0^\infty D_{p,A}(\omega) D_{p,B}(\omega) d\omega}{\int_0^\infty D_{p,A}(\omega) d\omega \int_0^\infty D_{p,B}(\omega) d\omega}, \tag{4.4}$$

where $D_{p,A}$ and $D_{p,B}$ are phonon density of states calculated for the regions A and B, respectively.

4.4 Results and Discussion

As nanoscale structural defects, or holes, are introduced to a single-layer graphene sheet, thermal transport decreases due to additional phonon scatterings by hole boundaries. Since the positions of hole centers are fixed and asymmetrically distributed, porosity (ζ) and asymmetricity (α_A) increase as hole size increases. Differing from cases with symmetric hole arrangements [47], reduction in thermal transport of asymmetric configuration depends on heat flow direction; i.e., when heat flows in the reverse direction (from high to low porosity area), as the porosity increases, thermal transport decreases more significantly than the forward direction (Fig. 4.2a). The difference between heat fluxes with two opposite directions demonstrates heat flow rectification, which is characterized as η. As Fig. 4.2b shows, η increases with ζ and α_A; specifically, with $\zeta > 30\%$, rectification is more noticeable. According to the local heat flux analysis, the heat flow downstream area has a larger density of small magnitude heat flux vectors, when compared with that of the upstream region, in both forward and reverse heat flow cases (Figs. 4.3a and 4.3d).

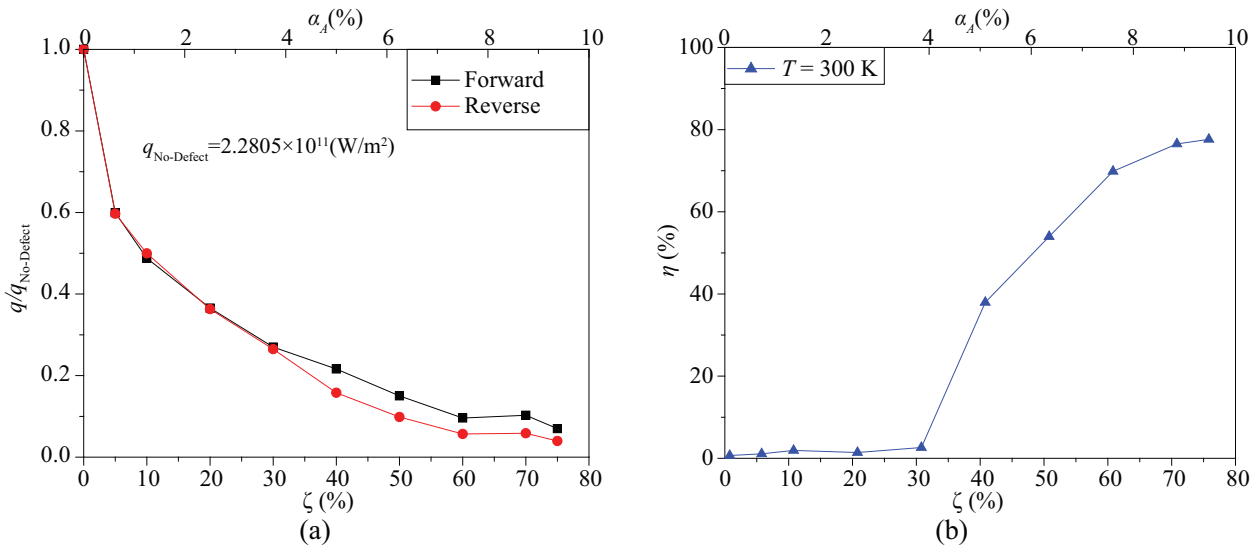


Figure 4.2: Heat flux ratio of DEG with triangular hole arrangement to non-defect graphene with respect to porosity (ζ) and asymmetricity (α_A). (b) Thermal rectification of DEG with triangular hole arrangement with respect to porosity (ζ) and asymmetricity (α_A).

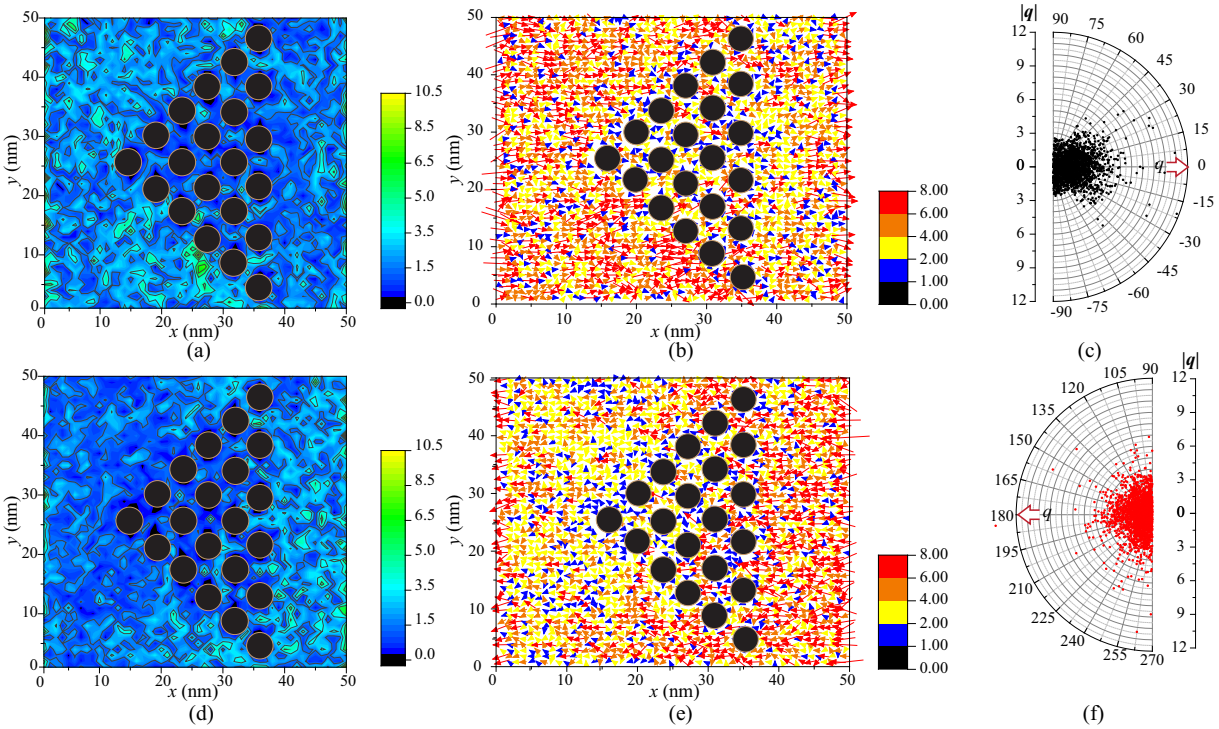


Figure 4.3: Local heat flux distribution in DEG with a triangular hole arrangement. For the forward direction of heat flow, (a) local heat flux contour, (b) local heat flux vectors, and (c) angular distributions of local heat flux vectors. For the reverse direction of heat flow, (d) local heat flux contour, (e) local heat flux vectors, and (f) angular distributions of local heat flux vectors.

Since the simulated systems in this study are under steady-state condition and contain no heat source or sink between hot and cold thermostats, the heat flow of cross-sectional area at any point (x) must be consistent along the flow direction due to energy conservation. To maintain a constant amount of heat flow with a smaller magnitude of local heat flux vectors, the vectors should be more oriented in the heat flow direction, rather than randomly distributed. Figures 4.3b and 4.3e confirm that heat flux vectors downstream have more directionality in the heat flow direction. Since the direction of local heat flux vector can be considered as the average phonon propagation direction, we attribute this to the fact that phonon transport channel is laterally confined by hole structures. Thus, phonons, whose propagating direction has a small angle from the overal heat flow direction $\pm x$, can pass through the channel between holes, while phonons with a propagation direction more deviated from the heat flow direction, are back-scattered by hole boundaries. These oriented vectors are equilibrated to have a broader angular distribution by phonon-phonon (p-p) scattering downstream (momentum relaxation). However, as the phonon mean free path in graphene is longer than the simulation system size, it cannot be fully relaxed and the degree of relaxation depends on distance after the hole area. Since the reverse direction allows for a longer average distance after holes, further momentum relaxation, and thus, less oriented heat flux vectors are expected than the forward heat flow case. As predicted, comparing angular distribution of heat flux vectors (Figs. 4.3c and 4.3f), a large portion of heat flux vectors are between -45° and 45° in the forward direction, while heat flux vectors have a more random angle distribution in the reverse direction due to more relaxation. With more oriented phonon propagations, heat transfer can be more efficient in the forward direction, resulting in thermal rectification.

In MD simulations of defected graphene structures, phonons are scattered by hole boundaries, other phonons, and thermostats (due to a limited distance between the two thermostats). Nanoscale hole pitch shorter than mean free path by p-p scatterings ($\sim$240-750 nm [19, 90]) leads to the dominance of phonon-hole boundary (p-hb) scattering, especially for large-porosity (ζ) cases.

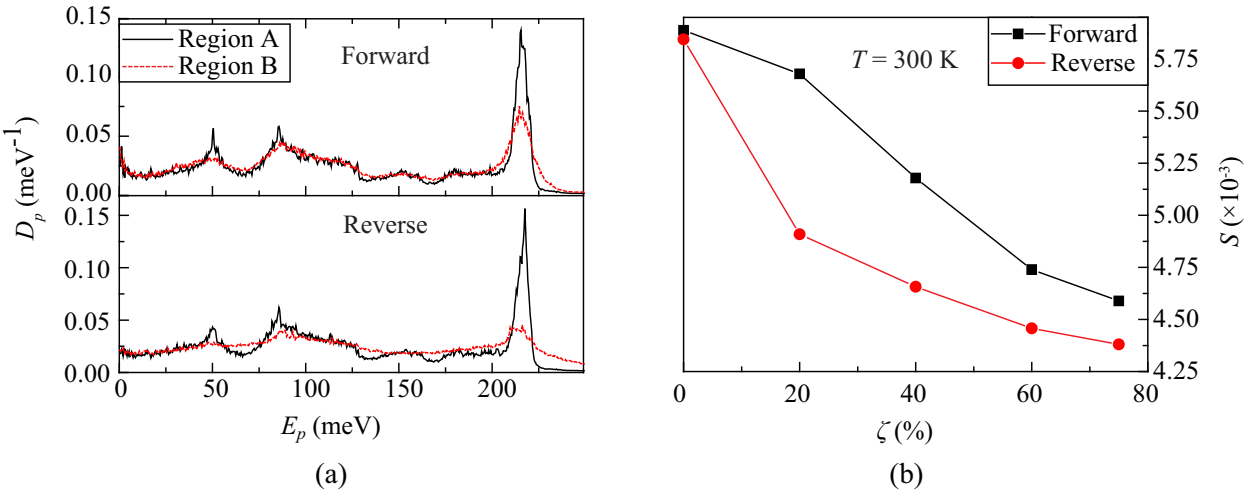


Figure 4.4: (a) Phonon density of states (D_p) of TRA-DEG at Regions A and B in the forward and reverse heat flow directions. (b) Effect of porosity on D_p overlap factor (S) of TRA-DEG, for the forward and reverse heat flow directions.

Depending on heat flow direction, different T's are prescribed in regions A and B, which can result in different thermal transport efficiencies. Figure 4.4a shows different phonon density of states (D_p) depending on heat flow direction and Fig.4.4b demonstrates overlap of D_p's in two regions (S) varying with porosity. As the forward direction has a larger S than the reverse, more phonons can be transported without changing their energy, also reinforcing preferred heat flow in the forward direction.

Regardless of heat flow direction, reduction in magnitude of local heat flux vectors is also observed after the hole area with a rectangular arrangement (REA), as in TRA case (Figs. 4.5a and 4.5d). Forward-direction heat flow in Fig. 4.5b demonstrates a larger area of high-magnitude (red) vectors and smaller area of low-magnitude (yellow and blue) after the hole filled region, as compared to the reverse-direction heat flow in Fig. 4.5e. Similar to TRA, this asymmetry allows for a different relaxation distance after lateral confinement; this contrast of relaxation extent, which is supported by different angular distributions of heat flow vectors in Figs. 4.5c and 4.5f, causes thermal rectification.

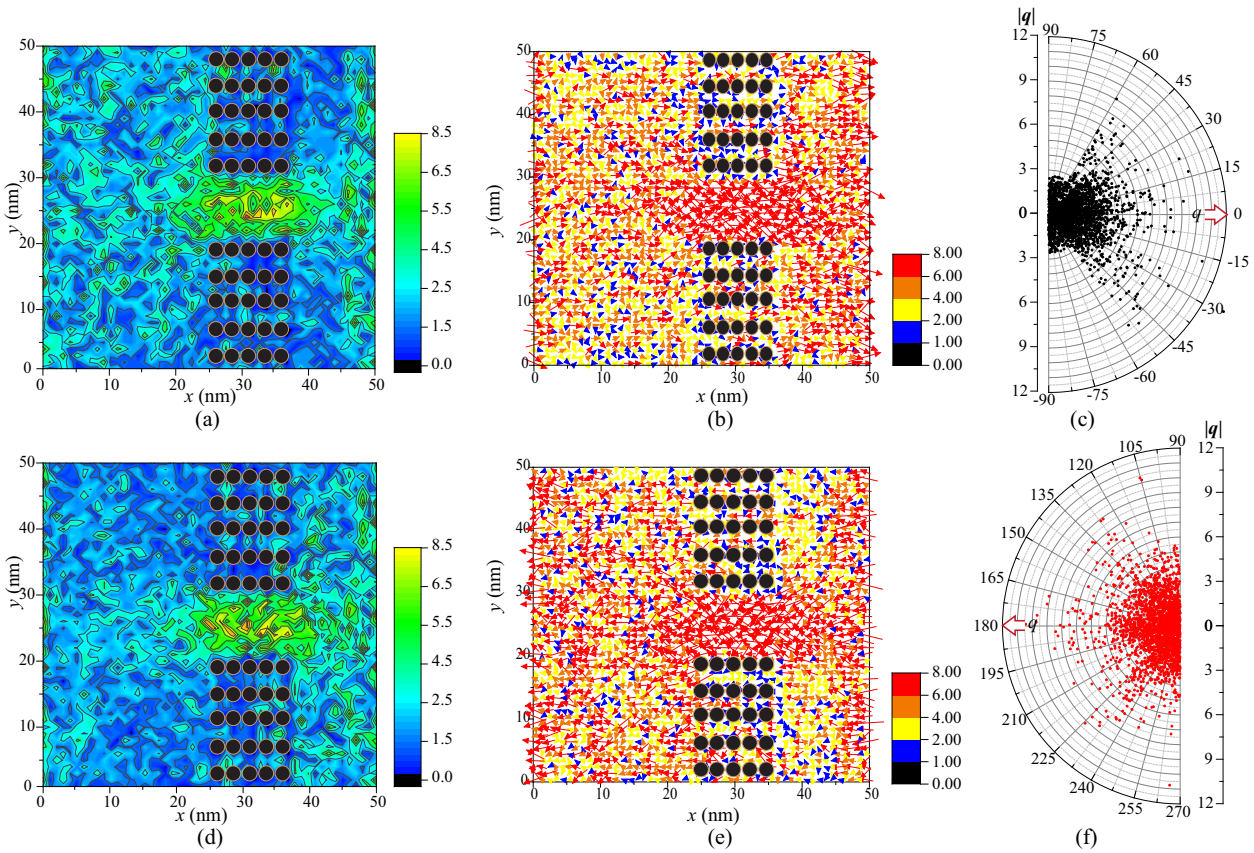


Figure 4.5: Local heat flux distribution in DEG with a rectangular hole arrangement. For the forward direction of heat flow, (a) local heat flux contour, (b) local heat flux vectors, and (c) angular distributions of local heat flux vectors. For the reverse direction of heat flow, (d) local heat flux contour, (e) local heat flux vectors, and (f) angular distributions of local heat flux vectors.

When non-defected area exists ($d_s > 0$), heat flow is concentrated on a non-defected channel, but less lateral confinement enables a larger angular direction distribution of local heat flux vectors than holey area as in Figs. 4.5b and 4.5e. Thus, the difference between heat flux distributions in forward and reverse directions is reduced as d_s increases, decreasing the dependence of heat flow direction.

As Fig. 4.6a shows, while maintaining positive dependence on porosity, rectification of REA shows a more significant increase when the non-defected area is smaller. Conversely, with a larger porosity (ζ) of holey area or larger hole size (d), η decreases faster as d_s increases. Figure 4.6b shows that η reduction by increasing d_s with $\zeta = 30\%$ is smaller than the case of $\zeta = 60\%$, especially near $d_s = 0$, demonstrating that the relative size of a non-defected channel [$= d_s/(l_p - d)$, where l_p is the hole pitch] is an important factor in rectification. To compare rectification of different hole arrangements, η's are plotted with respect to its

degree of asymmetry (α_A) as in Fig. 4.6c. Structural asymmetricity and phonon propagation redirection cause the contrast in relaxation process after defected structures, which induce rectification in nanoscale systems, where transport is not fully diffusive. As the asymmetry and phonon redirection are controlled by hole arrangement and size, the graphene structure can be optimized for large rectification. While this research presents different optimal hole arrangements for a large rectification depending on α_A, overall TRA displays the largest rectification (especially when $\alpha_A > 4\%$).

Here, we note that the reported rectification depends on system size and temperature setting, which can influence the discrepancy of phonon relaxation between the heat flow up- and downstream regions. The rectification is expected to decrease with increasing size, which is supported by our additional simulations on a different length [10 nm increase in non-defected region (where relaxation occurs) caused 4.3% drop in thermal rectification for the TRA-DEG]. If the system domain is large enough for phonons to be fully relaxed, the rectification could diminish. This implies that more rectification can be observed when an asymmetric hole distribution is created within a region smaller than the phonon relaxation length, such as a small grain in a polycrystalline graphene. In addition, a higher temperature will shorten the relaxation distance, while a larger temperature gradient will increase asymmetricity of phonon relaxation; thus, the degree of rectification can change with working temperature and prescribed temperature gradient (lower temperature and larger gradient would be desirable). The detailed effects of system size and temperature can be further studied in future works.

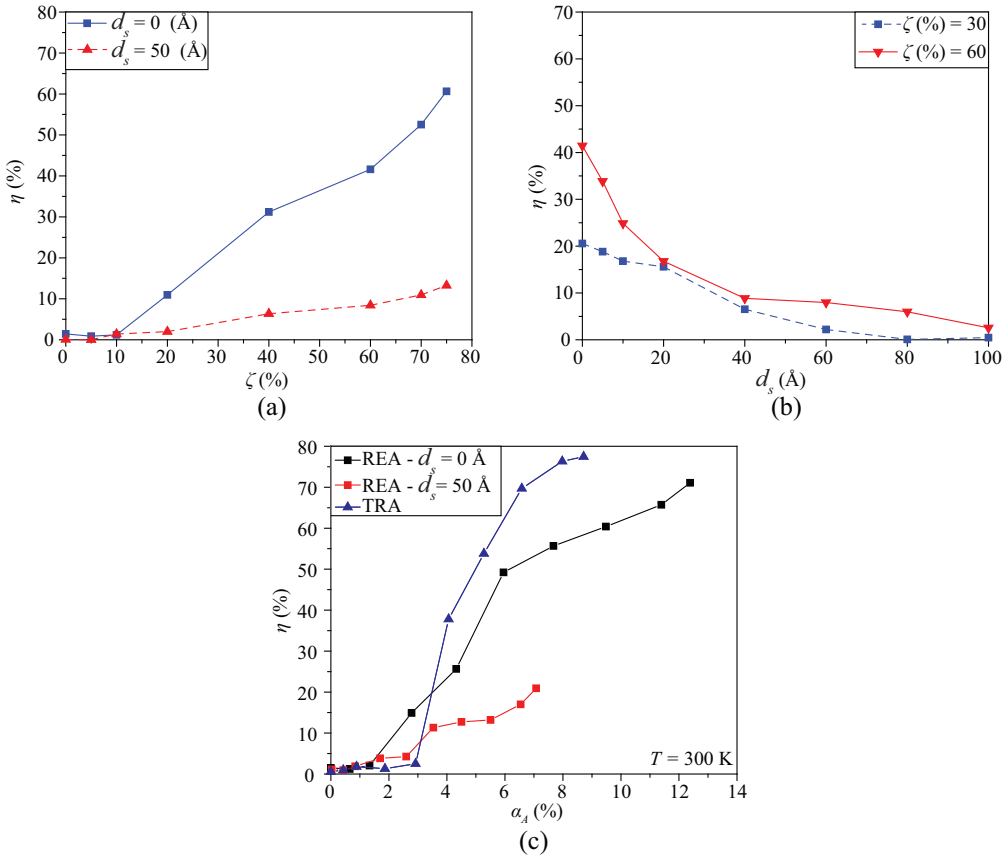


Figure 4.6: Thermal rectification of REA-DEG (a) with respect to porosity with different non-defected areas (d_s = 0 and 5 nm). (b) With two different porosities, rectification variations with respect to non-defected area size (d_s). (c) Comparison of thermal rectifications for TRA and REA with two different non-defected area sizes

4.5 Conclusions

The effects of asymmetric hole arrangements on directional dependence of thermal transport were investigated within a single layer of graphene. Geometrical confinement by hole structures leads to selective phonon transport depending on propagation direction, reducing thermal conductance. The resulting distribution of phonon propagation direction is equilibrated through momentum relaxation after lateral phonon confinement. With an asymmetric structure and nanoscale dimension in ballistic regime, the extent of relaxation depends on the heat flow direction, and this contrast yields to thermal rectification within the asymmetric defect engineered graphene samples; i.e., with an equivalent temperature difference, heat flow is larger with an increasing-porosity (forward) direction. Thermal

rectification increases as porosity increases, and can reach as high as 78% at room temperature with triangular hole arrangement with porosity of 75%. The difference in the overlap of D_p's in two regions (S) are different for the forward and reverse direction and S decreases as temperature and asymmetricity increases.

The proposed method of inducing thermal rectification within graphene sheets is both experimentally and economically feasible. In contrast to previous thermal rectification studies, which require complex geometries or impractical graphene sheet tailoring, our results demonstrate that thermal rectification can be achieved by creating asymmetric hole arrangements, without altering the overall rectangular shape of the device. By controlling the hole size and position, we can manipulate the thermal rectification value, thus enabling effective and precise thermal rectification for advanced thermal management and phononic device.

Chapter 5

Control of In-plane and Cross-plane Thermal Transport of Graphene by Silicon Doping

5.1 Abstract

Effects of silicon (Si) doping on thermal transport of suspended and SiO_2-supported graphene are investigated via molecular dynamics (MD) simulations. Due to the large mismatch in atomic mass, Si can be an effective depressor for thermal transport, while minimizing the reduction of electron transport due to the resemblance in valence electrons between the host carbon (C) and doped Si. The change of transport in Si-doped graphene is attributed to phonon-impurity scattering, induced by the mass and interaction mismatches between C and Si. This study identifies contribution of mass mismatch as well as interaction mismatch of Si to transport reduction, separately. In addition, these mass and interaction mismatch effects are also examined on in-plane thermal conductivity and cross-plane thermal resistance of SiO_2-supported graphene by systematic control of MD simulation conditions. 2% Si doping reduces in-plane transport of suspended graphene by ∼80% with more contribution of interaction mismatch. Support graphene with 2% of Si doping is less affected by doping (70% of reduction), and rather cross-plane transport is enhanced, showing the decrease of interfacial thermal resistance by ∼30%. Change in phonon behavior due to doping creates near zero energy peaks in phonon density of states which enhances the interfacial thermal transport to the substrate. This study improves the understanding of dopant concentration effect on in-plane and cross-plane thermal transport in graphene/SiO_2 heterostructures and provides insights to control thermal transport for enhanced thermal design.

5.2 Introduction

Exceptional properties of graphene, including its high electrical and thermal conductivities [169, 170, 171, 37, 54, 172], have motivated extensive research on graphene over the last decade. In particular, tailoring of graphene properties has been of great interest for the development of various innovative and enhanced applications, such as electronic and photonic devices [173]. Although the high thermal conductivity of graphene offers the promise of effective heat dissipation, it is not always desirable depending on application (e.g., thermoelectric energy conversion [29, 30, 31, 32]) and its control also influences (mostly deteriorates) other properties; thus, advanced control of thermal transport in graphene has been actively studied. Edge passivation [112], strain [113], grain boundary [109, 114], geometrical defects [47], point defects [164, 174], isotope engineering [175, 45, 176, 177], and substitutional dopants to graphene [174, 178, 179, 175] have been suggested to alter the graphene thermal transport, and all these approaches displayed their effectiveness in thermal transport control. For applicational enhancement, the influence on other structural and electrical properties should be minimized, and thus, substitutional atomic doping, which can allow for suppressing thermal transport without destruction of hexagonal lattice structure inducing significant property changes, attracts more interest as one of the most effective and promising methods [179, 175]. For thermal transport control by doping, researchers have used different materials as dopants, like aluminum (Al), phosphorous (P), sulfur (S), hydrogen (H), nitrogen (N), boron (B), and silicon (Si) [180, 181, 182, 183, 184].

Lowering thermal conductivity, while maintaining the electrical transport, can lead to an efficient thermoelectric conversion [29, 30, 31, 32], and this can be achieved by enhancing the phonon scattering and minimizing the change of electronic structure. Since Si is in the same periodic family as host carbon atom (C), Si doping is possibly more effective to maintain electronic structure, thus electrical conductivity, than other dopants. Moreover, a large mismatch in atomic mass between Si and C is expected to increase a scattering rate, reducing thermal conductivity, according to the perturbational analysis [185]. Therefore, Si doping is promising to thermoelectric applications, and this possibility is supported by recent studies on electrical and thermal transport of Si doped atoms [186] showing a

notably lowered thermal conductivity and a considerable charge mobility. Even though previous studies [176, 177] focused on the mass mismatch, doping distorts the force field around dopants, and this bonding strength mismatch can also contribute to additional phonon-impurity scattering. Also, doping effects on cross-plane (interfacial) and in-plane thermal transport of supported systems have been relatively unexplored. Thus, further study of the scattering origins and comprehensive evaluation of doping effects can improve the understanding of thermal transport control by doping. In this research, in-plane and cross-plane thermal transport of Si-doped graphene are investigated using the molecular dynamics (MD) simulations. Silicon dioxide (SiO_2) is employed as a substrate materials as widely used in applications [187], and the doping concentration is considered up to 2%. By adjusting mass and interatomic potentials of dopants, contributions of mass and bonding strength mismatches to thermal transport control are evaluated separately, and phonon spectrum is also calculated to explain thermal transport behaviors of Si-doped graphene.

5.3 Materials and Methods

Boundary conditions in the y-axis direction are periodic, while it is fixed and free for the x- and z-axis directions, respectively. As shown in Fig. 5.1a, x, and y are the in-plane directions, and heat flows in the x-direction. One layer of the graphene sheet is simulated, and for all of the simulations in this study, the length in the x-direction is $l = 50.0$ nm and width in the y-direction is $w = 20.0$ nm, and for the supported cases, Fig. 5.1b the height of SiO_2 block in the z-direction is $h = 32.82$ nm. The adaptive intermolecular reactive empirical bond order (AIREBO) [66] potential is used to model inter-carbon (C-C) interactions, Tersoff potential applied to model C-Si [188], Si-Si, O-O and O-Si [189] interactions. The interaction between the graphene and SiO_2 substrate is assumed to be van der Waals (vdW) type, which is modeled using the Lennard-Jones (LJ) potential [190] $V_{ij}(r) = 4\epsilon_{ij}[(\sigma_{ij}/r)^{12} - (\sigma_{ij}/r)^6]$, where i = C, j = Si or O, and r is the interatomic distance. The numerical values of the ϵ_{ij} and σ_{ij} obtained from Ong et al. [85]. All simulations were performed using Large-scale Atomic/Molecular Massively Parallel Simulator (LAMMPS) [65]. Time step size and total simulation time and for all simulations are 0.5 fs and 2.5 ns, respectively. The results

presented in this work have been obtained via averaging five independent simulations, and all common verification of MD resultant data (e.g., validation of potential and kinetic energy convergence, and structural stability) were performed for all of the simulations to ensure that presented results are physically sound and scientifically meaningful.

Doping is implemented by randomly replacing carbon atoms with Si atoms in graphene sheet while keeping the number of Si atoms in a way to meet the goal dopant concentration. The dopant concentration varies from 0.0% to 2.0% with an increment of 0.2% for all of the simulations.

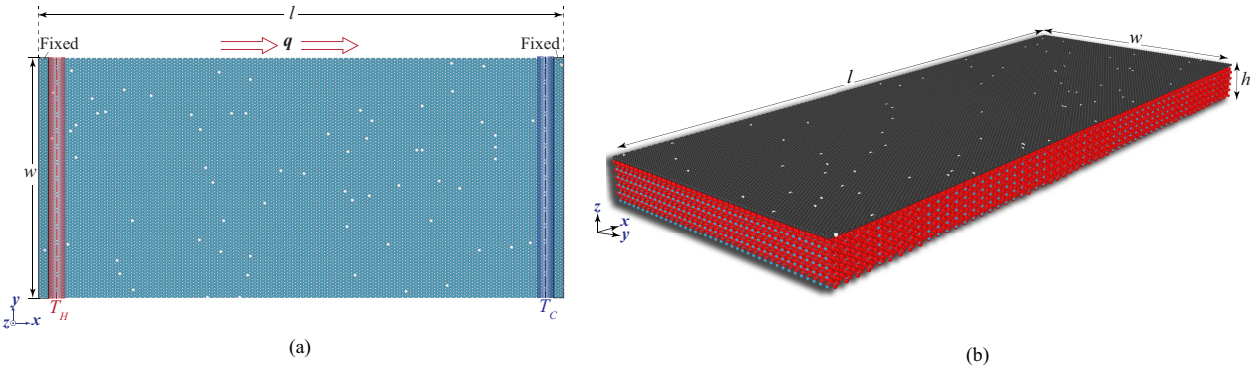


Figure 5.1: Schematics of simulation cells for (a) suspended Si-doped graphene (b) SiO_2 supported Si-doped graphene.

Since Si doping affects phonon transport through scattering by heavier Si atoms and weaker C-Si interactions in comparison to C-C interactions, three cases of Si-doped graphene are simulated for different concentrations (0 to 2%) and geometries (suspended and supported):

i) The mass of C atoms at dopant sites is replaced with the mass of Si atoms, not applying C-Si interatomic interactions (mass effect).

ii) Interactions with C atoms at the dopant sites are replaced with the interactions with Si (C-Si in in-plane, Si-Si and Si-O interactions in cross-plane), not changing their mass (interaction effect).

iii) Both mass and interaction are altered by doping; i.e., the mass of Si and C-Si in in-plane and Si-Si and Si-O interactions in cross-plane are employed (mass+interaction effect).

These allow us to quantify the contributions of mass and interaction mismatches to thermal transport.

Mentioned scenarios help us to distinguish the effect of the interactions and mass of atoms on phonon scattering and thermal conductivity.

Temperature distribution and thermal transport are induced under non-equilibrium temperature settings [75, 76] by prescribing hot and cold thermostatting regions at the two opposite ends of the simulation sample. To examine thermal transport at T, temperatures of hot and cold thermostats are set as $T + 25$ K and $T - 25$ K, respectively. Initial equilibration is performed for 0.5 ns in the NVT ensemble (constant number of particles, volume, and temperature) by re-scaling velocities to a prescribed temperature. After equilibration is completed, five layers of carbon atoms (≈ 4.6Å) are fixed at both ends of the structure (x- and y-axis directions) to prevent heat leakage to the periodic mirror of the sample at the ends; hot and cold Langevin thermostats are then applied next to these fixed regions to generate a heat flux within the simulation sample [42, 112, 76].

Cross-plane thermal transport across the graphene/SiO_2 interface is investigated employing the temperature relaxation method [64, 81]. The graphene/SiO_2 system is first equilibrated at 300 K; hot and cold thermostats at 350 K and 250 K are then respectively placed on the graphene and SiO_2 block in the NVE ensemble. After reaching steady-state, the thermostats are then removed to allow for thermal relaxation of the simulated structure. During this thermal relaxation period, temperature and energy changes of graphene and SiO_2 block are recorded; the interfacial thermal resistance, R (m^2-K/W) can be obtained by [64, 83, 84]

$$R = \frac{\int_0^t A(T_{\text{graphene}} - T_{\text{SiO2}})dt}{E_t - E_0}, \tag{5.1}$$

where E_t is the total energy of the supported graphene, E_0 is the initial energy of graphene at the beginning of relaxation period, A is the thermal transport interface area, and T_{graphene} and T_{SiO2} are the graphene and SiO_2 temperatures.

To identify phonon behaviors within thermal transport, phonon density of states (D_p) is calculated through the Fourier transform of the velocity autocorrelation function [86, 46].

5.4 Results and Discussion

Graphene thermal conductivity can be defined as $k = (1/2)C\nu\Lambda$ based on kinetic transport theory [44]. Here, C is the specific heat, ν is phonon group velocity, and Λ is phonon mean free path (MFP) [45]. If we assume that Λ is limited by the anharmonic phonon Umklapp and point-defect scattering, we can write $\Lambda^{-1} = \Lambda_U^{-1} + \Lambda_P^{-1}$. Subscript U is for Umklapp-limited MFP in $\Lambda = \nu\tau_U$ and subscript P is for point-defect-limited MFP in $\Lambda = \nu\tau_P$. In these equations the τ_U and τ_P are Umklapp-limited phonon lifetime and point-defect-limited phonon lifetime respectively which can be affected by isotopes, defects, impurities or vacancies.

The scattering rate on point defects, $1/\tau_P$, is related to volume per atom in the lattice V_0, phonon frequency ω, and strength of phonon-point defect scattering Γ, $1/\tau_P \propto V_0(\omega^\alpha/\nu^\beta)\Gamma$ [191, 192, 185]; Here, α =3(4) and β =2(3) for a 2D(3D) system, respectively [45]. From perturbation theory Γ is defined as [191, 192, 185]:

$$\Gamma = \sum_i f_i \lfloor (1 - M_i/\bar{M})^2 + \varepsilon\gamma^2(1 - R_i/\bar{R})^2 \rfloor \tag{5.2}$$

where f_i is the fractional concentration of the foreign atoms (e.g., impurity, defect or isotope atoms), M_i is the mass of the i-th substitutional atom, $\bar{M}$ is the average atomic mass, R_i is the Pauling ionic radius of the i-th foreign atom, $\bar{R}$ is the average radius, γ is the Gruneisen parameter, which characterizes the anharmonicity of the lattice, and ε is a phenomenological parameter. The mass of a foreign atom (impurity, vacancy, defect or isotope) is known well whereas the local displacement $\Delta R = \bar{R} - R_i$ due to the atom radius or bond length difference is usually not known.

Considering equation 5.2 and the way τ_p affects thermal conductivity, it is clear that the Si dopant can hinder thermal conductivity by introducing the local mass-difference term, $\Delta M = \bar{M} - M_i$ and bond-strength-difference which can quantify by bond-length difference term $\Delta R = \bar{R} - R_i$ (i.e., weaker bond will result in larger bond length).

Here, the effect of mass is similar to isotopically modified graphene which creates additional phonon scattering called "mass-difference" scattering [45] which is affecting the mass-difference term, and the potential effect is affecting bond-strength-difference term.

5.4.1 Suspended graphene

Fig. 5.2a demonstrates the effect of changing mass, potential as well as mass and potential at the same time. Due to heavier mass of Si atoms (28.085) in comparison with carbon atoms (12.001), the Si atoms act as obstacles for phonon transfer in Si-doped graphene and according to equation 5.2, increment of the substitutional atoms concentration, increases the phonon-point scattering strength (Γ) and phonon scattering rate ($1/\tau_p$) which reduces in-plane thermal conductivity and thermal transport rate ($\mathbf{q}$) more than 80%.

Relative contribution of bond-strength mismatch to thermal conductivity reduction is larger than that of mass mismatch, and their summation is larger than the unity as in Fig. 5.2b shows. This indicates that Si doping induces not only large mass mismatch but also significant bonding-strength mismatch. This results in a very high chance of scattering at dopant sites, thus thermal transport reduction dominantly dependent on fractional concentration of Si dopants.

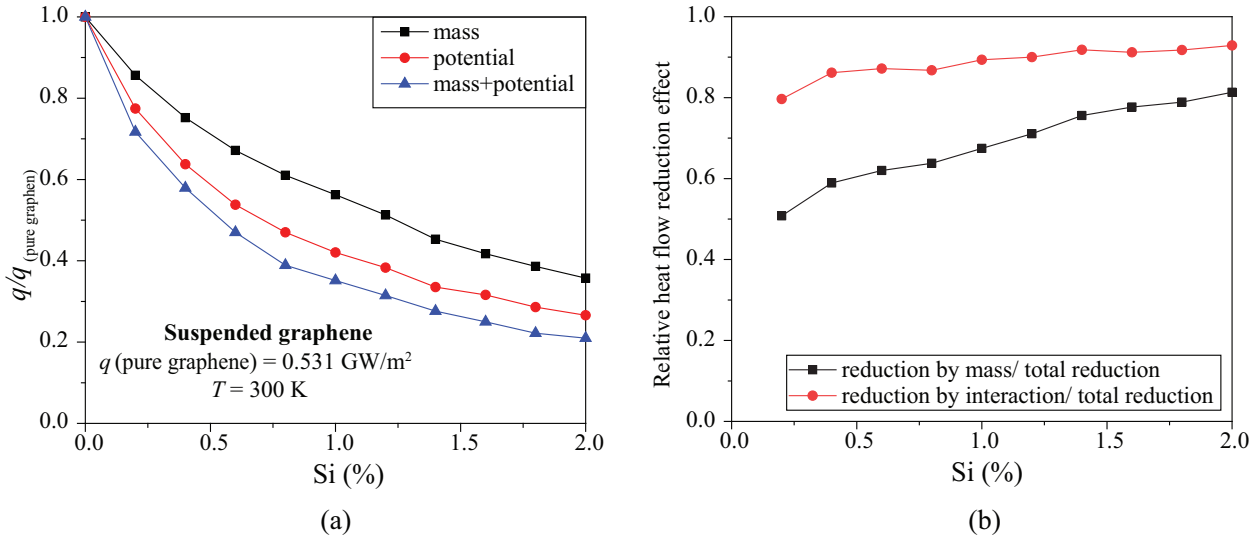


Figure 5.2: (a) Effect of mass, potential, and mass+potential on the in-plane thermal transport of suspended Si-doped graphene as a function of dopant concentration. (b) Relative contribution of mass and potential on thermal transport reduction.

Changing only the interatomic potential of the dopant atoms to (C-Si) interactions which is a weaker interaction in comparison to (C-C) interactions, causes larger bonding length which increases the term $\Delta R = \bar{R} - R_i$ in equation 5.2 and induces bond-strength-difference scattering. According to Fig. 5.2, the bond-strength-difference has a higher impact on

reducing the thermal conductivity of the graphene. As expected, when we apply both mass and interaction effect, the thermal conductivity further decreases.

The relative contribution of each scattering term has the same behavior in the supported case (Fig.5.3b), the coupled scattering mechanisms also are increasing as the Si concentration increases in the supported case.

5.4.2 SiO_2 supported graphene

Since out-of-plane phonons which are the primary thermal energy carriers in suspended graphene and these phonon mods can suppress significantly by the substrate [46], doping has a smaller effect on thermal conductivity reduction of supported Si-doped graphene (Fig. 5.3a). However, we can see the same mass-difference, and bond-strength-difference effects for the supported graphene too.

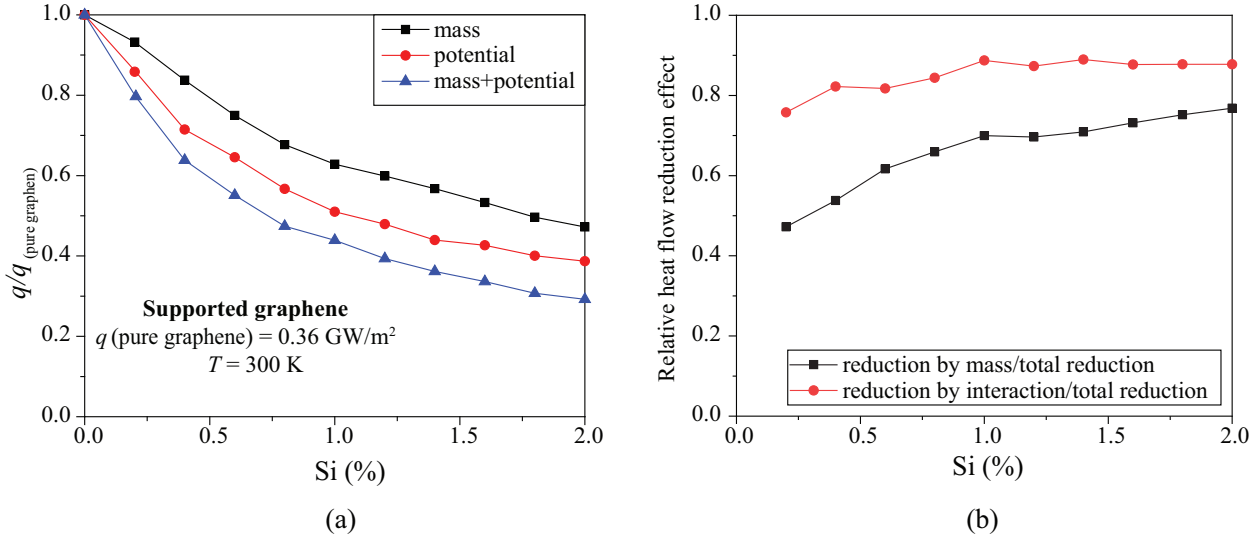


Figure 5.3: (a) Effect of mass, potential, and mass+potential on the in-plane thermal transport of supported Si doped graphene as a function of dopant concentration. (b) Relative contribution of mass and potential on thermal transport reduction.

Studying the effect of Si doping on interfacial thermal resistance between the graphene and SiO_2 substrate (Fig. 5.4) shows that increasing the dopant reduces the interfacial thermal resistance. Because of stronger interactions of Si-Si bonds in comparison with C-Si bonds, the strength of interactions between Si doped graphene and substrate increases with increasing the number of Si atoms in the graphene layer.

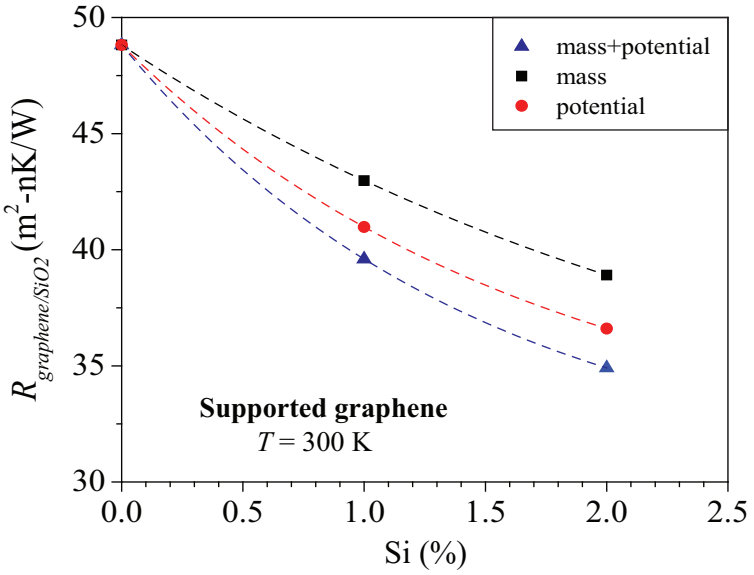


Figure 5.4: Cross-plane interfacial thermal resistance in the supported Si doped graphene with respect to dopant concentration.

By increasing dopant percentage, D_p shows an additional low-energy peak as in Fig. 5.5. The peak created by the potential effect is larger than the one for the only mass effect, and the peak for both effects is the largest, similar to their effect on thermal conductivity. The stronger interaction constrains the motions of constituent atoms neighboring the interfaces, analogous to linkage to very heave mass, which we attribute the appearance and increase of low-energy phonon peak too.

The peak is sharp and narrow; thus, we deduce that the phonon is localized (or not propagated) in the out-of-plane direction. Additionally, the out-of-plane mode, which the peak belongs to, has a minor contribution to in-plane thermal transport in the supported graphene [46], and the in-plane thermal conductivity is decreasing despite an increased phonon population by a larger density of state at the peak. Therefore, the low-energy phonons in the peak do not contribute to in-plane thermal transport, being localized. This low-energy vibration excitation can provide additional transport channels, enhancing local cross-plane interfacial transport as discussed in detail in our previous work [46].

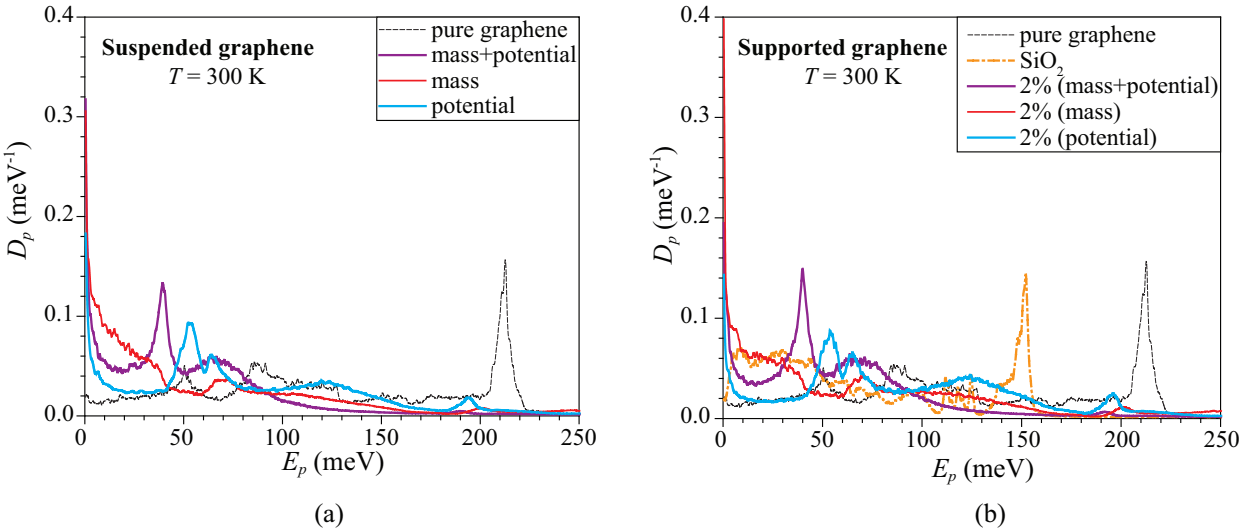


Figure 5.5: (a)D_p's of pure graphene, as well as mass, potential, and mass+potential effect. (b) D_p's of phonon mode polarized in the cross-plane direction (z) for pure graphene, as well as mass, potential, and mass+potential effect. The near zero phonon peak appears for the doped graphene and similar to previous results, the potential has a larger effect in comparison with mass effect.

As discussed above, phonons with long wavelength (low frequency) dominantly contribute to thermal transport due to their high transmission across interfaces, and this additional channel enhances the cross-plane thermal transport vividly; thus, the larger peak by higher dopant concentration can lead to the lower interfacial resistance.

5.5 Conclusions

Phonon transport is significantly influenced by the point-defect scattering, which can reduce in-plane thermal conductivity dramatically (∼80%). Si doping creates local phonon scattering, induced by mass- and bond-strength-mismatches, which increases the total phonon scattering, reducing the phonon relaxation time. Since the out-of-plane phonons (the primary energy carriers for the in-plane thermal transport) are scattered by the substrate, the effect of phonon-point defect (impurity) scattering in supported Si-doped graphene on in-plane thermal conductivity is smaller than suspended graphene.

The graphene/SiO_2 interfacial transport can be effectively controlled by the dopant concentration, thus the variation in out-of-plane phonon mode. Increasing dopant concentration

creates the additional low-frequency transport channel in the out-of-plane mode, which effectively reduces interfacial thermal resistance (by $\sim$30%).

This study offers insights on thermal transport properties in Si-doped graphene heterostructures, which can be employed for the thermal system design and analysis of graphene devices. Effective, anisotropic thermal transport control proposed in this research is beneficial in many engineering applications.

Chapter 6

Conclusions

6.1 Summary and Contributions

Various methods for controlling in-plane and cross-plane thermal transport are investigated via molecular dynamics (MD) simulations. Fundamental carrier properties calculated by MD (e.g., phonon density of states, local heat flux vectors, and contributions of out-of-plane and in-plane phonon modes to thermal transport) supports mechanisms of selective and dynamic thermal transport control suggested in this study, enhancing the understanding of nanoscale thermal conduction phenomena.

To control the in-plane thermal transport of graphene, various means, including interfacial interaction and structural and point defects, have been examined to alter the kinetics of phonon scattering. Introduction of cross-plane interaction by supported and suspended structures changes phonon spectrum and scattering kinetics in the out-of-plane mode, which significantly reduces in-plane thermal conductivity of graphene. Nanosize structural defects induce drastic change of phonon scattering kinetics, and this study demonstrates the control of hole size and arrangement enables not only considerable change of thermal conductivity but also asymmetric behaviors of thermal transport. Si doping induces phonon-point scattering due to both mass and atomic interaction mismatches, and ∼80% of thermal transport reduction by 2% of Si doping is observed in this study.

To control cross-plane thermal transport, we can use mechanical forces to the interface. The simulation results confirm that by applying force to the interface of a sandwiched graphene layer between Si blocks we can reduce the interfacial thermal resistance by 50% (when 2.6 GPa pressure applied to the interface by external forces). It is interesting that applying force to the interface, does not affect in-plane thermal conductivity of sandwiched graphene (2.6 GPa pressure to the interface reduces in-plane thermal conductivity by 3.5%). Some of the methods used to control in-pane thermal conductivity, can be used to alter cross-plane thermal transport, too. For example, creating geometrical defects (holes) in graphene nanomeshs (GNMs), can reduce interfacial thermal transport by weakening graphene structure and reducing the average distance between GNM and the substrate. Si doping also reduces interfacial thermal transport by creating a near zero frequency phonons with higher transmission and enhancing cross-plane thermal transport.

The main finding of each applied method of controlling thermal transport can be summarized as follows:

- The substrate induces the phonon scattering especially out-of-plane modes, which are prohibited in suspended 2D graphene, reducing in-plane thermal conductivity of supported graphene. Adding another contact surface in the sandwiched graphene system increases the substrate activated scattering of the out-of-plane modes, and applying a pressure leads to change in out-of-plane phonon modes. The change in conductivity (k) is not significant for the sandwiched and pressurized sandwiched structure, indicating thermal energy is transported dominantly by in-plane phonons which are almost invariant with pressure application. In contrast, the cross-plane interactions which can effectively control the graphene/Si interfacial transport, by variation of the out-of-plane phonon mode. Applying the pressure for the interaction control effectively reduces interfacial thermal resistance by creating additional low-frequency transport channel in the out-of-plane mode (by 50% with 2.6 GPa, while in-plane conductivity reduces by 3.5%).

- Propagation of thermal energy carriers can have redirected by geometrical confinements on graphene which can effectively control thermal transport. The transport channel scale (width) in GNMs is critical to resultant variations of in-plane thermal transport. Although additional scattering caused by the GNM supporting substrate do not change the tendencies of conductivity variation by porosity and arrangement, their influences on in-plane transport are weakened by diversified scattering mechanisms. Contrarily, GNM porosity is shown to greatly affect cross-plane transport as interfacial thermal resistance decreases with increasing porosity. As the average atomic distance between the substrate and GNM is reduced due to structure weakening from broken bonds near holes, the strength of vdW interactions increase between the two layers. With increasing porosity of supported GNM, we observe heat leakage to the substrate stemming from decreases of in-plane conductivity and cross-plane thermal resistance; considerations should be given to this diversion of heat flow within conductivity measurements and simulations for improved accuracy. This study shows that

geometrical confinements can be used as an effective means to control heat flow direction and magnitude providing possible extension to enhanced thermal system design and evaluation of electronics.

- Geometrical confinement by hole structures leads to selective phonon transport depending on propagation direction, reducing thermal conductance. The resulting distribution of phonon propagation direction is equilibrated through momentum relaxation after lateral phonon confinement. With an asymmetric structure and nanoscale dimension in ballistic regime, the extent of relaxation depends on the heat flow direction, and this contrast yields to thermal rectification within the asymmetric defect engineered graphene samples. Thermal rectification increases as porosity increases and can reach as high as 78% at room temperature with triangular hole arrangement with porosity of 75%. The proposed method of inducing thermal rectification within graphene sheets is both experimentally and economically feasible. In contrast to previous thermal rectification studies, which require complex geometries or impractical graphene sheet tailoring, our results demonstrate that thermal rectification can be achieved by creating asymmetric hole arrangements, without altering the overall rectangular shape of the device. By controlling the hole size and position, we can manipulate the thermal rectification value, thus enabling effective and precise thermal rectification for advanced thermal management and phononic device.

- Phonon transport is significantly influenced by the point-defect scattering, which can reduce in-plane thermal conductivity dramatically ($\sim$80%). Si doping creates local phonon scattering induced by mass-difference, and bond-strength-difference effects, which this increases the total phonon scattering, reducing thermal transport. Since the out-of-plane phonons (the primary energy carriers for the in-plane thermal transport) are scattered by the substrate, influence of enhanced point defect scattering is smaller in supported graphene. The graphene/SiO_2 interfacial thermal transport can be effectively controlled by the dopant concentration. Increasing dopant concentration

creates the additional low-frequency transport channel in the out-of-plane mode, which effectively reduces interfacial thermal resistance (by ∼30%).

This research covers various approaches of controlling heat conduction in freestanding graphene and graphene heterostructures, and proposes new mechanisms of controlling heat transfer direction and magnitude. By calculating and discussing fundamental properties involved in the thermal properties of materials, this study provides deeper insights to the ongoing physics behind thermal transport control and suggests new and precise methods to enhance and improve design of electronic, phononic, and energy conversion devices.

6.2 Recommendation for Further Studies

Although MD simulations can predict various mechanical, and thermal properties, it is limited to atomistic vibration (i.e., phonon transport) simulations and electron transport can not be included in MD simulations. The current computing power, and available MD algorithms are the limiting factors of spatial and temporal dimension. Because of mentioned limiting factors graphene simulation in this work is limited to nanoscale and the simulation time lengths are limited to few nano seconds. To further enhance physical understanding and control thermal transport in more effective way, exploring different approaches, structures and simulation methods can be useful. Here, possible extensions of this advanced thermal transport control study are suggested.

This research have explored methods of reducing thermal conductivity of graphene for possible thermoelectric energy conversion applications. Performing Density Functional Theory (DFT) simulations to predict electron transport and calculate TE power factor ($\sigma_e S^2$, σ_e: electrical conductivity and S: Seebeck coefficient) will provide more insight to improve TE devices design. However, DFT simulations for large systems sizes to include the proposed holes sized in this research is not computationally affordable at this time.

Since altering material structure through the proposed methods in this study can affect electronic transport too, performing a comprehensive multi-scale simulation of thermal and electronic transport simulations will be a useful extension to this study. By obtaining electronic and thermal properties from DFT and MD simulations and applying them as

input to larger scale simulations using finite element method (FEM) and computational fluid dynamics (CFD) can provide all necessary insights and understanding for a real size engineering electronic and energy conversion device design.

The results of this study showed that by creating asymmetric scattering we can induce thermal rectification in graphene layer. This research used geometrical defects to induce scattering. Asymmetric point-defect scattering (i.e., doping) can be used to create materials with asymmetric thermal transport behavior which can act as thermal rectifiers (Fig. 6.1a).

Interfacial thermal transport can also be studied in the asymmetric systems. For example, asymmetric external mechanical force can be used to produce interfacial thermal resistance distribution at the interface and control interfacial thermal transport in a non-uniform way (Fig. 6.1b).

The proposed thermal rectification method for nano-structures can be employed to create micro- and macro-size materials with thermal rectification properties. Assembling thermal nanoscale rectifiers in series or parallel arrangements can be used to buildup macro-size thermal rectifiers (Fig. 6.1c).

In addition to graphene systems, other 2D materials structures like MoS_2, h-BN, etc. and other substrate systems (polymer, etc.) can also be promising research topic for novel electronic, energy conversion and storage applications.

6.3 Outlook

Although nanoscale MD investigations might appear to be far from macro-, and micro-scale domain for engineering applications, understanding the fundamentals of the nanoscale physics and underlying phenomena, which determine material properties, become increasingly essential as new demands arise for designing materials with a higher efficiency and desired properties. As the computational abilities grow and innovative algorithms are developed, atomistic simulations will continue to improve to predict and calculate required principles for understanding of the ongoing physics in larger scales.

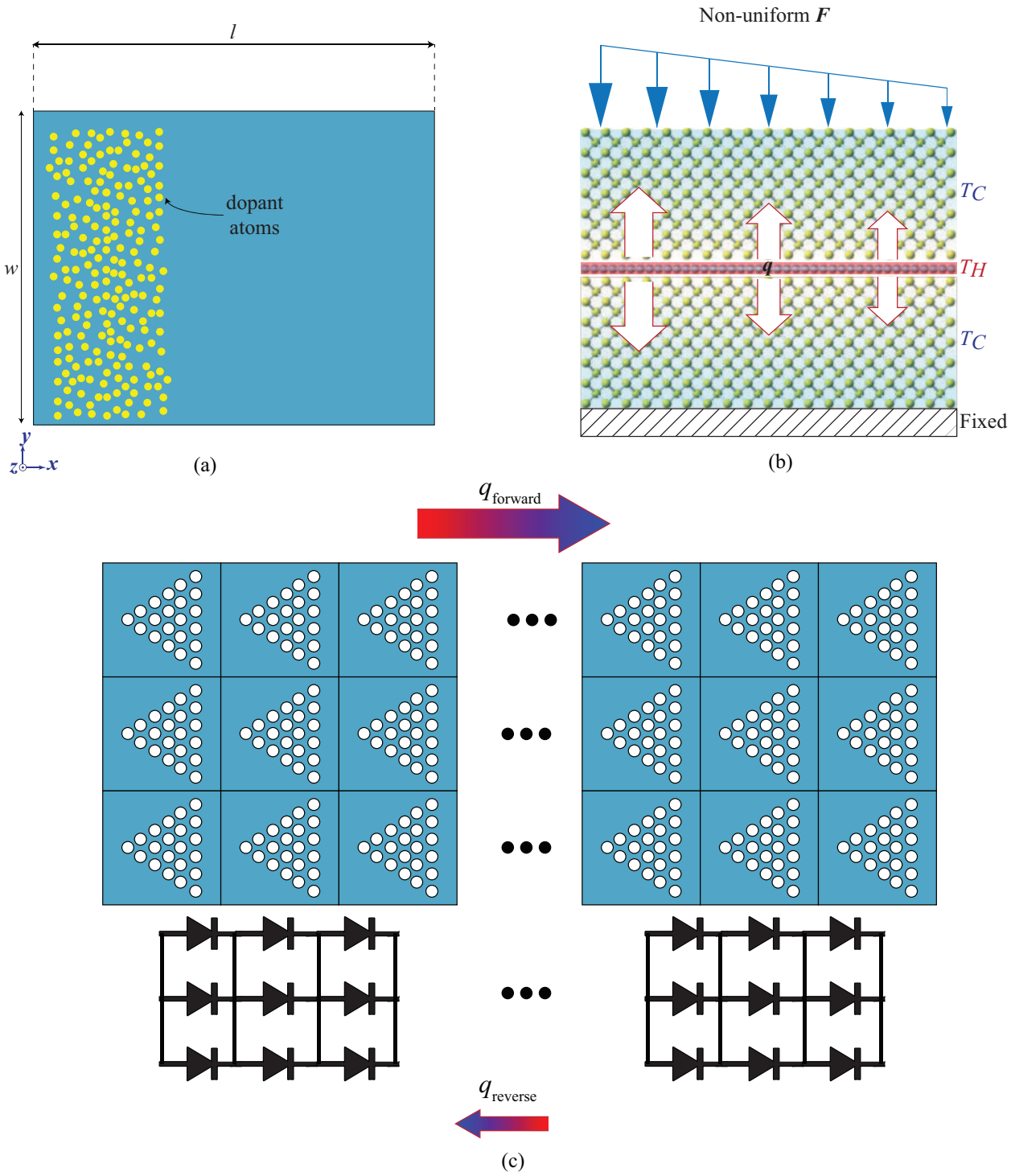


Figure 6.1: (a) Applying asymmetric doping to generate thermal rectification in graphene layer. (b) Asymmetric interfacial thermal transport induced by non-uniform pressure applied to the interface. (c) Assembling nano thermal rectifiers to create micro and macro thermal rectifiers.

6.4 Publications

6.4.1 Journal publications

1) Ali Yousefzadi Nobakht, and Seungha Shin. "*Anisotropic control of thermal transport in graphene/Si heterostructures.*" Journal of Applied Physics 120.22 (2016): 225111. [46]

2) Drew C. Marable, Seungha Shin, and **Ali Yousefzadi Nobakht**. "*Investigation into the microscopic mechanisms influencing convective heat transfer of water flow in graphene nanochannels.*" International Journal of Heat and Mass Transfer 109 (2017): 28-39. [135]

3) Ali Yousefzadi Nobakht, Seungha Shin, Kenneth D. Kihm, Drew C. Marable, and Woomin Lee. "*Heat flow diversion in supported graphene nanomesh.*" Carbon 123 (2017): 45-53. [47]

4) Ali Yousefzadi Nobakht, Yasser Ashraf Gandomi, Jiaqi Wang, Matthew H. Bowman, Drew C. Marable, Benton E. Garrison, Daekun Kim, Seungha Shin. "*Thermal rectification via asymmetric structural defects in graphene.*" Carbon 132 (2018): 565-572. [48]

5) Jiaqi Wang, **Ali Yousefzadi Nobakht**, Seungha Shin, Amit Shyam. "*Structural Deformation and Transformation of θ'-Al_2Cu Precipitate in Al Matrix via Interfacial Diffusion.*" Computational Materials Science, *Under Review.*

6) Manav Vohra, **Ali Yousefzadi Nobakht**, Seungha Shin, Sankaran Mahadevan. "*Uncertainty Quantification in Non-Equilibrium Molecular Dynamics Simulations of Thermal Transport.*" International Journal of Heat and Mass Transfer, *Under Review.* [193]

7) Ondrej Dyck, Feng Bao, Maxim Ziatdinov, **Ali Yousefzadi Nobakht**, Seungha Shin, Kody Law, Artem Maksov, Bobby G. Sumpter, Richard Archibald, Stephen Jesse, Sergei V. Kalinin. "*Single atom force measurements: mapping potential energy landscapes via electron beam induced single atom dynamics.*" Nature Nanotechnology, *Under Review.* [194]

8) Ali Yousefzadi Nobakht, Seungha Shin, and Jiaqi Wang. "*Asymmetric Thermal Transport by Adjusting Structural Defects.*" AIAA Journal, *Under Review.*

9) Ali Yousefzadi Nobakht, James D. Blanks, Jiaqi Wang, Hassan Rezayat and Seungha Shin. "*Effect of Precipitate Geometry on Thermal Transport in Aluminum Alloys.*" Computational Materials Science, *Under Review.*

6.4.2 Conference presentations

1) Ali Yousefzadi Nobakht, and Seungha Shin. "*Pressure effects on in-plane and cross-plane thermal transport within graphene heterostructures*" ASME 2016 SHTC Summer Heat Transfer Conference.

2) Ali Yousefzadi Nobakht, and Seungha Shin. "*Control of thermal transport in graphene and graphene nanomesh heterostructures*" ASME 2017 SHTC Summer Heat Transfer Conference.

3) Ali Yousefzadi Nobakht, and Seungha Shin. "*Control of thermal transport in graphene/Si heterostructures*" ASME 2017 INTERPACK® Packaging and Integration of Electronic and Photonic Microsystems.

4) Ali Yousefzadi Nobakht, and Seungha Shin. "*Diversion of heat flow in supported graphene nanomeshes*" ASME 2017 INTERPACK® Packaging and Integration of Electronic and Photonic Microsystems.

Bibliography

[1] Massoud Kaviany. *Heat transfer physics*. Cambridge University Press, 2014. 2, 3, 5, 20

[2] Mark Lundstrom. *Fundamentals of carrier transport*. Cambridge University Press, 2009. 2, 3

[3] David L King, Jay A Kratochvil, and William E Boyson. Temperature coefficients for pv modules and arrays: measurement methods, difficulties, and results. In *Photovoltaic Specialists Conference, 1997., Conference Record of the Twenty-Sixth IEEE*, pages 1183–1186. IEEE, 1997. 2

[4] Pravin M Kulkarni, Dhirendra Rana, KP Karunakaran, Asim Tewari, and Prathmesh Joshi. Additive manufacturing of directionally heat conductive objects. *Agile Manufacturing Systems*, 5, 2016. 2

[5] Jun Fukai, Makoto Kanou, Yoshikazu Kodama, and Osamu Miyatake. Thermal conductivity enhancement of energy storage media using carbon fibers. *Energy Conversion and Management*, 41(14):1543–1556, 2000. 2, 26

[6] HS Gwon, SH Kim, R Kasada, and Satoshi Konishi. Anisotropic heat transfer characteristics of composite material enhanced with high thermal conductivity fiber. In *2013 IEEE 25th Symposium on Fusion Engineering (SOFE)*, pages 1–4. IEEE, 2013. 2, 26

[7] Nick A Roberts and DG Walker. A review of thermal rectification observations and models in solid materials. *International Journal of Thermal Sciences*, 50(5):648–662, 2011. 2, 47

[8] Nianbei Li, Jie Ren, Lei Wang, Gang Zhang, Peter Hänggi, and Baowen Li. Colloquium: Phononics: Manipulating heat flow with electronic analogs and beyond. *Reviews of Modern Physics*, 84(3):1045, 2012. 3

[9] Mingsheng Xu, Tao Liang, Minmin Shi, and Hongzheng Chen. Graphene-like two-dimensional materials. *Chemical reviews*, 113(5):3766–3798, 2013. 3, 4

[10] Ruben Mas-Balleste, Cristina Gomez-Navarro, Julio Gomez-Herrero, and Felix Zamora. 2d materials: to graphene and beyond. *Nanoscale*, 3(1):20–30, 2011. 3

[11] Hyun-Jung Choi, Sun-Min Jung, Jeong-Min Seo, Dong Wook Chang, Liming Dai, and Jong-Beom Baek. Graphene for energy conversion and storage in fuel cells and supercapacitors. *Nano Energy*, 1(4):534–551, 2012. 3

[12] Nanda Gopal Sahoo, Yongzheng Pan, Lin Li, and Siew Hwa Chan. Graphene-based materials for energy conversion. *Advanced Materials*, 24(30):4203–4210, 2012. 3

[13] Yuka Tsuboi, Feijiu Wang, Daichi Kozawa, Kazuma Funahashi, Shinichiro Mouri, Yuhei Miyauchi, Taishi Takenobu, and Kazunari Matsuda. Enhanced photovoltaic performances of graphene/si solar cells by insertion of a mos 2 thin film. *Nanoscale*, 7 (34):14476–14482, 2015. 3

[14] MA Gluba, D Amkreutz, GV Troppenz, J Rappich, and NH Nickel. Embedded graphene for large-area silicon-based devices. *Applied Physics Letters*, 103(7):073102, 2013. 3

[15] Kostya S Novoselov, Andre K Geim, Sergei V Morozov, D Jiang, Y_ Zhang, Sergey V Dubonos, Irina V Grigorieva, and Alexandr A Firsov. Electric field effect in atomically thin carbon films. *science*, 306(5696):666–669, 2004. 4, 29

[16] Yuanbo Zhang, Yan-Wen Tan, Horst L Stormer, and Philip Kim. Experimental observation of the quantum hall effect and berry's phase in graphene. *nature*, 438 (7065):201, 2005. 4

[17] Andre K Geim and Konstantin S Novoselov. The rise of graphene. *Nature materials*, 6(3):183, 2007. 4

[18] Alexander A Balandin, Suchismita Ghosh, Wenzhong Bao, Irene Calizo, Desalegne Teweldebrhan, Feng Miao, and Chun Ning Lau. Superior thermal conductivity of single-layer graphene. *Nano letters*, 8(3):902–907, 2008. 4, 10, 16, 29, 47

[19] S Ghosh, I Calizo, D Teweldebrhan, EP Pokatilov, DL Nika, AA Balandin, W Bao, F Miao, and C Ning Lau. Extremely high thermal conductivity of graphene: Prospects for thermal management applications in nanoelectronic circuits. *Applied Physics Letters*, 92(15):151911, 2008. 4, 10, 15, 16, 29, 35, 54

[20] Changgu Lee, Xiaoding Wei, Jeffrey W Kysar, and James Hone. Measurement of the elastic properties and intrinsic strength of monolayer graphene. *science*, 321(5887): 385–388, 2008. 4

[21] Fang Liu, Pingbing Ming, and Ju Li. Ab initio calculation of ideal strength and phonon instability of graphene under tension. *Physical Review B*, 76(6):064120, 2007. 4

[22] LA Falkovsky. Optical properties of graphene. In *Journal of Physics: Conference Series*, volume 129, page 012004. IOP Publishing, 2008. 4

[23] Matthias C Schabel and José Luís Martins. Energetics of interplanar binding in graphite. *Physical Review B*, 46(11):7185, 1992. 4

[24] Ageeth A Bol, Amal Kasry, Ahmed Maarouf, Glenn J Martyna, Dennis M Newns, Razvan A Nistor, and George S Tulevski. Graphene solar cell, June 27 2013. US Patent App. 13/772,990. 4

[25] Shengrui Sun, Lian Gao, and Yangqiao Liu. Enhanced dye-sensitized solar cell using graphene-tio 2 photoanode prepared by heterogeneous coagulation. *Applied physics letters*, 96(8):083113, 2010. 4

[26] Zongyou Yin, Jixin Zhu, Qiyuan He, Xiehong Cao, Chaoliang Tan, Hongyu Chen, Qingyu Yan, and Hua Zhang. Graphene-based materials for solar cell applications. *Advanced energy materials*, 4(1), 2014. 4

[27] Yen-Chia Chen, Ting Cao, Chen Chen, Zahra Pedramrazi, Danny Haberer, Dimas G De Oteyza, Felix R Fischer, Steven G Louie, and Michael F Crommie. Molecular bandgap engineering of bottom-up synthesized graphene nanoribbon heterojunctions. *Nature nanotechnology*, 10(2):156, 2015. 4

[28] L Vicarelli, MS Vitiello, D Coquillat, A Lombardo, AC Ferrari, W Knap, M Polini, V Pellegrini, and A Tredicucci. Graphene field-effect transistors as room-temperature terahertz detectors. *Nature Materials*, 11(10):865–871, 2012. 4, 10

[29] D Dragoman and M Dragoman. Giant thermoelectric effect in graphene. *Applied Physics Letters*, 91(20):203116, 2007. 4, 29, 62

[30] H Mahabadipour and H Ghaebi. Development and comparison of two expander cycles used in refrigeration system of olefin plant based on exergy analysis. *Applied Thermal Engineering*, 50(1):771–780, 2013. 4, 29, 62

[31] Yijian Ouyang and Jing Guo. A theoretical study on thermoelectric properties of graphene nanoribbons. *Applied Physics Letters*, 94(26):263107, 2009. 4, 29, 62

[32] Jae Hun Seol, Insun Jo, Arden L Moore, Lucas Lindsay, Zachary H Aitken, Michael T Pettes, Xuesong Li, Zhen Yao, Rui Huang, David Broido, Natalio Mingo, Rodney S Ruoff, and Shi. Li. Two-dimensional phonon transport in supported graphene. *Science*, 328(5975):213–216, 2010. 4, 10, 29, 30, 62

[33] F Schedin, AK Geim, SV Morozov, EW Hill, P Blake, MI Katsnelson, and KS Novoselov. Detection of individual gas molecules adsorbed on graphene. *Nature materials*, 6(9):652, 2007. 4

[34] Xiaochang Miao, Sefaattin Tongay, Maureen K Petterson, Kara Berke, Andrew G Rinzler, Bill R Appleton, and Arthur F Hebard. High efficiency graphene solar cells by chemical doping. *Nano letters*, 12(6):2745–2750, 2012. 4

[35] Suchismita Ghosh, Wenzhong Bao, Denis L Nika, Samia Subrina, Evghenii P Pokatilov, Chun Ning Lau, and Alexander A Balandin. Dimensional crossover of thermal transport in few-layer graphene. *Nature Materials*, 9(7):555, 2010. 4, 47

[36] Denis L Nika, Artur S Askerov, and Alexander A Balandin. Anomalous size dependence of the thermal conductivity of graphene ribbons. *Nano Letters*, 12(6):3238–3244, 2012. 4, 47

[37] Alexander A Balandin. Thermal properties of graphene and nanostructured carbon materials. *Nature Materials*, 10(8):569–581, 2011. 4, 47, 62

[38] S.M. Unger and G.T. Riddle. Integrated circuit subassembly with thermally anisotropic heat transfer element. *US Patenet*, 6(104):104,090, August 15 2000. URL https://www.google.com/patents/US6104090. 5, 26

[39] Seungha Shin and Massoud Kaviany. Interflake thermal conductance of edge-passivated graphene. *Physical Review B*, 84(23):235433, 2011. 5

[40] Eric S Toberer, Lauryn L Baranowski, and Chris Dames. Advances in thermal conductivity. *Annual Review of Materials Research*, 42:179–209, 2012. 5

[41] Kwangnam Kim and Massoud Kaviany. Thermal conductivity switch: Optimal semiconductor/metal melting transition. *Physical Review B*, 94(15):155203, 2016. 5

[42] Bing-Yang Cao, Wen-Jun Yao, and Zhen-Qiang Ye. Networked nanoconstrictions: An effective route to tuning the thermal transport properties of graphene. *Carbon*, 96: 711–719, 2016. 5, 29, 31, 51, 65

[43] Tianli Feng and Xiulin Ruan. Ultra-low thermal conductivity in graphene nanomesh. *Carbon*, 101:107–113, 2016. 5, 29, 36

[44] John M Ziman. *Electrons and phonons: the theory of transport phenomena in solids*. Oxford university press, 1960. 5, 66

[45] Shanshan Chen, Qingzhi Wu, Columbia Mishra, Junyong Kang, Hengji Zhang, Kyeongjae Cho, Weiwei Cai, Alexander A Balandin, and Rodney S Ruoff. Thermal conductivity of isotopically modified graphene. *Nature materials*, 11(3):203, 2012. 6, 29, 30, 48, 62, 66

[46] Ali Yousefzadi Nobakht and Seungha Shin. Anisotropic control of thermal transport in graphene/si heterostructures. *Journal of Applied Physics*, 120(22):225111, 2016. 6, 30, 35, 41, 52, 65, 68, 69, 79

[47] Ali Yousefzadi Nobakht, Seungha Shin, Kenneth D Kihm, Drew C Marable, and Woomin Lee. Heat flow diversion in supported graphene nanomesh. *Carbon*, 123: 45–53, 2017. 6, 47, 48, 52, 62, 79

[48] Ali Yousefzadi Nobakht, Yasser Ashraf Gandomi, Jiaqi Wang, Matthew H Bowman, Drew C Marable, Benton E Garrison, Daekun Kim, and Seungha Shin. Thermal rectification via asymmetric structural defects in graphene. *Carbon*, 132:565–572, 2018. 6, 79

[49] Arman Vassighi and Manoj Sachdev. *Thermal and power management of integrated circuits*. Springer Science & Business Media, 2006. 10

[50] Phaedon Avouris, Zhihong Chen, and Vasili Perebeinos. Carbon-based electronics. *Nature nanotechnology*, 2(10):605–615, 2007. 10

[51] Kirill I Bolotin, KJ Sikes, Zd Jiang, M Klima, G Fudenberg, J Hone, Ph Kim, and HL Stormer. Ultrahigh electron mobility in suspended graphene. *Solid State Communications*, 146(9):351–355, 2008. 10, 29

[52] SV Morozov, KS Novoselov, MI Katsnelson, F Schedin, DC Elias, JA Jaszczak, and AK Geim. Giant intrinsic carrier mobilities in graphene and its bilayer. *Physical Review Letters*, 100(1):016602, 2008. 10, 16

[53] Simone Bertolazzi, Daria Krasnozhon, and Andras Kis. Nonvolatile memory cells based on mos2/graphene heterostructures. *ACS nano*, 7(4):3246–3252, 2013. 10

[54] Eric Pop, Vikas Varshney, and Ajit K Roy. Thermal properties of graphene: Fundamentals and applications. *MRS bulletin*, 37(12):1273–1281, 2012. 10, 15, 16, 36, 62

[55] Z Chen, W Jang, W Bao, CN Lau, and C Dames. Thermal contact resistance between graphene and silicon dioxide. *Applied Physics Letters*, 95(16):161910, 2009. 10

[56] Wanyoung Jang, Zhen Chen, Wenzhong Bao, Chun Ning Lau, and Chris Dames. Thickness-dependent thermal conductivity of encased graphene and ultrathin graphite. *Nano letters*, 10(10):3909–3913, 2010. 10

[57] Yee Kan Koh, Myung-Ho Bae, David G Cahill, and Eric Pop. Heat conduction across monolayer and few-layer graphenes. *Nano Letters*, 10(11):4363–4368, 2010. 10

[58] L Lindsay, DA Broido, and Natalio Mingo. Flexural phonons and thermal transport in graphene. *Physical Review B*, 82(11):115427, 2010. 10, 16, 39

[59] Kin Fai Mak, Chun Hung Lui, and Tony F Heinz. Measurement of the thermal conductance of the graphene/SiO_2 interface. *Applied Physics Letters*, 97(22):221904, 2010. 10

[60] Ashley M DaSilva, Ke Zou, JK Jain, and Jun Zhu. Mechanism for current saturation and energy dissipation in graphene transistors. *Physical Review Letters*, 104(23): 236601, 2010. 10

[61] Marcus Freitag, Mathias Steiner, Yves Martin, Vasili Perebeinos, Zhihong Chen, James C Tsang, and Phaedon Avouris. Energy dissipation in graphene field-effect transistors. *Nano Letters*, 9(5):1883–1888, 2009. 10

[62] Inanc Meric, Melinda Y Han, Andrea F Young, Barbaros Ozyilmaz, Philip Kim, and Kenneth L Shepard. Current saturation in zero-bandgap, top-gated graphene field-effect transistors. *Nature Nanotechnology*, 3(11):654–659, 2008. 10

[63] Chenhan Liu, Zhiyong Wei, Weiyu Chen, Kedong Bi, Juekuan Yang, and Yunfei Chen. Pressure effects on the thermal resistance of few-layer graphene. *Physics Letters A*, 380(1):248–254, 2016. 10, 23

[64] Carl Fredrik Carlborg, Junichiro Shiomi, and Shigeo Maruyama. Thermal boundary resistance between single-walled carbon nanotubes and surrounding matrices. *Physical Review B*, 78(20):205406, 2008. 10, 14, 21, 33, 34, 65

[65] Steve Plimpton. Fast parallel algorithms for short-range molecular dynamics. *Journal of Computational Physics*, 117(1):1–19, 1995. 11, 31, 48, 63

[66] Steven J Stuart, Alan B Tutein, and Judith A Harrison. A reactive potential for hydrocarbons with intermolecular interactions. *The Journal of Chemical Physics*, 112 (14):6472–6486, 2000. 11, 30, 48, 63

[67] Frank H Stillinger and Thomas A Weber. Computer simulation of local order in condensed phases of silicon. *Physical review B*, 31(8):5262, 1985. 11, 30

[68] Tobias Hertel, Robert E Walkup, and Phaedon Avouris. Deformation of carbon nanotubes by surface van der waals forces. *Physical Review B*, 58(20):13870, 1998. 12, 30

[69] Jianliang Xiao, Simon Dunham, Ping Liu, Yongwei Zhang, Coskun Kocabas, Lionel Moh, Yonggang Huang, Keh-Chih Hwang, Chun Lu, Wei Huang, and John A Rogers. Alignment controlled growth of single-walled carbon nanotubes on quartz substrates. *Nano Letters*, 9(12):4311–4319, 2009. 12, 30

[70] Anthony K Rappé, Carla J Casewit, KS Colwell, WA Goddard Iii, and WM Skiff. Uff, a full periodic table force field for molecular mechanics and molecular dynamics simulations. *Journal of the American Chemical Society*, 114(25):10024–10035, 1992. 12, 25, 31

[71] Jie Chen, Gang Zhang, and Baowen Li. Impacts of atomistic coating on thermal conductivity of germanium nanowires. *Nano Letters*, 12(6):2826–2832, 2012. 12

[72] Soon-Ho Choi, Shigeo Maruyama, Kyung-Kun Kim, and Jung-Hye Lee. Evaluation of the phonon mean free path in thin films by using classical molecular dynamics. *Journal-Korean Physical Society*, 43(1):747–753, 2003. 12

[73] Aron Cummings, Mohamed Osman, Deepak Srivastava, and Madhu Menon. Thermal conductivity of y-junction carbon nanotubes. *Physical Review B*, 70(11):115405, 2004. 12

[74] Yufei Gao, Wenbo Bao, Qingyuan Meng, Yuhang Jing, and Xiaoxu Song. The thermal transport properties of single-crystalline nanowires covered with amorphous shell: A molecular dynamics study. *Journal of Non-Crystalline Solids*, 387:132–138, 2014. 12

[75] ZhengXing Huang and ZhenAn Tang. Evaluation of momentum conservation influence in non-equilibrium molecular dynamics methods to compute thermal conductivity. *Physica B: Condensed Matter*, 373(2):291–296, 2006. 12, 31, 49, 65

[76] Patrick K Schelling, Simon R Phillpot, and Pawel Keblinski. Comparison of atomic-level simulation methods for computing thermal conductivity. *Physical Review B*, 65 (14):144306, 2002. 12, 16, 31, 49, 51, 65

[77] Yanwu Zhu, Shanthi Murali, Weiwei Cai, Xuesong Li, Ji Won Suk, Jeffrey R Potts, and Rodney S Ruoff. Graphene and graphene oxide: synthesis, properties, and applications. *Advanced Materials*, 22(35):3906–3924, 2010. 12, 29, 31

[78] DW Bullett. Chemical pseudopotential approach to covalent bonding. ii. bond lengths and bond energies in diamond, silicon and graphite. *Journal of Physics C: Solid State Physics*, 8(17):2707, 1975. 12

[79] Ryogo Kubo. Statistical-mechanical theory of irreversible processes. I. general theory and simple applications to magnetic and conduction problems. *Journal of the Physical Society of Japan*, 12(6):570–586, 1957. 12, 31, 33, 51

[80] Yang Hong, Lei Li, Xiao Cheng Zeng, and Jingchao Zhang. Tuning thermal contact conductance at graphene–copper interface via surface nanoengineering. *Nanoscale*, 7 (14):6286–6294, 2015. 14

[81] Bo Liu, Julia A Baimova, Chilla D Reddy, Adrian Wing-Keung Law, Sergey V Dmitriev, Hong Wu, and Kun Zhou. Interfacial thermal conductance of a silicene/graphene bilayer heterostructure and the effect of hydrogenation. *ACS Applied Materials & Interfaces*, 6(20):18180–18188, 2014. 14, 33, 65

[82] Jingchao Zhang, Yang Hong, Zhen Tong, Zhihuai Xiao, Hua Bao, and Yanan Yue. Molecular dynamics study of interfacial thermal transport between silicene and substrates. *Physical Chemistry Chemical Physics*, 17(37):23704–23710, 2015. 14

[83] Jingchao Zhang, Yang Hong, and Yanan Yue. Thermal transport across graphene and single layer hexagonal boron nitride. *Journal of Applied Physics*, 117(13):134307, 2015. 14, 21, 34, 65

[84] Jingchao Zhang, Yongchun Wang, and Xinwei Wang. Rough contact is not always bad for interfacial energy coupling. *Nanoscale*, 5(23):11598–11603, 2013. 14, 21, 34, 65

[85] Zhun-Yong Ong and Eric Pop. Molecular dynamics simulation of thermal boundary conductance between carbon nanotubes and SiO_2. *Physical Review B*, 81(15):155408, 2010. 14, 21, 63

[86] Seungha Shin, Massoud Kaviany, Tapan Desai, and Richard Bonner. Roles of atomic restructuring in interfacial phonon transport. *Physical Review B*, 82(8):081302, 2010. 15, 34, 52, 65

[87] Zhiyong Wei, Zhonghua Ni, Kedong Bi, Minhua Chen, and Yunfei Chen. In-plane lattice thermal conductivities of multilayer graphene films. *Carbon*, 49(8):2653–2658, 2011. 15, 16

[88] Myung-Ho Bae, Zuanyi Li, Zlatan Aksamija, Pierre N Martin, Feng Xiong, Zhun-Yong Ong, Irena Knezevic, and Eric Pop. Ballistic to diffusive crossover of heat flow in graphene ribbons. *arXiv preprint arXiv:1304.1179*, 2013. 15, 16, 36

[89] DL Nika, S Ghosh, EP Pokatilov, and AA Balandin. Lattice thermal conductivity of graphene flakes: Comparison with bulk graphite. *Applied Physics Letters*, 94(20): 203103, 2009. 15

[90] Xiangfan Xu, Luiz FC Pereira, Yu Wang, Jing Wu, Kaiwen Zhang, Xiangming Zhao, Sukang Bae, Cong Tinh Bui, Rongguo Xie, John TL Thong, Byung Hee Hong, Kian Ping Loh, Davide Donadio, Baowen Li, and Barbaros Özyilmaz. Length-dependent thermal conductivity in suspended single-layer graphene. *Nature Communications*, 5:3689, 2014. 15, 35, 54

[91] Vikas Varshney, Soumya S Patnaik, Ajit K Roy, George Froudakis, and Barry L Farmer. Modeling of thermal transport in pillared-graphene architectures. *ACS Nano*, 4(2):1153–1161, 2010. 16

[92] YY Zhang, Y Cheng, QX Pei, CM Wang, and Y Xiang. Thermal conductivity of defective graphene. *Physics Letters A*, 376(47):3668–3672, 2012. 16

[93] Kedong Bi, Yunfei Chen, Juekuan Yang, Yujuan Wang, and Minhua Chen. Molecular dynamics simulation of thermal conductivity of single-wall carbon nanotubes. *Physics Letters A*, 350(1):150–153, 2006. 16

[94] Enrique Munoz, Jianxin Lu, and Boris I Yakobson. Ballistic thermal conductance of graphene ribbons. *Nano Letters*, 10(5):1652–1656, 2010. 18

[95] Dhruv Singh, Jayathi Y Murthy, and Timothy S Fisher. Spectral phonon conduction and dominant scattering pathways in graphene. *Journal of Applied Physics*, 110(9): 094312, 2011. 18

[96] Changwook Jeong, Supriyo Datta, and Mark Lundstrom. Full dispersion versus debye model evaluation of lattice thermal conductivity with a landauer approach. *Journal of Applied Physics*, 109(7):073718, 2011. 18

[97] P Scuracchio, A Dobry, S Costamagna, and FM Peeters. Tuning the polarized quantum phonon transmission in graphene nanoribbons. *Nanotechnology*, 26(30):305401, 2015. 21, 41

[98] Zhequan Yan, Liang Chen, Mina Yoon, and Satish Kumar. Phonon transport at the interfaces of vertically stacked graphene and hexagonal boron nitride heterostructures. *Nanoscale*, 8(7):4037–4046, 2016. 21, 41

[99] Weiwei Cai, Arden L Moore, Yanwu Zhu, Xuesong Li, Shanshan Chen, Li Shi, and Rodney S Ruoff. Thermal transport in suspended and supported monolayer graphene grown by chemical vapor deposition. *Nano Letters*, 10(5):1645–1651, 2010. 22

[100] Jingchao Zhang and Xinwei Wang. Thermal transport in bent graphene nanoribbons. *Nanoscale*, 5(2):734–743, 2013. 22

[101] L Britnell, R V Gorbachev, R Jalil, B D Belle, F Schedin, A Mishchenko, T Georgiou, M I Katsnelson, L Eaves, S V Morozov, et al. Field-effect tunneling transistor based on vertical graphene heterostructures. *Science*, 335(6071):947–950, 2012. 29

[102] Insub Jung, Ho Young Jang, Junghyuk Moon, and Sungho Park. Fabrication of a graphene nanomesh using a platinum nano-network as a pattern mask. *Nanoscale*, 6 (12):6482–6486, 2014. 29, 30

[103] Xiaogan Liang, Yeon-Sik Jung, Shiwei Wu, Ariel Ismach, Deirdre L Olynick, Stefano Cabrini, and Jeffrey Bokor. Formation of bandgap and subbands in graphene nanomeshes with sub-10 nm ribbon width fabricated via nanoimprint lithography. *Nano letters*, 10(7):2454–2460, 2010. 29, 30

[104] Jannik C Meyer, Andre K Geim, Mikhail I Katsnelson, Konstantin S Novoselov, Tim J Booth, and Siegmar Roth. The structure of suspended graphene sheets. *arXiv preprint cond-mat/0701379*, 2007. 29

[105] Zhun-Yong Ong, Yongqing Cai, and Gang Zhang. Theory of substrate-directed heat dissipation for single-layer graphene and other two-dimensional crystals. *Physical Review B*, 94(16):165427, 2016. 29

[106] Justin Haskins, Alper Kınacı, Cem Sevik, Hâldun Sevinçli, Gianaurelio Cuniberti, and Tahir Cagın. Control of thermal and electronic transport in defect-engineered graphene nanoribbons. *ACS nano*, 5(5):3779–3787, 2011. 29, 48

[107] Jin-Wu Jiang, Bing-Shen Wang, and Jian-Sheng Wang. First principle study of the thermal conductance in graphene nanoribbon with vacancy and substitutional silicon defects. *Applied Physics Letters*, 98(11):113114, 2011. 29

[108] Tapas Kuila, Saswata Bose, Ananta Kumar Mishra, Partha Khanra, Nam Hoon Kim, and Joong Hee Lee. Chemical functionalization of graphene and its applications. *Progress in Materials Science*, 57(7):1061–1105, 2012. 29, 48

[109] Andrey Y Serov, Zhun-Yong Ong, and Eric Pop. Effect of grain boundaries on thermal transport in graphene. *Applied Physics Letters*, 102(3):033104, 2013. 29, 62

[110] Teng Yong Ng, Jing Jie Yeo, and ZS Liu. A molecular dynamics study of the thermal conductivity of graphene nanoribbons containing dispersed stone–thrower–wales defects. *Carbon*, 50(13):4887–4893, 2012. 29

[111] Hoda Malekpour, Pankaj Ramnani, Srilok Srinivasan, Ganesh Balasubramanian, Denis L Nika, Ashok Mulchandani, Roger K Lake, and Alexander A Balandin. Thermal conductivity of graphene with defects induced by electron beam irradiation. *Nanoscale*, 8(30):14608–14616, 2016. 29, 48

[112] Jiuning Hu, Stephen Schiffli, Ajit Vallabhaneni, Xiulin Ruan, and Yong P Chen. Tuning the thermal conductivity of graphene nanoribbons by edge passivation and isotope engineering: A molecular dynamics study. *Applied Physics Letters*, 97(13): 133107, 2010. 29, 31, 51, 62, 65

[113] Ning Wei, Lanqing Xu, Hui-Qiong Wang, and Jin-Cheng Zheng. Strain engineering of thermal conductivity in graphene sheets and nanoribbons: ademonstration of magic flexibility. *Nanotechnology*, 22(10):105705, 2011. 29, 62

[114] Woomin Lee, Kenneth David Kihm, Hong Goo Kim, Seungha Shin, Changhyuk Lee, Jae Sung Park, Sosan Cheon, Oh Myoung Kwon, Gyumin Lim, and Woorim Lee. In-plane thermal conductivity of polycrystalline chemical vapor deposition graphene with controlled grain sizes. *Nano Letters*, 17(4):2361–2366, 2017. 29, 62

[115] Jinwoo Oh, Hoyeon Yoo, Jaeyoo Choi, Jeong Yun Kim, Dong Su Lee, Myung Jong Kim, Jong-Chan Lee, Woo Nyon Kim, Jeffrey C Grossman, Jong Hyuk Park, et al. Significantly reduced thermal conductivity and enhanced thermoelectric properties of single-and bi-layer graphene nanomeshes with sub-10nm neck-width. *Nano Energy*, 35: 26–35, 2017. 29

[116] Jingwei Bai, Xing Zhong, Shan Jiang, Yu Huang, and Xiangfeng Duan. Graphene nanomesh. *Nature nanotechnology*, 5(3):190–194, 2010. 29, 30, 48

[117] Yong Xu, Zuanyi Li, and Wenhui Duan. Thermal and thermoelectric properties of graphene. *Small*, 10(11):2182–2199, 2014. 30

[118] Zhiyuan Zeng, Xiao Huang, Zongyou Yin, Hong Li, Yang Chen, Hai Li, Qing Zhang, Jan Ma, Freddy Boey, and Hua Zhang. Fabrication of graphene nanomesh by using

an anodic aluminum oxide membrane as a template. *Advanced Materials*, 24(30): 4138–4142, 2012. 30

[119] Lili Jiang and Zhuangjun Fan. Design of advanced porous graphene materials: from graphene nanomesh to 3d architectures. *Nanoscale*, 6(4):1922–1945, 2014. 30

[120] Ali Esfandiar, Nicholas J Kybert, Eric N Dattoli, Gang Hee Han, Mitchell B Lerner, Omid Akhavan, Azam Irajizad, and AT Charlie Johnson. DNA-decorated graphene nanomesh for detection of chemical vapors. *Applied Physics Letters*, 103(18):183110, 2013. 30

[121] Rajat Kanti Paul, Sushmee Badhulika, Nuvia M Saucedo, and Ashok Mulchandani. Graphene nanomesh as highly sensitive chemiresistor gas sensor. *Analytical chemistry*, 84(19):8171–8178, 2012. 30

[122] Salim Berrada, Viet Hung Nguyen, Damien Querlioz, Jérôme Saint-Martin, Alfonso Alarcón, Christophe Chassat, Arnaud Bournel, and Philippe Dollfus. Graphene nanomesh transistor with high on/off ratio and good saturation behavior. *Applied Physics Letters*, 103(18):183509, 2013. 30, 48

[123] Kai-Xuan Chen, Xiao-Ming Wang, Dong-Chuan Mo, and Shu-Shen Lyu. Substrate effect on thermal transport properties of graphene on SiC (0001) surface. *Chemical Physics Letters*, 618:231–235, 2015. 30

[124] Zhi-Xin Guo, JW Ding, and Xin-Gao Gong. Substrate effects on the thermal conductivity of epitaxial graphene nanoribbons. *Physical Review B*, 85(23):235429, 2012. 30

[125] Zhun-Yong Ong and Eric Pop. Effect of substrate modes on thermal transport in supported graphene. *Physical Review B*, 84(7):075471, 2011. 30

[126] Ying Ying Wang, Zhen Hua Ni, Ting Yu, Ze Xiang Shen, Hao Min Wang, Yi Hong Wu, Wei Chen, and Andrew Thye Shen Wee. Raman studies of monolayer graphene: the substrate effect. *The Journal of Physical Chemistry C*, 112(29):10637–10640, 2008. 30

[127] Bladimir Ramos-Alvarado, Satish Kumar, and GP Peterson. On the wettability transparency of graphene-coated silicon surfaces. *The Journal of chemical physics*, 144(1):014701, 2016. 30

[128] Xinming Li, Hongwei Zhu, Kunlin Wang, Anyuan Cao, Jinquan Wei, Chunyan Li, Yi Jia, Zhen Li, Xiao Li, and Dehai Wu. Graphene-on-silicon schottky junction solar cells. *Advanced Materials*, 22(25):2743–2748, 2010. 30

[129] Xiaomu Wang, Zhenzhou Cheng, Ke Xu, Hon Ki Tsang, and Jian-Bin Xu. High-responsivity graphene/silicon-heterostructure waveguide photodetectors. *Nature Photonics*, 7(11):888–891, 2013. 30

[130] Denis L Nika and Alexander A Balandin. Phonons and thermal transport in graphene and graphene-based materials. *Reports on Progress in Physics*, 80(3):036502, 2017. 35, 47

[131] Arnold Eucken. Thermal conductivity of ceramic refractory materials; its calculation from thermal conductivity of constituents. volume 12, page 231, 1933. 36

[132] Tianli Feng and Xiulin Ruan. Prediction of spectral phonon mean free path and thermal conductivity with applications to thermoelectrics and thermal management: a review. *Journal of Nanomaterials*, 2014, 2014. 36

[133] Truong Quoc Vo and BoHung Kim. Transport phenomena of water in molecular fluidic channels. *Scientific Reports*, 6:33881, 2016. 41

[134] Dmitry Alexeev, Jie Chen, Jens H Walther, Konstantinos P Giapis, Panagiotis Angelikopoulos, and Petros Koumoutsakos. Kapitza resistance between few-layer graphene and water: Liquid layering effects. *Nano letters*, 15(9):5744–5749, 2015. 41

[135] Drew Champion Marable, Seungha Shin, and Ali Yousefzadi Nobakht. Investigation into the microscopic mechanisms influencing convective heat transfer of water flow in graphene nanochannels. *International Journal of Heat and Mass Transfer*, 109:28–39, 2017. ISSN 0017-9310. 41, 79

[136] Haidong Wang, Shiqian Hu, Koji Takahashi, Xing Zhang, Hiroshi Takamatsu, and Jie Chen. Experimental study of thermal rectification in suspended monolayer graphene. *Nature Communications*, 8:15843, 2017. 47, 48

[137] Xavier Cartoixa, Luciano Colombo, and Riccardo Rurali. Thermal rectification by design in telescopic si nanowires. *Nano Letters*, 15(12):8255–8259, 2015. 47

[138] Jiuning Hu, Xiulin Ruan, and Yong P Chen. Thermal conductivity and thermal rectification in graphene nanoribbons: a molecular dynamics study. *Nano Letters*, 9(7):2730–2735, 2009. 47, 48

[139] Baowen Li, Lei Wang, and Giulio Casati. Thermal diode: Rectification of heat flux. *Physical Review Letters*, 93(18):184301, 2004. 47, 52

[140] Gang Wu and Baowen Li. Thermal rectification in carbon nanotube intramolecular junctions: Molecular dynamics calculations. *Physical Review B*, 76(8):085424, 2007. 47, 48

[141] Guangping Lei, Huiyuan Cheng, Hantao Liu, and Wenji Rao. Thermal rectification in asymmetric graphyne nanoribbons: A nonequilibrium molecular dynamics study. *Materials Letters*, 189:101–103, 2017. 47

[142] D Sawaki, W Kobayashi, Y Moritomo, and I Terasaki. Thermal rectification in bulk materials with asymmetric shape. *Applied Physics Letters*, 98(8):081915, 2011. 47, 48

[143] Nan Zeng and Jian-Sheng Wang. Mechanisms causing thermal rectification: The influence of phonon frequency, asymmetry, and nonlinear interactions. *Physical Review B*, 78(2):024305, 2008. 47

[144] Nuo Yang, Gang Zhang, and Baowen Li. Carbon nanocone: a promising thermal rectifier. *Applied Physics Letters*, 93(24):243111, 2008. 47, 48

[145] Nuo Yang, Gang Zhang, and Baowen Li. Thermal rectification in asymmetric graphene ribbons. *Applied Physics Letters*, 95(3):033107, 2009. 47, 52

[146] Ping Yang, Xialong Li, Yanfan Zhao, Haiying Yang, and Shuting Wang. Effect of triangular vacancy defect on thermal conductivity and thermal rectification in graphene nanoribbons. *Physics Letters A*, 377(34):2141–2146, 2013. 47, 48, 52

[147] Wei-Rong Zhong, Wei-Hao Huang, Xi-Rong Deng, and Bao-Quan Ai. Thermal rectification in thickness-asymmetric graphene nanoribbons. *Applied Physics Letters*, 99(19):193104, 2011. 47

[148] Bambi Hu and Lei Yang. Heat conduction in the frenkel–kontorova model. *Chaos: An Interdisciplinary Journal of Nonlinear Science*, 15(1):015119, 2005. 47

[149] Bambi Hu, Lei Yang, and Yong Zhang. Asymmetric heat conduction in nonlinear lattices. *Physical Review Letters*, 97(12):124302, 2006. 47

[150] Jinghua Lan and Baowen Li. Thermal rectifying effect in two-dimensional anharmonic lattices. *Physical Review B*, 74(21):214305, 2006. 47, 52

[151] Jinghua Lan and Baowen Li. Vibrational spectra and thermal rectification in three-dimensional anharmonic lattices. *Physical Review B*, 75(21):214302, 2007. 47, 52

[152] Baowen Li, Jinghua Lan, and Lei Wang. Interface thermal resistance between dissimilar anharmonic lattices. *Physical Review Letters*, 95(10):104302, 2005. 47, 48, 52

[153] Alexander A Balandin and Denis L Nika. Phononics in low-dimensional materials. *Materials Today*, 15(6):266–275, 2012. 47

[154] Mohammad Alaghemandi, Elena Algaer, Michael C Böhm, and Florian Müller-Plathe. The thermal conductivity and thermal rectification of carbon nanotubes studied using reverse non-equilibrium molecular dynamics simulations. *Nanotechnology*, 20(11): 115704, 2009. 47

[155] A Rajabpour, SM Vaez Allaei, and F Kowsary. Interface thermal resistance and thermal rectification in hybrid graphene-graphane nanoribbons: a nonequilibrium molecular dynamics study. *Applied Physics Letters*, 99(5):051917, 2011. 47

[156] Feng Hao, Daining Fang, and Zhiping Xu. Mechanical and thermal transport properties of graphene with defects. *Applied Physics Letters*, 99(4):041901, 2011. 48

[157] Zacharias G Fthenakis and David Tománek. Computational study of the thermal conductivity in defective carbon nanostructures. *Physical Review B*, 86(12):125418, 2012. 48

[158] Zacharias G Fthenakis, Zhen Zhu, and David Tománek. Effect of structural defects on the thermal conductivity of graphene: From point to line defects to haeckelites. *Physical Review B*, 89(12):125421, 2014. 48

[159] Zhen Zhu, Zacharias G Fthenakis, and David Tománek. Electronic structure and transport in graphene/haeckelite hybrids: an ab initio study. *2D Materials*, 2(3): 035001, 2015. 48

[160] Md Monirojjaman Monshi, Sadegh Mehdi Aghaei, and Irene Calizo. Band gap opening and optical absorption enhancement in graphene using ZnO nanoclusters. *arXiv preprint arXiv:1706.06163*, 2017. 48

[161] Kunpeng Yuan, Mingman Sun, Zhaoliang Wang, and Dawei Tang. Tunable thermal rectification in silicon-functionalized graphene nanoribbons by molecular dynamics simulation. *International Journal of Thermal Sciences*, 98:24–31, 2015. 48

[162] Bohayra Mortazavi and Saïd Ahzi. Thermal conductivity and tensile response of defective graphene: A molecular dynamics study. *Carbon*, 63:460–470, 2013. 48

[163] Yuan Feng and Xingang Liang. Thermal rectification of silicene nanosheets with triangular cavities by molecular dynamics simulations. *Journal of Heat Transfer*, 139 (5):052402, 2017. 48

[164] Weiwei Zhao, Yanlei Wang, Zhangting Wu, Wenhui Wang, Kedong Bi, Zheng Liang, Juekuan Yang, Yunfei Chen, Zhiping Xu, and Zhenhua Ni. Defect-engineered heat transport in graphene: a route to high efficient thermal rectification. *Scientific Reports*, 5:11962, 2015. 48, 62

[165] Gang Wu and Baowen Li. Thermal rectifiers from deformed carbon nanohorns. *Journal of Physics: Condensed Matter*, 20(17):175211, 2008. 48

[166] Tamio Ikeshoji and Bjørn Hafskjold. Non-equilibrium molecular dynamics calculation of heat conduction in liquid and through liquid-gas interface. *Molecular Physics*, 81 (2):251–261, 1994. 51

[167] S Srinivasan and RS Miller. On parallel nonequilibrium molecular dynamics simulations of heat conduction in heterogeneous materials with three-body potentials: Si/ge superlattice. *Numerical Heat Transfer, Part B: Fundamentals*, 52(4):297–321, 2007. 51

[168] Zhongwei Zhang, Yuanping Chen, Yuee Xie, and Shengbai Zhang. Transition of thermal rectification in silicon nanocones. *Applied Thermal Engineering*, 102:1075–1080, 2016. 52

[169] KS Novoselov. Nobel lecture: Graphene: Materials in the flatland. *Reviews of Modern Physics*, 83(3):837, 2011. 62

[170] Kentaro Nomura and AH MacDonald. Quantum transport of massless dirac fermions. *Physical review letters*, 98(7):076602, 2007. 62

[171] Kentaro Nomura and Allan H MacDonald. Quantum hall ferromagnetism in graphene. *Physical review letters*, 96(25):256602, 2006. 62

[172] Khan MF Shahil and Alexander A Balandin. Thermal properties of graphene and multilayer graphene: Applications in thermal interface materials. *Solid State Communications*, 152(15):1331–1340, 2012. 62

[173] He Tian, Dan Xie, Yi Yang, Tian-Ling Ren, Gang Zhang, Yu-Feng Wang, Chang-Jian Zhou, Ping-Gang Peng, Li-Gang Wang, and Li-Tian Liu. A novel solid-state thermal rectifier based on reduced graphene oxide. *Scientific reports*, 2:523, 2012. 62

[174] Shiqian Hu, Jie Chen, Nuo Yang, and Baowen Li. Thermal transport in graphene with defect and doping: phonon modes analysis. *Carbon*, 116:139–144, 2017. 62

[175] Gang Zhang and Baowen Li. Thermal conductivity of nanotubes revisited: Effects of chirality, isotope impurity, tube length, and temperature. *The Journal of chemical physics*, 123(11):114714, 2005. 62

[176] Hengji Zhang, Geunsik Lee, Alexandre F Fonseca, Tammie L Borders, and Kyeongjae Cho. Isotope effect on the thermal conductivity of graphene. *Journal of Nanomaterials*, 2010:7, 2010. 62, 63

[177] Qing-Xiang Pei, Yong-Wei Zhang, Zhen-Dong Sha, and Vivek B Shenoy. Carbon isotope doping induced interfacial thermal resistance and thermal rectification in graphene. *Applied Physics Letters*, 100(10):101901, 2012. 62, 63

[178] Elaheh K Goharshadi and Sayyed Jalil Mahdizadeh. Thermal conductivity and heat transport properties of nitrogen-doped graphene. *Journal of Molecular Graphics and Modelling*, 62:74–80, 2015. 62

[179] Hamed Rezania and Mohsen Yarmohammadi. Controlling dynamical thermal transport of biased bilayer graphene by impurity atoms. *AIP Advances*, 6(7):075121, 2016. 62

[180] Pablo A Denis. Band gap opening of monolayer and bilayer graphene doped with aluminium, silicon, phosphorus, and sulfur. *Chemical Physics Letters*, 492(4-6):251–257, 2010. 62

[181] Jiayu Dai, Jianmin Yuan, and Paolo Giannozzi. Gas adsorption on graphene doped with b, n, al, and s: a theoretical study. *Applied Physics Letters*, 95(23):232105, 2009. 62

[182] Feng Li, Jingjing Li, Yan Feng, Limin Yang, and Zongfeng Du. Electrochemical behavior of graphene doped carbon paste electrode and its application for sensitive determination of ascorbic acid. *Sensors and actuators B: Chemical*, 157(1):110–114, 2011. 62

[183] Yi Wang, Chun Xian Guo, Xin Wang, Cong Guan, Hongbin Yang, Kean Wang, and Chang Ming Li. Hydrogen storage in a ni–b nanoalloy-doped three-dimensional graphene material. *Energy & Environmental Science*, 4(1):195–200, 2011. 62

[184] Pablo A Denis. When noncovalent interactions are stronger than covalent bonds: Bilayer graphene doped with second row atoms, aluminum, silicon, phosphorus and sulfur. *Chemical Physics Letters*, 508(1-3):95–101, 2011. 62

[185] PG Klemens. The scattering of low-frequency lattice waves by static imperfections. *Proceedings of the Physical Society. Section A*, 68(12):1113, 1955. 62, 66

[186] Zegao Wang, Pingjian Li, Yuanfu Chen, Jingbo Liu, Wanli Zhang, Zheng Guo, Mingdong Dong, and Yanrong Li. Synthesis, characterization and electrical properties of silicon-doped graphene films. *Journal of Materials Chemistry C*, 3(24):6301–6306, 2015. 62

[187] K Izumi, M Doken, and HCMOS Ariyoshi. Cmos devices fabricated on buried sio2 layers formed by oxygen implantation into silicon. *Electronics Letters*, 14(18):593–594, 1978. 63

[188] J Tersoff. Modeling solid-state chemistry: Interatomic potentials for multicomponent systems. *Physical Review B*, 39(8):5566, 1989. 63

[189] Shinji Munetoh, Teruaki Motooka, Koji Moriguchi, and Akira Shintani. Interatomic potential for si–o systems using tersoff parameterization. *Computational Materials Science*, 39(2):334–339, 2007. 63

[190] John Edward Jones. On the determination of molecular fields.—i. from the variation of the viscosity of a gas with temperature. *Proc. R. Soc. Lond. A*, 106(738):441–462, 1924. 63

[191] PG Klemens and DF Pedraza. Thermal conductivity of graphite in the basal plane. *Carbon*, 32(4):735–741, 1994. 66

[192] PG Klemens. Theory of the a-plane thermal conductivity of graphite. *Journal of Wide Bandgap Materials*, 7(4):332–339, 2000. 66

[193] Manav Vohra, Ali Yousefzadi Nobakht, Seungha Shin, and Sankaran Mahadevan. Uncertainty quantification in non-equilibrium molecular dynamics simulations of thermal transport. *arXiv preprint arXiv:1805.00118*, 2018. 79

[194] Ondrej Dyck, Feng Bao, Maxim Ziatdinov, Ali Yousefzadi Nobakht, Seungha Shin, Kody Law, Artem Maksov, Bobby G Sumpter, Richard Archibald, Stephen Jesse, et al. Single atom force measurements: mapping potential energy landscapes via electron beam induced single atom dynamics. *arXiv preprint arXiv:1804.03729*, 2018. 79

Vita

Ali Yousefzadi Nobakht was born in Tabriz, Iran, to the parents of Mohammadhossein and Azam. His early childhood was spent in Tabriz, Iran, where he attended NODET (National Organization for Development of Exceptional Talents) Middle and High school. He obtained his Bachelor's of Science and Master's of Science in Mechanical Engineering in 2007 and 2010 respectively.

He worked in I.D.E.M. diesel manufacturing company and I.C.O.F.C. oil company for six years and then he decided to further and diversify his education by pursing a Ph.D., and accepted a graduate research assistantship with Dr. Seungha Shin's Nanoscale Heat Transfer Laboratory, in the Department of Mechanical, Aerospace, and Biomedical Engineering at UTK in 2015. Ali is scheduled to graduate with a Ph.D. degree in Mechanical Engineering with a concentration in Thermal – Fluid Mechanics in December 2018.